2013

Study on Performance Characteristics of Interior Permanent Magnet Synchronous Motor Due to Rotor Configuration

James Kettlewell
University of Windsor

Recommended Citation

Kettlewell, James, "Study on Performance Characteristics of Interior Permanent Magnet Synchronous Motor Due to Rotor Configuration" (2013). *Electronic Theses and Dissertations*. 4733.
https://scholar.uwindsor.ca/etd/4733

Study on Performance Characteristics of Interior Permanent Magnet Synchronous Motor Due to Rotor Configuration

By

James Kettlewell

A Thesis
Submitted to the Faculty of Graduate Studies
through Electrical and Computer Engineering
in Partial Fulfillment of the Requirements for
the Degree of Master of Applied Science
at the University of Windsor

Windsor, Ontario, Canada

2013

Library and Archives
Canada

Published Heritage
Branch

395 Wellington Street
Ottawa ON K1A 0N4
Canada

Bibliothèque et
Archives Canada

Direction du
Patrimoine de l'édition

395, rue Wellington
Ottawa ON K1A 0N4
Canada

Your file Votre référence
ISBN: 978-0-494-85112-8

Our file Notre référence
ISBN: 978-0-494-85112-8

NOTICE:

The author has granted a non-exclusive license allowing Library and Archives Canada to reproduce, publish, archive, preserve, conserve, communicate to the public by telecommunication or on the Internet, loan, distrbute and sell theses worldwide, for commercial or non-commercial purposes, in microform, paper, electronic and/or any other formats.

The author retains copyright ownership and moral rights in this thesis. Neither the thesis nor substantial extracts from it may be printed or otherwise reproduced without the author's permission.

AVIS:

L'auteur a accordé une licence non exclusive permettant à la Bibliothèque et Archives Canada de reproduire, publier, archiver, sauvegarder, conserver, transmettre au public par télécommunication ou par l'Internet, prêter, distribuer et vendre des thèses partout dans le monde, à des fins commerciales ou autres, sur support microforme, papier, électronique et/ou autres formats.

L'auteur conserve la propriété du droit d'auteur et des droits moraux qui protege cette thèse. Ni la thèse ni des extraits substantiels de celle-ci ne doivent être imprimés ou autrement reproduits sans son autorisation.

In compliance with the Canadian Privacy Act some supporting forms may have been removed from this thesis.

While these forms may be included in the document page count, their removal does not represent any loss of content from the thesis.

Conformément à la loi canadienne sur la protection de la vie privée, quelques formulaires secondaires ont été enlevés de cette thèse.

Bien que ces formulaires aient inclus dans la pagination, il n'y aura aucun contenu manquant.

Canada

Study on Performance Characteristics of Interior Permanent Magnet Synchronous Motor Due to Rotor Configuration

by

James Kettlewell

APPROVED BY:

Dr. Xiang Chen, Electrical & Computer Engineering

Dr. William Altenhof, Mechanical, Automotive & Materials Engineering

Dr. Narayan Kar, Electrical & Computer Engineering

Chair of Defense Name, Chair of Defense

14/02/13

DECLARATION OF ORIGINALITY

I hereby certify that I am the sole author of this thesis and that no part of this thesis has been published or submitted for publication.

I certify that, to the best of my knowledge, my thesis does not infringe upon anyone’s copyright nor violate any proprietary rights and that any ideas, techniques, quotations, or any other material from the work of other people included in my thesis, published or otherwise, are fully acknowledged in accordance with the standard referencing practices. Furthermore, to the extent that I have included copyrighted material that surpasses the bounds of fair dealing within the meaning of the Canada Copyright Act, I certify that I have obtained a written permission from the copyright owner(s) to include such material(s) in my thesis and have included copies of such copyright clearances to my appendix.

I declare that this is a true copy of my thesis, including any final revisions, as approved by my thesis committee and the Graduate Studies office, and that this thesis has not been submitted for a higher degree to any other University or Institution.

ABSTRACT

This research study was conducted in an effort to understand what effects the rotor configuration has on the performance of a permanent magnet synchronous machine, independent of the stator configuration. Three motors were designed with different interior permanent magnet rotor configurations with the same stator laminations and were analyzed using a combination FEA *dq*-axis circuit model. The results show that the performance characteristics affected by the rotor configuration were synchronous and reluctance torque production, torque ripple, efficiency and parameter variation. The V-shaped rotor configuration produced the most torque at 70 Nm. The Flat rotor configuration had the second highest torque production at 67 Nm. The Radial rotor configuration had the highest efficiency but had the highest torque ripple. The parameter variation had an effect on the reluctance torque production capabilities of each rotor configuration due to the saturation in the machines.

DEDICATION

I DEDICATE THIS WORK TO MY PARENTS FOR THEIR CONTINUOUS SUPPORT IN MY ACADEMIC AND PROFESSIONAL CAREER.

ACKNOWLEDGEMENTS

I want to thank Dr. Kar for his guidance and supervision of my masters' research, Dr. X. Chen for his suggestions and comments, Dr. Altenhof for taking the time to advise me on verification and validation of FEA modeling and also his comments and suggestions on my research. I want to thank everyone in the Charge Lab research facility for their support throughout my research.

I also want to thank the following individuals for their assistance and support throughout my academic career:

Raymond Ong
Marko Jovanovic
Enzo Rocca
Mr. J. Halpin

A special thanks to my mother for having the patience to help me edit this thesis.

TABLE OF CONTENTS

LIST OF TABLES

LIST OF FIGURES

LIST OF ABBREVIATIONS/SYMBOLS

PMSM	Permanent Magnet Synchronous Machine
HEV	Hybrid Electric Vehicle
EV	Electric Vehicle
FLd	Flux Linkage in the *d*-axis
FLq	Flux Linkage in the *q*-axis
THD	Total Harmonic Distortion

NOMENCLATURE

B	Flux density [T]
K	Machine design constant
k_{emf}	Back EMF constant
K_w	Winding factor constant
k_m	Minor hysteresis loop constant
I_a,I_b,I_c	Stator 3-phase current [A rms]
ω_e	Electrical speed [rad/sec]
r	Radius [m]
i	Instantaneous current [A]
B_{pm}	Flux density of the permanent magnets [T]
λ_{pm}	Permanent magnet flux linkage [Wb-turns]
B_r	Remnant flux density [T]
H_c	Coercive force [A/m]
α_B	Temperature coefficients for B_r remnant flux density
α_H	Temperature coefficient for H_c coercive force
υ_{PM}	Temperature of the permanent magnets [^{O}C]
r_a, r_b, r_c	Armature resistance [Ohms]
λ_a, λ_b, λ_c	3-phase stator flux linkages [Wb-turns]
p	Differential operator
λa_{stator}, λb_{stator}, λc_{stator}	Flux linkages due to the stator currents and inductances [Wb-turns]
L_{aa}, L_{bb} and L_{cc},	Stator self-inductances [H]
L_{ac}, L_{bc} and L_{ab}	Stator mutual inductances [Wb-turns]
ϕ_m	Peak flux density due to the permanent magnets [Wb]
L_{ls}	Leakage flux inductance [H]
L_A, L_B	Magnetizing inductances [H]
θ_e	Electrical rotor position [deg.]
k_T	Krause dq transform
v_a, v_b, v_c	Three phase stator voltages [V]
v_d, v_q	d and q-axis terminal voltages [V]
i_d, i_q	d and q-axis instantaneous current values [A]
I_d, I_q	Steady state d and q-axis current values [A]

P	Number of poles
ω_m	Mechanical speed [rad/sec]
N_1	Number of turns per phase [turns]
l_{1av}	Average length per turn [m]
a	Number of conductor paths
σ_1	Eelectrical conductivity of the conductor [S/m]
s_a	Cross sectional area of the conductor
ρ	Resistivity of a material
H	Magnetic field intensity [A/m]
J_f	Current density [A/m]
A	Magnetic vector potential [Wb/m]
E	Electric field intensity [V/m]
μ	Permeability [H/m]
R_c	Core loss resistor [Ohms]
L_d, L_q	d and q-axis inductance [H]
PC	Permeance coefficient
B_m	Flux density of the magnet [T]
H_m	Magnetic field intensity of the magnet [A/m]
A_g	Area of air gap over one pole [m^2]
A_m	Area of magnet [m^2]
g	Air gap length [m]
l_m	Length of magnet [m]
E_{ph}	Back EMF value [V]
ϕ	Flux [Wb]
T_{ph}	Number of turns per phase
I_s	Peak stator current [A]

Chapter 1

1.0 Introduction

1.1 PMSM in Automotive Application

Permanent Magnet Synchronous Motors (PMSM) have been the main candidate for the application of propulsion motors in Hybrid Electric Vehicles (HEV) and Electric Vehicles (EV) by many of the main auto manufacturers such as Toyota and General Motors. Auto manufacturers recognize that today's consumers are more environmentally conscious and are concerned about rising fuel prices. In addition, the auto manufacturers are facing government regulations on target fuel efficiencies for future car models [1], [2]. Consumer concerns and government regulations have created an increasing demand for hybrid electric and electric vehicles. In the last decade, auto manufactures and their part suppliers have been investing in research and development efforts to improve the PMSM design for its application in HEV and EV and to lower their manufacturing cost. By lowering the manufacturing cost of these motors, auto manufacturers will be in a better position to make these fuel efficient vehicles more affordable to the majority of the consumers.

There are advantages in using the permanent magnet synchronous motors in HEV and EV application. They are highly efficient up to 95%, compact in design and require low maintenance. However with regards to efficiency, the motor is dependent on the loading conditions to which it is subjected [3], [4]. Most rated motor efficiencies are stated with respect to peak efficiency at a specific loading condition. In the application of HEV and EV propulsion system, the motor is put through many different loading conditions which depend on the driving conditions of the vehicle. The variable nature of the driving conditions demands that the motor be very efficient over its entire range of operation. Unfortunately, the motor cannot achieve its rated efficiency over the entire operating range.

1.2 PMSM Overview

The permanent magnet motor has been around since the 19th century [5]. In the last couple of decades, the PMSM has seen a lot of attention due to the development of high flux density and very ideal magnetic properties of the rare earth permanent magnets. The PMSM has the same operating principle as a conventional synchronous motor, which has an armature circuit and a field circuit. In a conventional synchronous motor, the field circuit sets up a static magnetic field and the armature circuit produces a rotating magnetic field. When the armature and field circuit's magnetic fields are unaligned, there will be a torque produced on the rotor shaft that will attempt to align the two magnetic fields. The torque that is produced is proportional to the cross product of the two magnetic flux densities of the field and armature circuits and can be given by:

$$Torque = k \cdot B_{field} \times B_{armature} \tag{1.1}$$

where k is a constant depending on the machine design. The fields, displaced from each other with respect to the load torque, will rotate in synchronism in the machine. This is the operating principle of both the PMSM and conventional synchronous machine.

The major difference between the two machines is that the PMSM gets its field flux from permanent magnets and the conventional synchronous machine uses a DC field circuit. The absence of the field circuit is what gives the PMSM most of its advantages. The PMSM has no associated field circuit losses thus making it more efficient than the conventional synchronous machine. It also produces less heat because there is no current flowing through a field circuit. Also, there are no friction losses due to the absence of the field circuit brushes which are needed in the conventional synchronous machine.

1.3 Aim of Study

Research shown in [6]-[15] provides the good argument that performance characteristics of a PMSM can be affected by the design of the stator and rotor. However, none of these studies have investigated which performance characteristics are only affected by the rotor alone. It is the aim of this study to investigate the design dependency of performance due to the rotor alone in the HEV and EV application. The reason why this author is only considering the rotor's effect on performance is due to the fact that the manufacturing capabilities of the stator are limited due to the complexity of the windings. If one had a strong understanding of the effects of the design and a good knowledge of the manufacturing limitations of the automotive industry, one could design a motor that meets performance criteria and manufacturability for the automotive industry. Therefore, trying to understand performance with respect to rotor design will help motor designers improve performance by altering the rotor design and not further complicating the stator design. In this study, the author has designed three different types of interior permanent magnet synchronous rotor configurations with the same stator design. In order to evaluate the performance of each rotor configuration, the author has used a model based on finite element analysis and *dq*-axis circuit modeling. The results have been analyzed with a focus on performance with respect to each rotor configuration.

1.4 Thesis Organization

The organization of this thesis is as follows:

- Chapter 1 introduces the PMSM in its HEV and EV application and states the aim of this study.
- Chapter 2 presents literature review and background theory of this study. This includes operating principles, mathematical modeling, torque production, torque ripple and a review of previous work in this area of study.
- Chapter 3 explains the FEA model coupled with a classical *dq*-axis circuit model used in this study. It discusses the model's limitations and justification for its use in this study. It also covers the design of the motors under test in this research work.
- Chapter 4 presents the analysis of all results and compares the performances of all three rotor designs. The analysis focused on the max torque production, efficiency, synchronous torque and reluctance torque production, torque ripple and parameter variation.
- Chapter 5 summaries findings and identifies future work.

Chapter 2

2.0 Literature Review and Previous Work

The PMSM has seen more attention in the last 20 years due to the invention of rare earth permanent magnet material in the 1960's [16]. The use of this high flux density permanent magnet material has allowed the PMSM to be compact in design and achieve high efficiency. These two advantages of the PMSM have made it an ideal candidate for the application of HEV and EV traction motor. In this chapter, the background theory of the PMSM will be covered. This will include basic operating principles, permanent magnet materials, motor modeling and performance factors. Also, a review of previous work done in this area will be discussed.

2.1 Fundamental Operating Principle of a PMSM

The operating principle of a PMSM is the same as a field excited synchronous machine. For the ease of explanation, we will use the example of an ideal two pole three phase PMSM (Figure. 2.1) which is supplied with three phase balance currents as given in equation 2.1.

$$\begin{aligned} I_a &= I_s \sin(\omega_e t) \\ I_b &= I_s \sin(\omega_e t - \frac{2\pi}{3}) \\ I_c &= I_s \sin(\omega_e t + \frac{2\pi}{3}) \end{aligned} \tag{2.1}$$

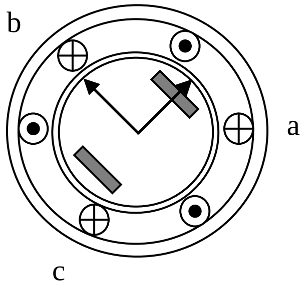

Figure 2.1: Three-phase 2 pole PMSM

In a PMSM there are two sources of flux or magnetic fields, the rotating magnetic field or rotating MMF which is setup by the three phase balance currents in equation (2.1) and the field flux or excitation flux setup by the permanent magnets. The rotating magnetic field setup by the three phase currents displaced in time by 120 electrical degree, has a speed of $2/P\omega_e$ with respect to the stationary stator. The constant flux produced by the permanent magnets will have a tendency to lock position with the rotating magnetic field. To do this, a torque will be produced on the rotor in an effort to align itself with the rotating magnetic field. A general expression for this torque is given in the following equation [17].

$$\mathrm{T} = ril B_{pm} \sin(\theta) \qquad (2.2)$$

Where i is the current in the windings, B_{pm} is the flux density of the permanent magnets, r is the radius of the stator bore, l is the length of the rotor and θ is the angle between the flux density of the permanent magnets on the rotor and the magnetic field induced by the stator currents.

2.1.1 Operating Regions of a PMSM

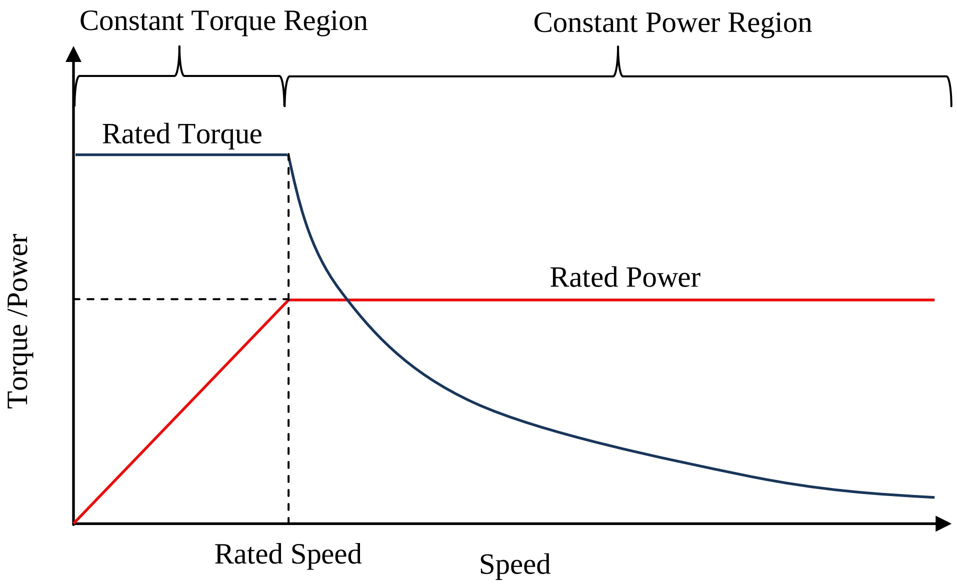

Figure 2.2: Operating Regions of a PMSM

In a typical inverter fed permanent magnetic synchronous machine, a constant torque can be achieved until the machine reaches the maximum terminal voltage that the inverter can produce [18]. At this point, the motor is said to be at its base speed and any other speed past the base speed will dictate a decrease in torque production. Below base speed, the rated torque can be achieved by applying the rated current to the machine. As the speed is increased in this region, the power has to increase if the machine is to maintain a constant torque. Hence this region is usually referred to as the constant torque region of operation. As the speed is increased in the constant torque region, the terminal voltage is also increased due to the induced back EMF dependency on speed and permanent magnet flux given by the following formula [17]:

$$E_{back\_EMF} = k_{emf} \omega_e \lambda_{pm} \tag{2.3}$$

where k_{emf} is a constant depending on the design of the machine, ω_e is the electrical speed in radians per second and λ_{pm} is the permanent magnet flux linkage. As the back EMF is increased with speed, the terminal voltage and power also have to increase to maintain constant torque. Once the terminal voltage is maxed out at the base speed, any increase in speed can only be obtained if the air gap flux density is weakened. By weakening the air gap flux density, the induced back EMF will be lowered, thus reducing the terminal voltage below its rated value. In this flux weakening region, the power is kept constant and the torque is reduced. Hence, this region is sometimes referred to as the constant power region or the flux weakening region.

2.2 Permanent Magnet Material

The three different types of permanent magnets used in machines are: Alnico, Ceramics (ferrites) and Rare-Earth Materials [19]. Each type has advantages and disadvantages depending on the application of the machine in which they are used. Therefore, depending on the application, a machine designer can select the type of permanent magnet material to use by evaluating the demagnetization curve such as the one shown in Figure 2.3 and the material's temperature coefficients with respect to the application.

The temperature coefficients are the factors that affect the remnant flux density and the coercive force as noted by the following formulas [19]:

$$B_r = B_r 20\left[1+\frac{\alpha_B}{100}\left(\upsilon_{PM}-20\right)\right] \tag{2.4}$$

$$H_c = H_c 20\left[1+\frac{\alpha_H}{100}\left(\upsilon_{PM}-20\right)\right] \tag{2.5}$$

where υ_{PM} is the temperature of the permanent magnets, B_r20 and H_c20 are the remnant magnetic flux and coercive force at 20^{o}C respectively and α_B and α_H are the temperature coefficients. The Coercive force (H_c) is the amount of reverse magnetic field that will demagnetize the magnet. The remnant flux density (B_r) is the amount of flux density that will be present if the magnetic field intensity is zero. H_c and B_r are very important quantities when deciding what type of material to use for the permanent magnets because they help determine the performance of the magnet in the application in which they are being used.

2.2.1 Alnico

The main advantage of Alnico is its high remnant flux density and its low temperature coefficient [19]. The only disadvantage is its non-linear demagnetization curve which corresponds to a low coercive force. This low coercive force means that the magnet can not only be easily magnetized but also easily demagnetized [19]. This is not a good characteristic for permanent magnets in the application of electric machines since they are exposed to non-linear reversing magnetic fields. The non-linear reversing magnetic fields may cause the magnet to demagnetize, thus affecting the performance of the electric machine. For most electric machine applications, a linear demagnetization curve is ideal.

2.2.2 Ceramics (Ferrites)

The main advantages of the Ceramic or ferrites is its higher coercive force, low cost, low temperature coefficients and linear demagnetization curve. Its main disadvantage is its low remnant flux density [19].

2.2.3 Rare-Earth Materials

Rare-earth materials have received a lot of attention in the last few decades for their use in electric machines. The major advantages of rare-earth material are its high remnant flux density, high coercive force, low temperature coefficients and its linear demonization curve. Its major disadvantage is its high manufacturing cost.

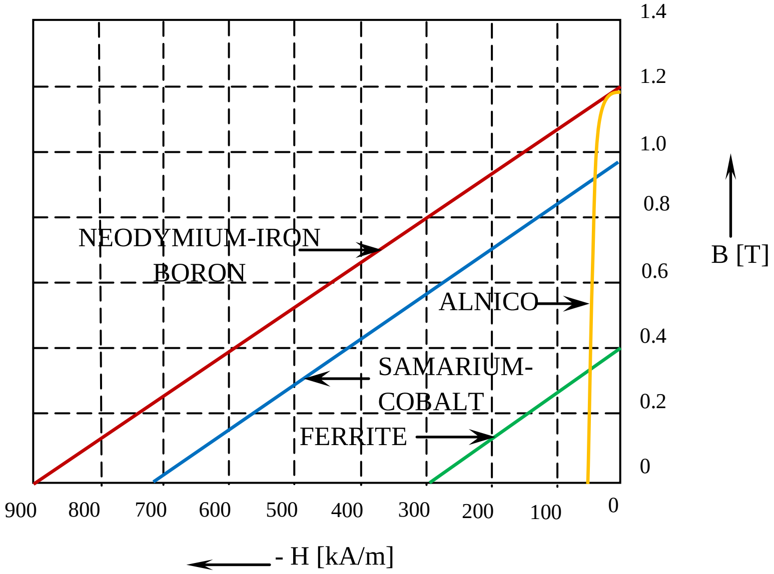

Figure 2.3: Demagnetization Curve of Permanent Magnet Material [19]

2.3 Modeling of a PMSM

2.3.1 Stator abc Reference Frame

The mathematical model of a PMSM in the stator stationary reference frame is given by the voltage equations which are expressed as a function of instantaneous stator current and flux linkages as seen in equation (2.6), where $r_a = r_b = r_c$ is the stator resistance and p is the differential operator d/dt [18], [12]. The two terms in the stator voltage equation are the stator armature resistance voltage drop and the voltage induced by the time varying stator flux linkages.

$$\begin{aligned} v_a &= r_a \cdot i_a + p\lambda_a \\ v_b &= r_b \cdot i_b + p\lambda_b \\ v_c &= r_c \cdot i_c + p\lambda_c \end{aligned} \tag{2.6}$$

The stator flux linkages can be further broken down into instantaneous stator current and inductances for a magnetically linear system as shown by the following equations [18], [20]:

$$\begin{aligned} \lambda_a &= \lambda_{astator} + \lambda_{PM} \\ \lambda_b &= \lambda_{bstator} + \lambda_{PM} \\ \lambda_c &= \lambda_{cstator} + \lambda_{PM} \end{aligned} \tag{2.7}$$

$$\begin{aligned} \lambda_{a\,stator} &= L_{aa} \cdot i_a + L_{ab} \cdot i_b + L_{ac} \cdot i_c \\ \lambda_{b\,stator} &= L_{ab} \cdot i_a + L_{bb} \cdot i_b + L_{bc} \cdot i_c \\ \lambda_{c\,stator} &= L_{ac} \cdot i_a + L_{bc} \cdot i_b + L_{cc} \cdot i_c \end{aligned} \tag{2.8}$$

$$\begin{aligned} \lambda a_{PM} &= \phi \sin(\theta r) \\ \lambda b_{PM} &= \phi \sin(\theta r - \frac{2\pi}{3}) \\ \lambda c_{PM} &= \phi \sin(\theta r + \frac{2\pi}{3}) \end{aligned} \tag{2.9}$$

where L_{aa}, L_{bb} and L_{cc}, are the stator self-inductances and L_{ac}, L_{bc} and L_{ab} are the stator mutual inductances respectively. In addition, the term λ_{pm} is the flux linkage produced by only the permanent magnets that are located on the rotor. The stator mutual and self-inductances can be further broken down as shown in equations (2.10) and (2.11).

$$\begin{aligned} L_{aa} &= Lls + LA - LB\cos(2\theta_r) \\ L_{bb} &= Lls + LA - LB\cos 2(\theta_r + \frac{2\pi}{3}) \\ L_{cc} &= Lls + LA - LB\cos 2(\theta_r - \frac{2\pi}{3}) \end{aligned} \tag{2.10}$$

$$\begin{aligned} L_{ab} &= -\frac{1}{2}LA - LB\cos 2(\theta r - \frac{2\pi}{3}) \\ L_{bc} &= -\frac{1}{2}LA - LB\cos(2\theta r) \\ L_{ac} &= -\frac{1}{2}LA - LB\cos 2(\theta r + \frac{2\pi}{3}) \end{aligned} \tag{2.11}$$

Looking at the stator self and mutual inductances in equation (2.10) and (2.11), the term L_{ls} is the stator leakage inductance and LA and LB are the magnetizing inductances. The leakage inductance is the inductance that does not contribute to the transfer of power through the air gap. Both the self and mutual stator inductance values vary with respect to rotor position θ_r, thus making them vary with time. These time varying inductances make steady state analysis of the machine difficult in the *abc* reference frame.

2.3.2 Rotor *dq* Reference Frame

A common method for modeling synchronous electric machines is the *dq*-axis model. This model transforms the stator *abc* quantities to a rotating reference frame located on the rotor. Thus, this rotating reference frame rotates at synchronous speed with the rotor. This transformation of the *abc* parameters to the *dq*-axis rotor reference frame makes the analysis and modeling of a PMSM easier due to the fact that the time varying inductance in the *abc* reference frame become non-varying in the *dq*-axis rotor reference frame at steady state. There are a few variations of the *dq*-axis transform that can be used to convert the *abc* quantities to their *dq*-axis quantities, but in this work the author has chosen to use Kruse's method. One major difference with Kruse's method is that he defines the displacement of the stator stationary axis with the rotating *dq*-axis as the angle between the *q* rotating axis and the *a* phase stationary axis, shown in Figure 2.4 below. Defining θ_e to be the angular displacement between the *q* and the *a*-axis and ω_e to be the angular velocity of the rotating reference frame, the Kruse transform is shown by equations (2.14)-(2.20) below [20]:

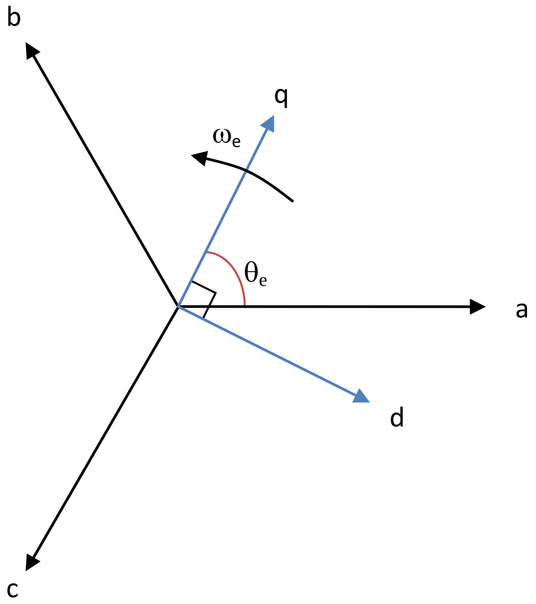

Figure 2.4: *dq*-axis Rotating Reference Frame and *abc* Reference Frame

$$f_{qd0} = k \cdot f_{abc} \tag{2.14}$$

where

$$f_{qd0} = \begin{bmatrix} f_q \\ f_d \\ f_0 \end{bmatrix} \tag{2.15}$$

$$f_{abc} = \begin{bmatrix} f_a \\ f_b \\ f_c \end{bmatrix} \tag{2.16}$$

$$k_T = \frac{2}{3} \cdot \begin{bmatrix} \cos\theta_e & \cos\left(\theta_e - \frac{2\pi}{3}\right) & \cos\left(\theta_e + \frac{2\pi}{3}\right) \\ \sin\theta_e & \sin\left(\theta_e - \frac{2\pi}{3}\right) & \sin\left(\theta_e - \frac{2\pi}{3}\right) \\ \frac{1}{2} & \frac{1}{2} & \frac{1}{2} \end{bmatrix} \tag{2.17}$$

The angular velocity and the inverse transform are as follows.

$$\omega_e = \frac{d\theta_e}{dt} \tag{2.18}$$

$$k_T^{-1} = \begin{bmatrix} \cos\theta_e & \sin\theta_e & 1 \\ \cos\left(\theta_e - \frac{2\pi}{3}\right) & \sin\left(\theta_e - \frac{2\pi}{3}\right) & 1 \\ \cos\left(\theta_e + \frac{2\pi}{3}\right) & \cos\left(\theta_e + \frac{2\pi}{3}\right) & 1 \end{bmatrix} \tag{2.19}$$

In the above equations, the term f can be any quantity such as voltage, current or flux linkage. The velocity of the reference frame ω_e is related to the angular position by [20].

$$\theta_e = \int \omega_e \cdot dt \tag{2.20}$$

Using the equations (2.14)-(2.17), one can transform any *abc* quantity in the modeling equations into the *dq*-axis reference frame. The voltage and current stator quantities can be transformed into their *dq*-axis quantities as shown below.

Given

$$v_{abc} = \begin{bmatrix} v_a \\ v_b \\ v_c \end{bmatrix} \tag{2.21}$$

where

$$\begin{aligned} v_a &= Vs \cdot \cos(\theta_e) \\ v_b &= Vs \cdot \cos\left(\theta_e - \frac{2\pi}{3}\right) \\ v_c &= Vs \cdot \cos\left(\theta_e + \frac{2\pi}{3}\right) \end{aligned} \tag{2.22}$$

Then

$$v_{qd0} = k_T \cdot v_{abc} \tag{2.23}$$

$$v_{qd0} = \frac{2}{3} \cdot \begin{bmatrix} \cos\theta_e & \cos\left(\theta_e - \frac{2\pi}{3}\right) & \cos\left(\theta_e + \frac{2\pi}{3}\right) \\ \sin\theta_e & \sin\left(\theta_e - \frac{2\pi}{3}\right) & \sin\left(\theta_e - \frac{2\pi}{3}\right) \\ \frac{1}{2} & \frac{1}{2} & \frac{1}{2} \end{bmatrix} \cdot \begin{bmatrix} v_a \\ v_b \\ v_c \end{bmatrix} \tag{2.24}$$

$$\begin{aligned} v_q &= \frac{2}{3}\left[v_a \cdot \cos\theta_e + v_b \cdot \cos\left(\theta_e - \frac{2\pi}{3}\right) + v_c \cdot \cos\left(\theta_e + \frac{2\pi}{3}\right)\right] \\ v_d &= \frac{2}{3}\left[v_a \cdot \sin\theta_e + v_b \cdot \sin\left(\theta_e - \frac{2\pi}{3}\right) + v_c \cdot \sin\left(\theta_e + \frac{2\pi}{3}\right)\right] \\ v_0 &= \frac{2}{3}\left[v_a \cdot \frac{1}{2} + v_b \cdot \frac{1}{2} + v_c \cdot \frac{1}{2}\right] \end{aligned} \tag{2.25}$$

The i_{qdo} currents can be derived in the same way as the voltage quantities shown above, thus resulting in the equation (2.26):

$$\begin{aligned} i_q &= \frac{2}{3}\left[i_a \cdot \cos\theta_e + i_b \cdot \cos\left(\theta_e - \frac{2\pi}{3}\right) + i_c \cdot \cos\left(\theta_e + \frac{2\pi}{3}\right)\right] \\ i_d &= \frac{2}{3}\left[i_a \cdot \sin\theta_e + i_b \cdot \sin\left(\theta_e - \frac{2\pi}{3}\right) + i_c \cdot \sin\left(\theta_e + \frac{2\pi}{3}\right)\right] \\ i_0 &= \frac{2}{3}\left[i_a \cdot \frac{1}{2} + i_b \cdot \frac{1}{2} + i_c \cdot \frac{1}{2}\right] \end{aligned} \tag{2.26}$$

Looking at the resistance voltage drop and assuming that all three phases have equal resistance, which is required for a balanced 3-phase condition, the resistance voltage drop in the *dq*-axis reference frame can be derived as follows:

$$Vr_{abc} = r_a \cdot i_{abc} \tag{2.27}$$

Where

$$r_s = \begin{bmatrix} r_a & 0 & 0 \\ 0 & r_b & 0 \\ 0 & 0 & r_c \end{bmatrix} \tag{2.28}$$

$$Vr_{qdo} = k_T \cdot r_s \cdot k_T^{-1} i_{qdo} \tag{2.29}$$

Then

$$k_T \cdot r_s \cdot k_T^{-1} = r_s \tag{2.30}$$

Therefore r_s in the *dq*-axis reference frame is equal to r_s in the *abc* reference frame when there is a three-phase balance condition.

$$Vr_{qdo} = r_s \cdot i_{qdo} \tag{2.31}$$

The flux linkage component of the *abc* equation (2.6), given by (2.7), can be transformed into the *dq*-axis reference frame by the equations (2.32) and (2.33) shown below [20].

$$V_{abc} = p\lambda_{abc} \tag{2.32}$$

$$V_{qdo} = k_T \cdot p[(k)^{-1}\lambda_{qdo}] \tag{2.33}$$

Equation (2.33) can be further expanded to:

$$V_{qd0} = k_T \cdot p\left[(k)^{-1}\lambda_{qd0}\right] + k_T (k_T)^{-1} p \cdot \lambda_{qd0} \tag{2.34}$$

the term $p[(k)^{-1}]$ can be derived as:

$$p \cdot \left[(k_T)^{-1}\right] = \omega \cdot \begin{bmatrix} -\sin\theta_e & \cos\theta_e & 0 \\ -\sin\left(\theta_e - \frac{2\pi}{3}\right) & \cos\left(\theta_e - \frac{2\pi}{3}\right) & 0 \\ -\sin\left(\theta_e + \frac{2\pi}{3}\right) & \cos\left(\theta_e + \frac{2\pi}{3}\right) & 0 \end{bmatrix} \tag{2.35}$$

Using trigonometric identities it can be shown that:

$$k_T \cdot p \cdot \left[(k_T)^{-1}\right] = \omega \cdot \begin{bmatrix} 0 & 1 & 0 \\ -1 & 0 & 0 \\ 0 & 0 & 0 \end{bmatrix} \tag{2.36}$$

Using the above derivation (2.36), equation (2.34) can be expanded as follows [20]:

$$V_{qd0} = \omega \cdot \lambda_{qd0} + p \cdot \lambda_{qd0} \tag{2.37}$$

where

$$\lambda_{qd0} = \begin{bmatrix} \lambda_d \\ -\lambda_q \end{bmatrix} \tag{2.38}$$

Expanding equation (2.37) [20] gives the following formulas:

$$\begin{aligned} V_q &= \omega\lambda_d + p\lambda_q \\ V_d &= -\omega\lambda_q + p\lambda_d \\ V_0 &= p\lambda_0 \end{aligned} \tag{2.39}$$

Using equations (2.31) and (2.39), the *abc* modeling equations (2.6) can be expressed in *dq*-axis reference frame as:

$$\begin{aligned} v_d &= r_s \cdot id + p\lambda_d - \omega_e\lambda_q \\ v_q &= r_s \cdot iq + p\lambda_q + \omega_e\lambda_d \end{aligned} \tag{2.40}$$

where

$$\begin{aligned} \lambda_d &= L_d i_d + \lambda_{pm} \\ \lambda_q &= L_q i_q \end{aligned} \tag{2.41}$$

For steady state analysis, these equations can be further reduced to equations (2.42) [20].

$$\begin{aligned} V_d &= r_s \cdot I_d - \omega_e\lambda_q \\ V_q &= r_s \cdot I_q + \omega_e\lambda_d \end{aligned} \tag{2.42}$$

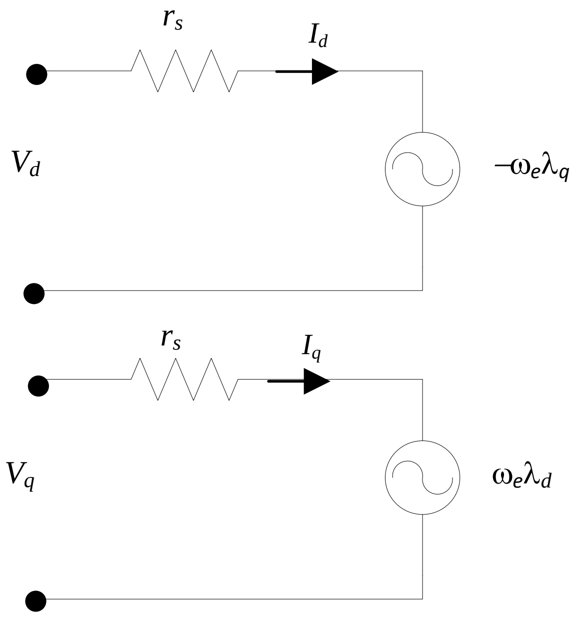

Figure 2.5: Steady State *dq*-axis Circuit Model

The quantities expressed in upper case letters like V_q and V_d represent steady state values. The steady state circuit model for the *d* and *q*-axis are shown in Figure 2.5 above.

The steady-state electromagnetic torque equation of the dq-axis model is:

$$T_{elm} = \left(\frac{3}{2}\right)\left(\frac{P}{2}\right)\left[\lambda_d \cdot I_q - \lambda_q \cdot I_d\right] \tag{2.43}$$

where P is the number of magnetic poles in the machine. Substituting equation (2.41) into (2.43), the torque equation expands to the following formula [21].

$$T_{elm} = \left(\frac{3}{2}\right)\left(\frac{P}{2}\right)\left[\lambda_{pm} \cdot I_q + \left(L_d - L_q\right) I_q \cdot I_d\right] \tag{2.44}$$

The steady state electromagnetic power can be derived by multiplying the torque by the mechanical speed ω_m in radians per second shown by equation (2.45).

$$P_{elm} = \omega_m \cdot \left(\frac{3}{2}\right)\left(\frac{P}{2}\right)\left[\lambda_{pm} \cdot I_q + \left(L_d - L_q\right) I_q \cdot I_d\right] \tag{2.45}$$

2.4 Power loss in a PMSM

Power loss in a PMSM can be separated into 4 categories:

- Stator Copper Losses
- Iron Losses
- Stray Losses
- Mechanical Losses

2.4.1 Stator Copper Losses

The stator coils are made up of copper which inherently has an electrical resistance. As current is driven through the coils, there will be a resistance drop loss proportional to the square of the current times the resistance. These losses will vary with temperature but can be easily calculated, given a specific temperature. A simple formula for resistive power loss is given by equation (2.46) below [19].

$$P_{sc} = 3 I_{LN}^2 R_S \tag{2.46}$$

The resistance in the above formula should be calculated for ac resistance. However for motors operating at frequencies around or below 60 Hz, the resistance can be approximated to be the dc resistance given by formula (2.47) [19]:

$$R_{dc} = \frac{N_1 l_{1av}}{a\sigma_1 s_a} \tag{2.47}$$

where N_1 is the number of turns per phase, l_{1av} is the average length per turn, a is the number of conductor paths, σ_1 is the electrical conductivity of the conductor and s_a is the cross sectional area of the conductor.

2.4.2 Iron Losses

The physical origin of the iron losses is usually treated on a microscopic scale and is the area of expertise of a physicist or material engineer. However, for the application of electrical machine analysis, this microscopic scale of the origin of iron losses does not provide practical means of calculating them [22]. In general, the effects of these microscopic mechanisms that dictate iron losses, cannot be known and therefore cannot be practically used to calculate losses in engineering applications [22]. To overcome the lack of application of the microscopic model of iron losses, several macroscopic and empirical models have been developed. Some of these models are the Steinmetz equation, created over a century ago and more recently Bertotti's work on representing the losses by a statistical approach based on domain theory [22], [23].

In general, iron losses are usually treated as the summation of three different types which are the hysteresis loss, eddy current loss and the excess eddy current loss.

2.4.3 Hysteresis loss

Hysteresis loss results from Barkhausen effect, where small domain wall segments make localized jumps between local minima of the system's free energy, giving rise to localized eddy currents around the jumping wall segments. The loss component depends very little on size and shape of the material. A common empirical formula based on the work of Steinmetz has been used directly or with some modification as shown in the formula below [24]:

$$P_{hys} = k_h \omega_s B_{peak}^{\beta} \tag{2.48}$$

where k_h is a constant that depends on material and geometry, β is the Steinmetz material constant, B_{peak} is the peak flux density and ω_s is the angular frequency of the varying flux density. The formula does not depend on the shape of the flux density wave form, only the peak value of it. However, it has been shown by authors[25], [26] that a flux density wave form that contains harmonics, which are called minor hysteresis loops, Figure 2.6, will affect the hysteresis loss. These minor Hysteresis loops will add to the overall hysteresis loss in a machine's magnetic material that has a flux density waveform which contains harmonics [26].

Work done by [26] has given an empirical correction factor to help take the minor hysteresis loss into account which is shown in the following formula:

$$K(B) = 1 + \frac{k_m}{B_{peak}} \sum_i \Delta B_i \tag{2.49}$$

where ΔB_i is the value of the flux i^{th} flux reversal, k_m is a constant that depends on the material and B_{peak} is the peak flux density of the waveform. With this empirical correction factor, equation (2.48) can then be adjusted to give a better empirical formula for calculating hysteresis loss in an electric machine's magnetic material. This adjustment has been made in the formula below [27].

$$P_{hys} = k_h \omega_s B^{\beta} K(B) \tag{2.50}$$

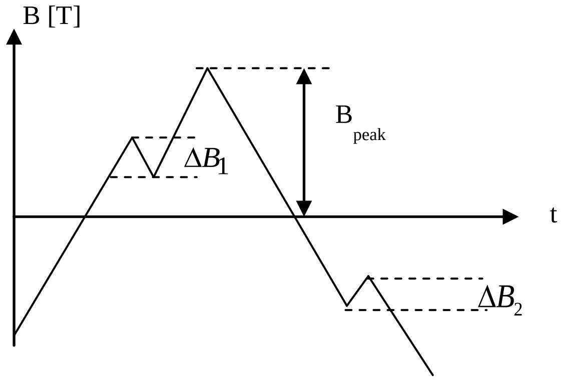

Figure 2.6: Minor Hysteresis Loops in Flux Density Waveform

2.4.4 Eddy Current Loss

Eddy current loss is caused by a net change in magnetization in the magnetic material of the electric machine [28]. This net change in magnetization will induce eddy currents in the material which are caused by Faraday's law of electromagnetic induction. These currents traveling through the material will cause a power loss due to the fact that the material has an electric resistance. This eddy current loss, due to the electric resistance of the material, can be modeled by equation (2.51) below [23], [28]. It is important to note that this loss is affected by the size and shape of the material.

For an arbitrary flux density waveform varying periodically with time, the eddy current loss can be calculated using the following formula [28]:

$$P_{eddy} = \frac{d^2}{3\pi\rho}\frac{1}{T}\int_0^T\left(\frac{dB(t)}{dt}\right) \tag{2.51}$$

where d is the thickness of the material perpendicular to the direction of the magnetic field, ρ is the resistivity of the material and T is the period of the flux density waveform [28]. If it is a P pole machine, then the period T is related to the mechanical speed ω_m using the following formula.

$$T = \frac{1}{f} = \frac{4\pi}{P\omega_m} \tag{2.52}$$

2.4.5 Excess Eddy Current Losses

The mechanism of excess eddy current loss is due to eddy currents induced around the domain walls. These eddy currents are caused by the change in magnetism in or near the domain walls due to the motion of the domains in response to an applied magnetic field [28]. The instantaneous excess eddy current loss density can be calculated using the following formula [28]:

$$P_{excess} = \sqrt{\frac{A\alpha n_o}{\rho}}\frac{1}{T}\int dt\left(\frac{dB}{dt}\right)^{3/2} \tag{2.53}$$

where A is the area of the cross section, α is a numerical constant and n_0 characterizes the statistical distribution of the local coercive fields [28].

2.4.6 Stray losses

Stray losses by definition are the difference between the total power loss and the conventional losses when the motor is loaded. These losses are usually ignored or assumed to be 0.5% of the total power input to the electric machine. The origin of the stray losses are said to be attributed to saturation of magnetic material by the load current, manufacturing imperfections of the magnetic material, space harmonics, fringing flux and leakage flux [29]. The fringing and leakage flux relates to the physical geometry of the machine. One of the factors that have been accredited to the leakage flux is the end windings of the machine.

2.4.7 Friction Losses

Friction or mechanical losses in an electric machine are due to the friction loss from the bearings in the machine and the wind resistance on the rotor.

2.5 Previous Work in the Area of Study

It is well known that the permanent magnet synchronous motor has high efficiency when compared to other motors. Research has been done by [6]-[15] to investigate and show the efficiency characteristics of different designs of permanent magnet synchronous motors. Authors of [6], [7] have investigated different designs of PMSMs for their use in hybrid electric vehicles, by examining their torque speed and efficiency characteristics. An interesting observation one could make of the work done in [6], [7] is that the rotor configuration has an effect on the efficiency characteristic of the motor. However, due to various other design changes from each motor in the investigation, the extent of the effect the rotor configuration has on the efficiency of the machine cannot be determined.

Other research done by authors in [14], [15] shows the effects of certain design parameters on power loss in PMSMs. Authors in [14] have investigated the rotor eddy current losses caused by the number of layers of the permanent magnets as well as the stator configuration being used. [15] investigates iron loss due to the dimensional shape of the stator in an interior PMSM. Work done by the authors of [8]-[13] show an adequate analysis of PMSM efficiency. Specifically the authors have investigated power loss in PMSM due to driving conditions, stator configurations and different rotor configurations. However, even with the extensive work of [8]-[13], there is not enough investigation into the rotor configuration's effects on the performance of the machine. Therefore, it is the aim of this work to investigate the performance characteristics of the PMSM caused by the rotor configuration.

2.6 FEA Modeling

Finite element analysis is a numerical method that has been used to solve for magnetic field solutions in electromagnetic devices since the mid 1970's [30]. The FEA technique is capable of solving for machine performance while taking the complex physical structure and non-linearities of the materials into account. The down side of such a numerical method is the computational time required to solve for accurate solutions.

2.6.1 Maxwell equations

The 2D Maxwell equations used by the Infolytica software package Magnet, are derived below starting with Ampere's law, assuming the displacement currents *dD/dt* are neglected [30], [31].

$$\nabla \times H = J_f \tag{2.55}$$

$$\nabla \cdot B = 0 \tag{2.54}$$

Using the constitutive tensor relation gives.

$$B = \mu \cdot H \tag{2.56}$$

$$J_f = \sigma \cdot E \tag{2.57}$$

Since the divergence of a curl in equation (2.55) is zero, it allows one to define a magnetic vector potential as shown in the following formula [30], [31].

$$B = \nabla \times A \tag{2.58}$$

Using (2.55) and (2.58)

$$H = \mu^{-1} \cdot B = \mu^{-1} \cdot \nabla \times A \tag{2.59}$$

Form Faraday's equation

$$\nabla \times E = \frac{-\partial B}{\partial t} + \nabla \times (v \times B) \tag{2.60}$$

Using (2.58)

$$E = -\nabla \times V - \frac{\partial A}{\partial t} + v \times \nabla \times A = -\nabla V - \frac{dA}{dt} \tag{2.61}$$

Where dA/dt is the total derivative which includes motion. Using (2.61), (2.57) and (2.60) in (2.54) gives the following formula [30][31].

$$\nabla \times \left(\mu^{-1} \nabla \times A\right) + \sigma \cdot \frac{dA}{dt} = -\sigma \cdot \nabla V \tag{2.62}$$

After solving (2.62) for the magnetic vector potential, A, B, H and J are found by using equations (2.58), (2.59) and (2.61) respectively.

The boundary conditions used to solve the equation (2.62) set the zero reference point of the magnetic vector potent A on the outer diameter of the stator [31]. If partial motor modeling is used, the additional periodic boundary conditions must be assigned to the appropriate edges of the model.

2.7 Saturation in Electric Machines

In an ideal electrical machine, the permeability of the electric steel (ferromagnetic material) is constant and torque production in the machine is linear with respect to the applied current. In practical machines, the ferromagnetic material, having a permeability of up to 600 times the permeability of free space, is not constant and varies depending on the loading condition [17]. A typical non-linear behavior of ferromagnetic material can be represented by the graph in Figure 2.7.

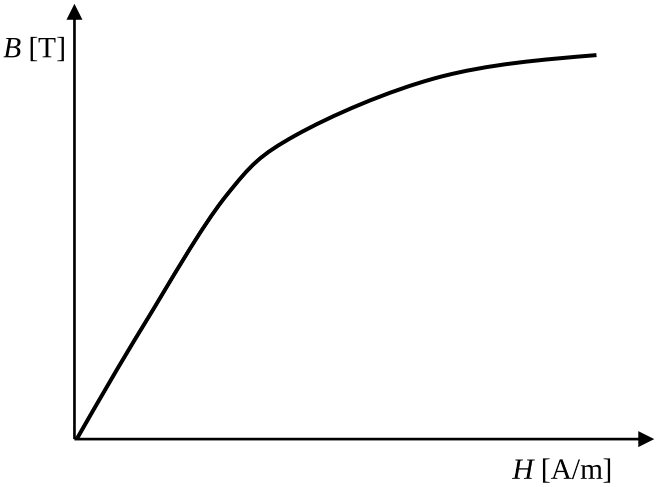

Figure 2.7: Saturation Characteristic of an Electric Machine [17]

This type of curve is generally called the magnetization curve or saturation curve of a ferromagnetic material. It shows the saturating characteristic of a ferromagnetic material due to the applied MMF or magnetic field intensity. At low levels of MMF or *H*, the flux production is linear with respect to the applied field, which can be seen in the Figure 2.7 above. This region of the graph is referred to as the linear region of operation. However, as the MMF or *H* is increased, the rate of change in the flux decreases. The decreased rate of change in the flux continues until the flux saturates to a certain value and will not increase any further with the increase of the applied field. This region of the graph is called the saturation region.

In electric machines, this saturation characteristic has an impact on performance and control. The torque production of an electric machine starts becoming nonlinear as the machine is saturated. It also makes the machine parameters L_d and L_q vary with respect to loading condition which makes model based control of electric machines difficult [32]. Saturation has also been attributed to torque ripple [33]. Work done by the authors in [33] shows that when a motor's FEA model is solved using a non-linear material characteristic (i.e. saturation), the torque ripple is greater when compared to the model solved using a linear material characteristic (i.e. no saturation).

2.8 Torque Production in an Interior PMSM

Looking at the torque production equation for a PMSM given by (2.44), it can be further broken down into two components of torque production as shown in equations (2.63) and (2.64). The first torque component that is common to all permanent magnet synchronous machines is the synchronous torque given by equation (2.63).

$$T_{sync} = \left(\frac{3}{2}\right)\left(\frac{P}{2}\right)\left(I_q \cdot \lambda_{pm}\right) \tag{2.63}$$

This synchronous component of toque is a product of the applied *q*-axis current and the permanent magnet flux linkage. The second component of torque is the reluctance torque given by equation (2.64).

$$T_{rel} = \left(\frac{3}{2}\right)\left(\frac{P}{2}\right)\left[\left(L_d - L_q\right)I_q \cdot I_d\right] \tag{2.64}$$

The production of a positive reluctance torque is only possible when the PMSM has a negative difference between the *d* and *q*-axis inductance terms. This characteristic is typically exhibited in the interior type PMSM and is not usually seen in the surface mount PMSM [21]. This capability of producing positive reluctance torque gives an advantage to the interior PMSM over the surface mount PMSM [21]. A ratio used to describe the motor's capability of producing reluctance torque is the saliency ratio. This ratio is the *q*-axis inductance to the *d*-axis inductance (i.e. L_q/L_d). The higher the saliency ratio of a motor, the more reluctance torque it is capable of producing.

2.9 Torque Ripple in Electric Machines

Torque ripple is simply the deflections of torque around an average value through time, at a steady state load value. Torque ripple is an undesirable characteristic of torque production in all electric motors which causes vibration and acoustic noise. In HEV and EV traction motors, low torque ripple is a desired characteristic. Torque ripple can be measured by the peak to peak deflection of instantaneous torque around an average value of torque, given as a percentage, which is shown in the equation below [34], [35], [36].

$$t_r = \frac{T_{\max} - T_{\min}}{T_{avg}} \times 100\% \tag{2.65}$$

The main causes of torque ripple can be attributed to [33], [37], [38]:

- Cogging Torque
- Harmonics in the Back EMF
- Saturation

2.9.1 Cogging Torque

Cogging torque is attributed to the interaction of permanent magnets and the variable reluctance of the air gap caused by the stator teeth [33], [37]. This variable reluctance will cause the rotor to try and align itself in a position where the reluctance of the magnetic circuit is minimized. The self-alignment of the rotor will cause a pulsating torque even when the machine is not powered [35]. A way to quantify cogging torque is to compare the spin loss of a magnetized and non-magnetized rotor with open stator terminals. The power required to spin the non-magnetized rotor will be due to the mechanical losses i.e. wind and friction. The power required to spin the magnetized rotor will be due to the mechanical losses plus the cogging torque losses. Subtracting the losses from both tests will give the power loss due to the cogging torque. A similar test can be run using FEA with a magnetized rotor and analyzing the loading torque on the rotor shaft when it is spun with no stator excitation.

2.9.2 Harmonics in Back EMF

In an ideal three phase synchronous machine, the air gap flux density is perfectly sinusoidal with no harmonics, thus producing a sinusoidal back EMF waveform. The ideal machine is also excited with a perfect sinusoidal current. However, in the practical situation, the air gap flux density is not perfectly sinusoidal. This is attributed to the physical constraints of the machine such as the number of slots per pole, the winding configuration of the stator and the non-sinusoidal flux distribution of the permanent magnets. This will result in the back EMF having undesired harmonics. These back EMF harmonics will induce some torque ripple into the PMSM even when being supplied by sinusoidal currents [28], [39]. This is shown by the authors in [33] and [39].

Chapter 3

3.0 Model Developed and Motor Designed for Study

The purpose of this study as mentioned in Chapter 1 is to analyze the effect of rotor configuration on the performance of the PMSM. In the following sections the methodology to complete such a study will be discussed. This will include an explanation of the model developed for this study. The model is a combination FEA software and basic circuit modeling. An overview of the motor design which was used to develop the test motor in this study will be explained. Also the verification and validation strategy and results which add confidence in the simulation results, will be presented.

3.1 Combination of FEA Simulation and *dq*-axis Circuit Model for Study

3.1.1 FEA Simulation

To take the electromagnetic effect of the rotor configuration into account on performance, a circuit model for a PMSM is coupled with a FEA model. Each of the three motors under test in this study has their own FEA model using the MagNet software package. The FEA simulation will be used to calculate the magnetizing branch of the model in order to calculate the torque output of the machine and the flux linkage of the *d* and *q*-axis. The FEA software will also be used to calculate the iron losses of the machine. Since the FEA software does not take iron losses into account when solving the FEA solution, the iron loss of the machine will be taken into account post processing in the *dq* circuit model. The iron loss value calculated by the FEA will be used to calculate an iron loss resistor that will be placed in parallel to the magnetizing branch in the circuit model. This will allow the model in this study to take into account iron losses and calculate the total input power of the machine. The iron loss calculation done by the MagNet software uses the Steinmetz equations with material constants determined from the material manufacturer’s data sheets. This iron loss calculation will take into account the hysteresis, eddy current and excess eddy current losses [31]. For the purpose of this study, this iron loss method is sufficient for determining the efficiency of each rotor configuration.

An overview of how the FEA and circuit models are coupled together can be seen in Figure 3.1. The first step in the model process is to run an FEA simulation for a specific loading condition. The FEA results will give the flux linkage of the three phase coils and iron losses of the machine that is being simulated for that specific loading condition. Those quantities will then be transformed into *dq*-axis quantities and incorporated into the *dq*-axis model. This process will be repeated for every desired operating point for all three machines.

3.1.2 *dq*-axis Circuit Model

The *dq*-axis model that is used in this study uses the following steady state equations [40]-[43].

$$\begin{aligned} V_d &= r_a \cdot I_d - \omega_e \lambda_q \\ V_q &= r_b \cdot I_q + \omega_e \lambda_d \end{aligned} \tag{3.1}$$

$$\begin{aligned} \lambda_d &= L_d I_d + \lambda_{pm\_r} \\ \lambda_q &= L_q I_q \end{aligned} \tag{3.2}$$

In addition to these steady state equations, the model will incorporate an iron loss resistor as previously stated. The *dq*-axis circuit model used in this study is shown in Figure 3.2.

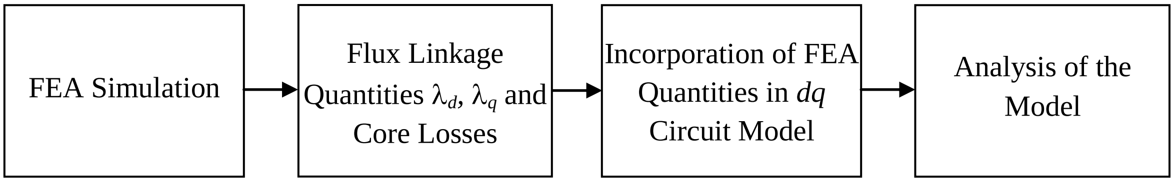

Figure 3.1: PMSM Developed Motor Model Overview

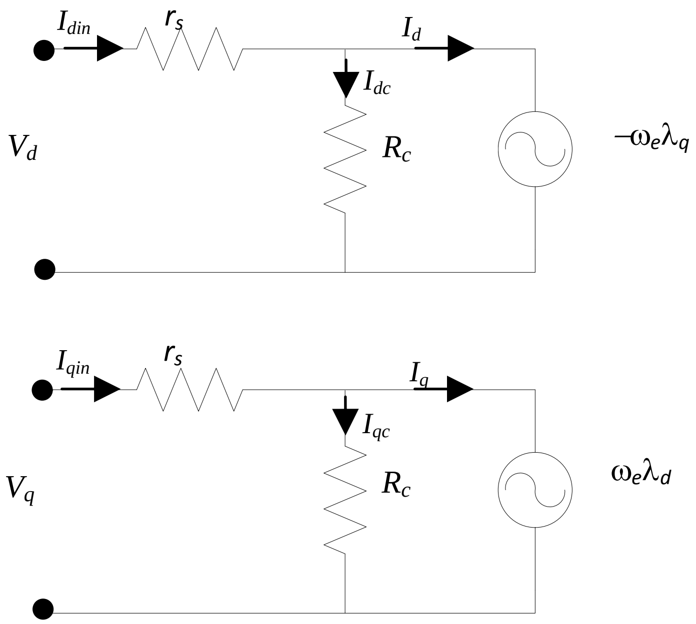

Figure 3.2: *dq*-axis Circuit Model Incorporating Core Loss Resistance

Using a resistor across the induced voltage to model the iron losses, used by the following authors [40]-[44], is a common way to model iron losses in electric machines. The iron loss resistance is placed in parallel to the induced voltage to signify that the current running through the resistor does not contribute to the output power of the machine [40]. The equations relating the power dissipated by the iron loss resistor are given by the following formulas [42], [44].

$$P_c = \frac{3}{2} \cdot R_c \left(I_{dc}{}^2 + I_{qc}{}^2 \right) \tag{3.3}$$

$$P_c = \frac{3}{2} \cdot \frac{\omega_e{}^2 \left(\lambda_d{}^2 + \lambda_q{}^2 \right)}{R_c} \tag{3.4}$$

$$R_c = \frac{3}{2} \cdot \frac{\omega_e{}^2 \left(\lambda_d{}^2 + \lambda_q{}^2 \right)}{P_c} \tag{3.5}$$

$$i_{dc} = -\frac{\omega_e \lambda_q}{R_c} \tag{3.6}$$

$$i_{qc} = \frac{\omega_e \lambda_d}{R_c} \tag{3.7}$$

3.1.3 Using FEA for Steady State Performance

Steady state FEA simulations is one type of computer aided analysis that motor designers use to test their motor designs for torque production, power loss, bus voltage requirements and any other performance requirements. Assuming the motor is completely designed in the CAD environment and ready for steady state simulations, the user will setup the simulation sequence in the following steps:

1. Set the rotor of the machine to spin at a constant speed in the desired direction of rotation.
2. Set the simulation up to apply a current excitation depending on what desired quantities of the *d* and *q*-axis current to which the motor will be subjected.
3. Run the simulation to determine how much torque the motor is capable of producing for the applied *d* and *q*-axis current for that specific speed.

These basic three steps are repeated for all different ranges of *d* and *q*-axis current, up to the max current and rotor speeds to determine the torque production capabilities of the motor design. After the torque values are known, the bus voltage is evaluated for each operating condition, i.e. *d* and *q*-axis current and rotor speed, to determine the operating range of the machine based on the max bus voltage limit value that can be applied to the coils. If the terminal voltage of the machine at a specific operating condition was higher than the max bus voltage, then that specific operating condition is not obtainable due to the bus voltage limitation. Usually under the base speed, all operating conditions are under the desired bus voltage. It is the higher speeds in the flux weakening region that have limitations on what current values and thus torque values can be achieved. It is this type of FEA simulation methodology that will be used to evaluate all three rotor configurations. In an effort to the limit the amount of simulation time needed for the evaluation of the motors, the simulations will be testing the machines in the motoring mode only. Looking at the *dq*-axis shown in Figure 3.3, one can see that the current I_s

that is being applied is broken down into its negative d-axis and positive *q*-axis components. The range of I_s will be from 10 amps to 50 amps in 10 amp increments and the current angle δ will be varied from 90 degrees to 170 degrees in 10 degree increments. Doing this will give a torque production curve similar to Figure 3.4 for a specific motor speed.

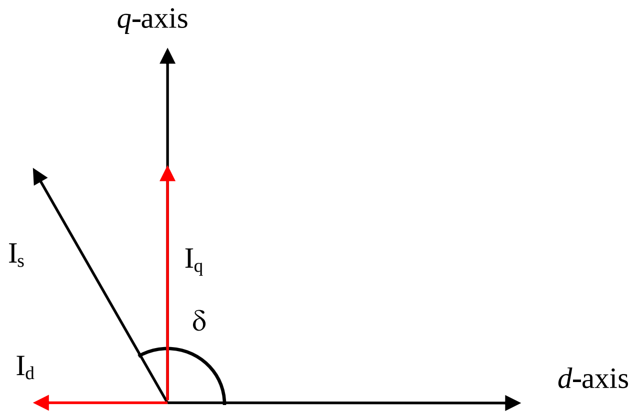

Figure 3.3: *dq*-axis Current Applied to the Model

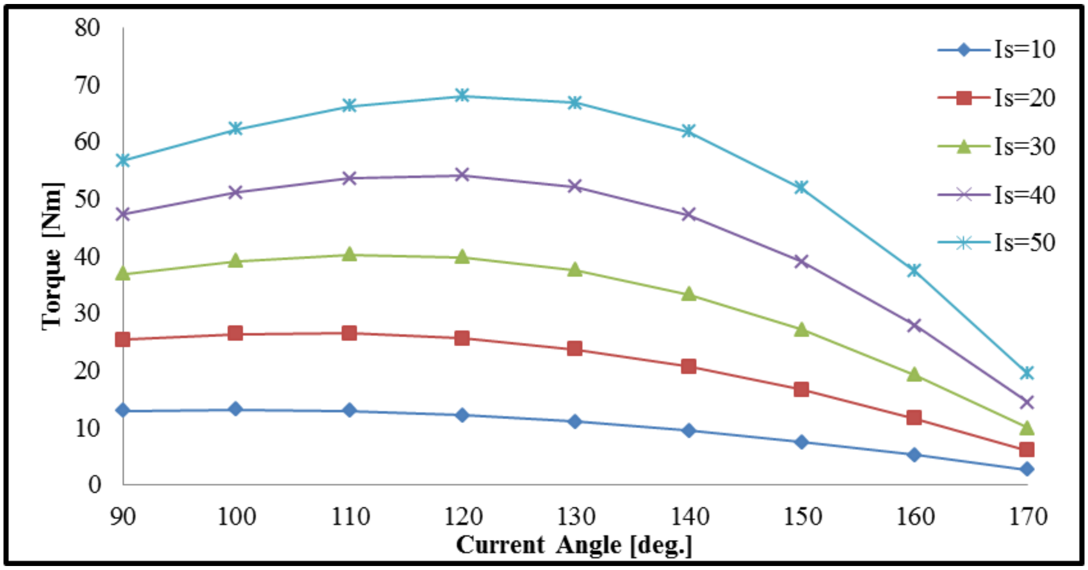

Figure 3.4: Expected Torque Production Curve from FEA Steady State Simulations

3.2 Explanation of the Types of Analysis

3.2.1 Efficiency Analysis

The efficiency of each operating condition that is simulated will be calculated to characterize the efficiency of each rotor configuration. Comparing efficiency of each rotor configuration will be done by selecting operating conditions based on the highest efficiency for each rotor configuration. The efficiency analysis of each rotor will be analyzed and then compared to the other rotor configurations.

3.2.2 Torque Ripple

Torque ripple in each rotor configuration will be evaluated using the following formula [34]-[36]:

$$t_r = \frac{T_{\max} - T_{\min}}{T_{avg}} \times 100\% \tag{3.8}$$

where T_{max} is the peak torque value, T_{min} is the minimum torque value and T_{avg} is the average torque value. Each rotor will be analyzed for torque ripple at specific operating conditions.

3.2.3 Saturation and Inductance Variations

The effects of saturation will be analyzed through the parameter variations with respect to loading conditions by solving for L_d and L_q using the flux linkages calculated by FEA through the following formulas [45].

$$L_d = \frac{\lambda_d - \lambda_{pm}}{I_d} \tag{3.9}$$

$$L_q = \frac{\lambda_q}{I_q} \tag{3.10}$$

The effects of these parameter variations which are due to saturation will then be analyzed by evaluating the toque production capabilities of the machine using the following formula.

$$T_{elm} = \left(\frac{3}{2}\right)\left(\frac{P}{2}\right)\left[\lambda_{mr} \cdot I_q + \left(L_d - L_q\right) I_q \cdot I_d\right] \tag{3.11}$$

Using equation (3.11) for torque production, one can see the dependence of L_d and L_q on the reluctance torque term.

$$T_{rel} = \left(\frac{3}{2}\right)\left(\frac{P}{2}\right)\left[\left(L_d - L_q\right)I_q \cdot I_d\right] \tag{3.12}$$

Assuming that the magnetic flux due to the permanent magnets is unaffected by saturation, the reluctance torque will vary with parameter variations caused by saturation in the machine. These affects will be analyzed with respect to rotor configuration.

3.2.4 Air Gap Flux Density Distribution and Back EMF

The ideal machine has a perfectly sinusoidal air gap flux density which will produce a back EMF with no harmonics. In a practical machine, the air gap flux density and the back EMF are not ideal sinusoidal waveforms due to the physical design of the machine. Any harmonics in the air gap flux density, that are not the fundamental component, will not be contributing to the torque production in the machine. These extra harmonics can have a negative effect on the motor performance resulting in iron losses and unfavorable torque pulsations. The back EMF waveform of each rotor configuration will be evaluated with respect to the harmonic content and its impact on toque ripple of each rotor configuration.

3.3 Limitations of the Model Developed

The model used in this study is limited due to a number of ideal assumptions taken in developing the model. The reason for selecting 2D over 3D FEA modeling was due to the advantage of reduction in the computational time of using 2D over 3D. However, the main disadvantage is that some of the 3D effects on performance are not taken into account by the 2D simulation. Some of these effects are skewing of the stator or rotor to reduce the torque ripple and the end winding leakage flux [46]. For steady state analysis of a motor design, these are acceptable limitations as long as the analyst is aware of the effects they will have on the motor performance. Since the 3D effects are not the focus of this study, the 2D analysis is acceptable.

There are other ideal assumptions such as the mechanical losses (i.e. wind and friction) which are not taken into account in the motor model for this study. Therefore, the efficiency analysis is based on the electromechanical energy conversion and does not include the mechanical losses. It is assumed that the magnet placement on the rotor will not affect the mechanical losses since the magnets are all of the same size and mass.

Also, it is known that the mechanical losses are small enough that they can be neglected in the analysis of the motor design as long as it known that the additional mechanical losses will affect the efficiencies of the manufactured machine. Mechanical losses such as wind and friction can attribute up to 5% of the total power loss in the machine [47]. Another assumption is that the motor is being supplied by ideal sinusoidal currents and that there are no harmonics induced by power electronics that may be controlling the motor.

3.4 Overview of Motor Design for This Study

3.4.1 Methodology of Design for This Study

The design of PMSM in the last 20 years has mainly been application specific with no general standardization [48]. Most design procedures start with analytical equations that are based on performance requirements and require an iterative process to refine the design [49]. In most cases, finite element analysis is used to help with the refinement process. The design approach in this work was derived from the same approaches in [48] and [49] where the motor performance requirements are stated and the overall motor dimensions are known. The objective of this research is to investigate the motor performance characteristics based on rotor design. To do this, the stator laminations and winding configuration will be the same for every motor under test and will only vary in an effort to achieve a common design performance criterion. The rotor designs are simplified by keeping the same magnetic volume in all three rotors. In addition, there will not be any optimization of the rotor with respect to flux barriers to achieve a better performing motor. This was done in an effort to see what effects the magnet placement has on the motor performance.

There are many different types of PMSM's, but the interior permanent magnet rotor type is getting the most attention in the application of HEV and EV .In this study, the focus will be on three different types of interior permanent magnet synchronous machines. The three different types are Flat interior, V-shaped interior and Radial interior, which are shown in Figure 3.5. These three were selected because they are the basic interior rotor types. Many other interior rotor configurations are based on these three configurations.

3.4.2 Material for Motors Designed in Study

The choice of material for the stator and rotor laminations was based on common materials used in this application of permanent magnet synchronous motors. The lamination material is non-oriented silicon steel of grade M-19 26 Ga which is used in high efficiency motors in the range of 1-200Hp [50]. However, different magnetic steel manufacturers use different grading systems to characterize their steel magnetic performance. Therefore, one has to be aware if a manufacturer uses a different grading system for their material. A manufacturer's equivalent M-19 26 Ga steel may not be an exact equivalent thus having some variation in the magnetic parameters. The magnetization characteristics of the M-19 26 Ga laminations used in this study are shown in Figure 3.6.

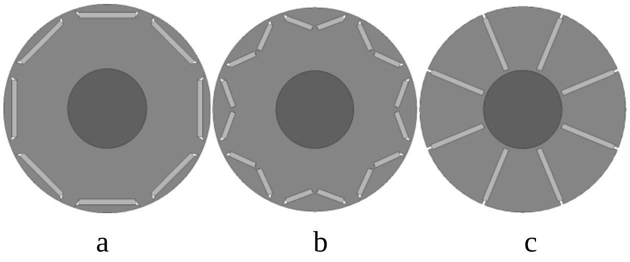

Figure 3.5: Rotor Configuration Selected for Study a) Flat b) V-shaped c) Radial

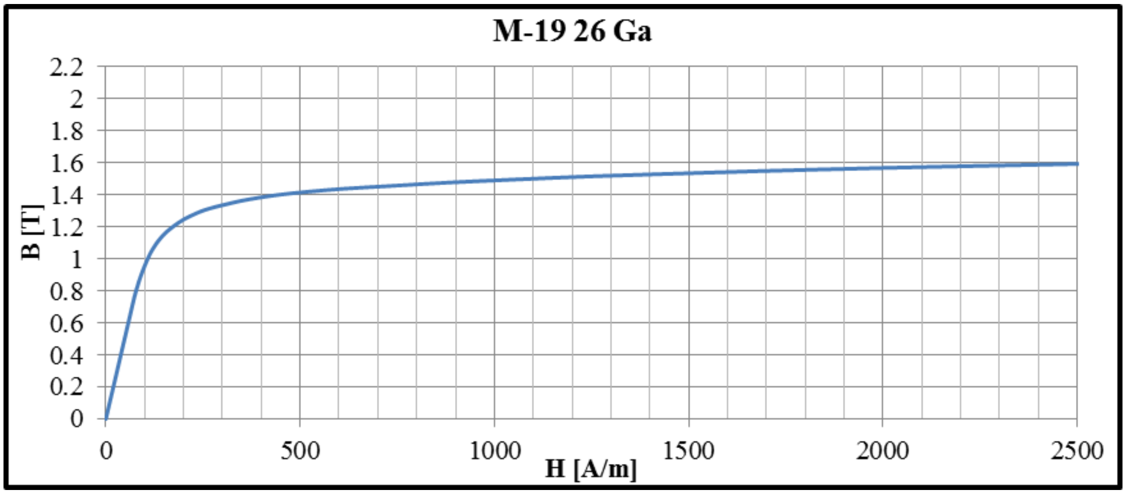

Figure 3.6: M-19 26 Ga Steel Used for the Rotor and Stator Laminations [50]

The permanent magnet material chosen was rare earth Neodymium Iron Boron: 28/32. This material was selected because it is used in motor applications for its high remnant flux density and high operating temperatures. The demagnetization curve for the Neodymium Iron Boron: 28/32 is given in Figure 3.7 for the motor operating temperature of 125 degrees C.

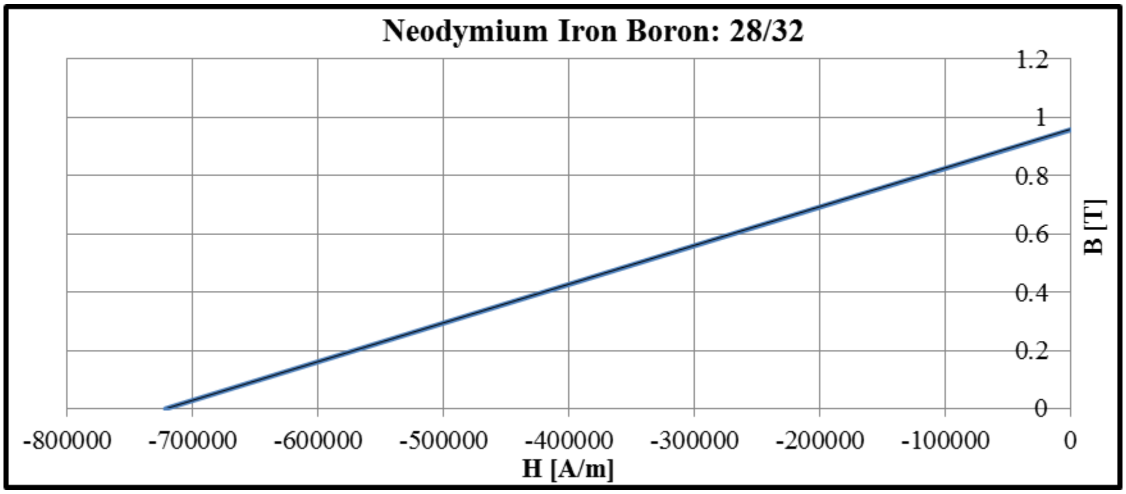

Figure 3.7: Demagnetization Curve for Permanent Magnet Material [50]

3.4.3 Overview of Motor Design

The motor performance design parameters for this study are listed in Table 3.1. These performance parameters were chosen for two reasons. First, it was necessary to keep the power rating under a desired limit so that the heat generated by the motor could be dissipated by an external fan. If the motor's power rating caused it to produce excessive heat thus requiring external cooling, then there would have to be additional design considerations on the external cooling to keep the motor at a nominal operating temperature. Secondly, the design parameters were chosen for the possibility of building and testing of the motors in the current facilities at CHARGE Labs located at the University of Windsor. The CHARGE Labs facility is currently set up to test 15 kW machines. If higher power motors were to be built, an extra cost would occur to get these motors tested at another facility. Therefore the power rating was kept under 15 kW.

.

Table 3.1: Performance Criteria

Performance Criteria	
T_n	50 Nm
N_n	1,500 rpm
$V_{L\text{-}L\ rms}$	300 V
I_n rms	35 A
Number of Phases	3
Number of Poles	8
Operating Temperature	125^{O} C
Max Operating Temperature	155^{O} C
Operating Frequency	100 Hz

Table 3.2: Motor Dimensions

Motor Dimensions	
Stator Outer Radius	95 mm
Stator Inner Radius	59.2 mm
Rotor Radius	58.4 mm
Rotor Shaft Radius	22.4 mm
Air Gap	0.8 mm
Axial Length	188.9 mm
Number of Slots	36
Winding Type	Double Layer Lap
Yoke Width	14.1 mm
Tooth Width	3.5 mm
Tooth Length	21.7 mm
Packing Factor	0.7
Area of Slot	0.00018805 m^2

The stator laminations chosen for this motor design is shown in Figure 3.8. The stator lamination has an outer dimension of 95 mm, an inner dimension of 59.2 mm and 36 slots. All other main dimensions that are common to all three motor designs are listed in Table 3.2.

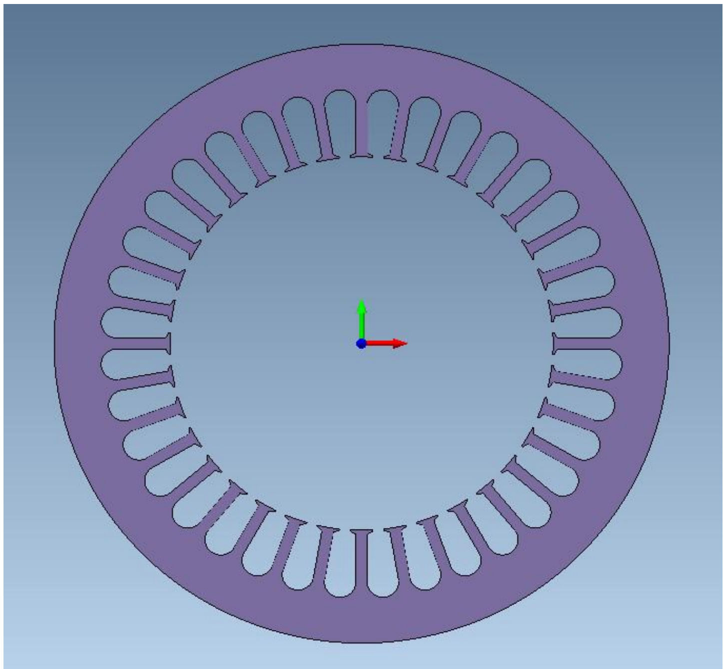

Figure 3.8: Stator Lamination

The winding configuration will be a double layer lap winding with 36 slots, with three phases and 8 poles. The number of slots per pole per phase is given by the following formula.

$$q = \frac{N_{slots}}{m \cdot P} = \frac{36}{3 \cdot 8} = 1.5 = \frac{3}{2} = 1\frac{1}{2} \tag{3.13}$$

Since the number of slots per pole per phase is not an integer, an integral slot winding is not possible. Therefore, a fractional slot winding will be used in the design of the stator coil configuration. A fractional slot winding is a little more complex to design than the integral slot winding, but it has its advantages. Using the method in [51] and [52], the fractional slot winding layout will consist of:

- The basic unit of 2 poles.
- Each phase will have 3 slots within 2 poles.
- All 3 phases will have 9 slots in 2 poles.
- Within the 2 pole basic unit, each phase has 1 coil group with a single coil and 1 coil group with 2 coils.
- The maximum number of parallel paths is 4.

With the fractional slot criteria listed above, the basic unit of the winding configuration is shown in Figure 3.9. This basic pole unit will then be repeated 4 times in the 8 pole machine to complete the entire winding configuration of the stator. There will be a series connection between all basic pole units in the winding. The coil pitch is selected to be 4 slots. The winding parameters that will affect the winding factor are listed in Table 3.3. The number of turns of each coil is determined based on performance requirements and the magnetic circuit design of the machine. The determination of the number of turns will be covered in the next section.

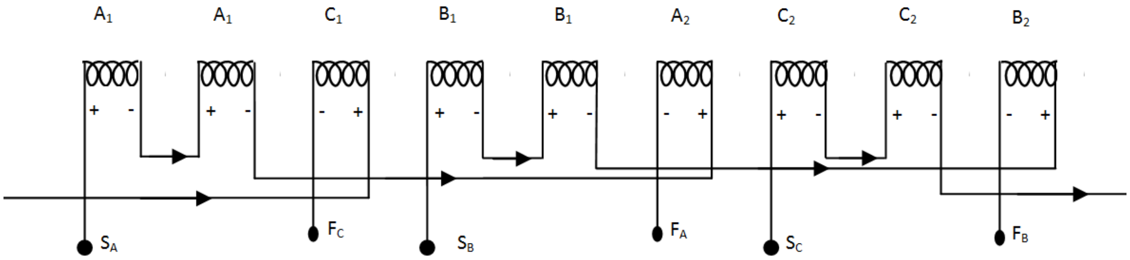

Figure 3.9: Base Pole Winding Layout

Table 3.3: Winding Parameters

Winding Parameters	
q	1.5
Slot Angle Between Two Consecutive Slots	40 Electrical Degrees
Magnetic Angle Between Phasors of the EMF	20 Electrical Degrees
Distribution Factor for a Fractional Slot Winding	0.9746
Pitch Factor	0.9848
Skew Factor	0.9798
Winding Factor $K_w = k_d k_p k_s$	0.9404

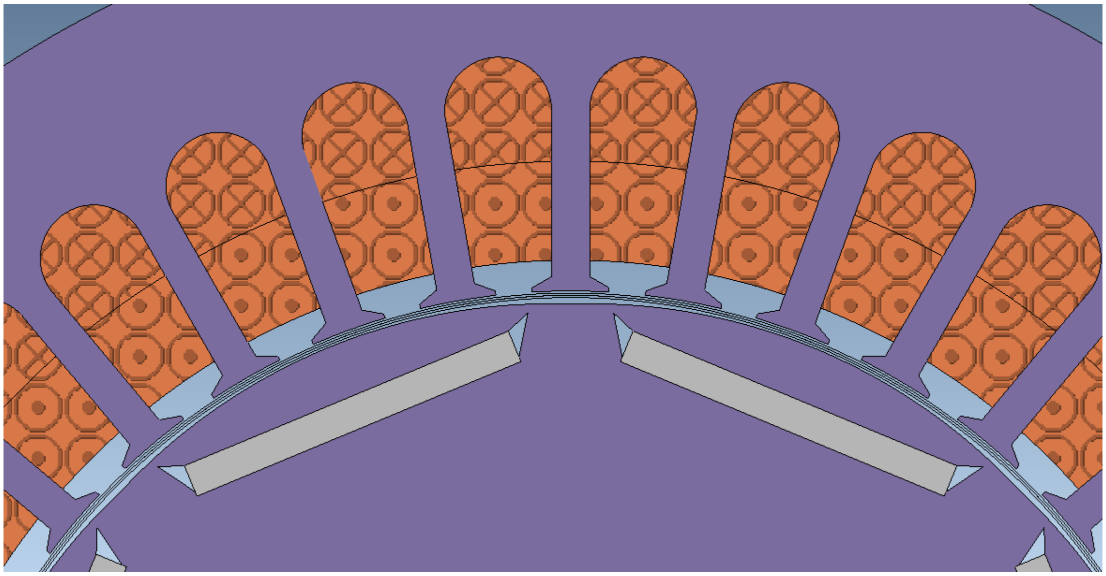

Figure 3.10: Air Gap Profile

3.4.4.1 Rotor Design

The rotor was designed to promote a sinusoidal flux density distribution in the air gap. An attempt to achieve this was done by varying the curvature of the rotor face with respect to the d axis of the rotor as shown in the Figure 3.10. The highest point of the rotor is directly above the pole face, where the air gap is 0.8 mm. The lowest part is located directly between two poles of the rotor, where the air gap is 1.2 mm. This type of design is done in synchronous machines to help achieve a better sinusoidal flux density distribution in the air gap. This will be done for all three rotor designs in this study.

3.4.4.2 Magnetic Circuit Design

The magnetic circuit design of the motor is dependent on other design parameters such as the material used, the dimension and the performance requirements of the machine. In the iterative process of machine design any of these quantities can be varied to try and achieve specific design specifications. However, in this study most of these design parameters have been fixed and the magnetic circuit only depends on the permanent magnet shape and the number of turns per coil. Therefore, the permanent magnet shape and number of turns per coil will be varied to achieve the desired performance of each motor in this study.

3.4.4.3 Permanent Magnet Operating Point

The Permeance Coefficient (*PC*), or *B/H* ratio, is the quantity that describes the operating point at which the magnet will function when placed into a magnetic circuit [53][49]. A formula for the Permeance Coefficient is given by equation (3.14) [49]. This formula may change depending on the magnetic circuit and geometry of the magnet.

$$PC = \frac{B_m}{\mu_0 H_m} = \frac{Ag \cdot lm}{Am \cdot g} \tag{3.14}$$

This formula is assuming that there is no leakage flux and that the potential drop in the magnetic core of the magnetic circuit is negligible. When designing a PMSM, it is preferred to have a relatively high PC value. This is done to ensure that the operating point of the magnet is away from the knee point of the demagnetization curve to avoid permanent demagnetization during the magnet's operation. For the radial rotor design, the PC equation shown by (3.14) has to be modified, as suggested by author [49].

3.4.4.5 Sizing of Magnets and Number of Turns

Sizing restrictions of the magnets were determined by the dimensional restraints established in the initial design requirements. The magnet width and height were varied within the sizing restrictions to see the effect on the permeance coefficient. The number of turns were also calculated based on the magnet size, the demagnetization curve, the *PC* value and B_m. The formulas used to determine the number of turns are given in the following formulas [49],[50],[52]:

$$\Phi = B_g \cdot A_g = B_m \cdot A_m \tag{3.15}$$

$$E_{ph} = 4.44 \cdot f \cdot \Phi \cdot T_{ph} \cdot K_w \tag{3.16}$$

$$T_{ph} = \frac{Eph}{4.44 \cdot f \cdot \Phi \cdot K_w} \tag{3.17}$$

where E_{ph} is assumed to be the max bus voltage, f is the frequency at a desired speed above base speed and K_w is the winding factor. After varying the magnet size and the number of turns using the analytical equations above, an initial design was frozen and then evaluated using FEA software. After a few iterations using the FEA software and after making slight modifications to the number of turns, the final design of the motors was chosen. The magnet sizing and number of turns for each motor are shown in Table 3.4. This final design of the magnetic circuit uses 1.81E-05 m^3 of permanent magnet material for each rotor configuration. The dimensions of the magnet used in the Flat and Radial rotor configuration are the same. Only the V-shaped rotor configuration has a different size magnet due to its configuration. All three rotor configurations have the same rectangular shape and magnet height of 3mm along the magnetization direction. In all three rotor configurations, the volume of material taken away for the flux barriers is the same in order to eliminate any bias of less material for core loss comparison. The final rotor configurations are shown in Figure 3.11. The name plate data for all three rotor configuration is stated in Table 3.5.

Table 3.4: Magnet Dimensions and Number of Turns

Magnet Dimensions and Number of Turns	Flat	V-shape	Radial
w_m [m]	0.032	0.032	0.032
h_m [m]	0.003	0.003	0.003
A_m [m^2]	0.006	0.006	0.006
Number of Turns Per Coil	6	7	6

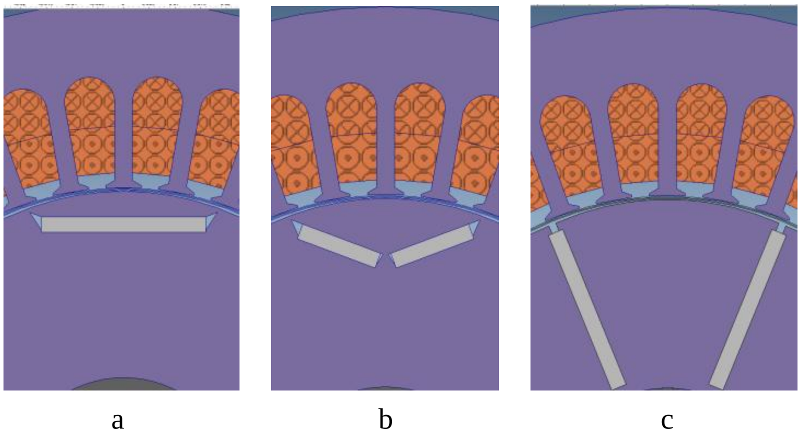
a b c

Figure 3.11: Rotor Designs For Study a) Flat b) V-shaped c) Radial

Table 3.5: Name Plate Data

Name Plate Data	
Bus Voltage	300 $V_{L\text{-}L\ rms}$
Rated Speed	1500 RPM
Rated Torque	50 Nm
Rated Current RMS	35 A

3.5 Verification and Validation of the Model Developed

In this study, a model was developed to investigate the performance of three different permanent magnet synchronous machines rotor configurations. The main source of data in this study is based on computer simulations. The author of this work has found it necessary to validate the model used in this study to prove confidence in the results. To accomplish this validation, the following Verification and Validation plan was developed.

There are many research papers that explain guidelines in the verification and validation efforts, such as [54], [55] to name a few. However, the authors of these papers point out that verification and validation process has not yet reached an industry standard. They suggest not using their papers as a standard but rather as a guideline in the method of validating a computer model. To understand the verification and validation processes the following definitions should be stated [54], [55]:

"Verification: The process of determining that the computational model accurately represents the underlying mathematical model and its solutions."

"Validation: The process of determining the degree to which a model is an accurate representation of the real world from the perspective of the intended uses of the model."

Simply stated, the verification is concerned with the computational mathematics and the validation is concerned with the accuracy of said model to the real world situation that it is trying to represent. The verification and validation process which has been undertaken for this study has two main steps: verification of the model and validation of the model to other independent results.

3.5.1 Verification

In the verification of the model, it is assumed that the software package MagNet has had its code verified and therefore no code verification is required. The calculation verification is done in two parts, a power balance study and a mesh refinement study.

The power balance study is done to select a time step that is adequate enough to solve the model to a reasonable accuracy. This is done by evaluating the total power of the system over one electrical cycle for different time steps. The equation used for the power balance study is shown below:

$$P_{in} = P_{loss} + P_{mech} + P_{mag} \tag{3.18}$$

where P_{loss} is the Ohmic losses, P_{mech} is the Torque times the mechanical speed and P_{mag} is the time rate of change in the stored magnetic energy.

The object of this power balance study is to quantify the error in the power balance equation. As the time step is reduced, the error should decrease with no divergence of the error that would violate the power balance of the system i.e. $P_{in} = P_{out}$. There will always be an error no matter how small the time step chosen. This is due to the error associated with the computational finite element method. It is up to the user of the FEA software to determine how much error is acceptable for the accuracy requirements of the model.

The mesh refinement study was conducted after the time step was chosen by the power balance study. The purpose of the mesh refinement study was used to establish what degree of mesh refinement is required for the desired accuracy of the model. This is done by systematical refining the mesh size by a certain value and solving the model for a quantity of interest. The mesh refinement steps can be seen in the Figure 3.12.
For each mesh refinement step, the difference in the quantity of interest was determined by using the average relative error shown in equation (3.19). In the case of this study the quantity of interest was torque production. The final mesh size is determined at the discretion of the model user depending on how much error is acceptable.

$$\frac{1}{N}\sum_{i=1}^{N}\frac{\left|f_{i\_ref} - f_i\right|}{\left|f_{i\_ref}\right|} \tag{3.19}$$

where N is the number of samples

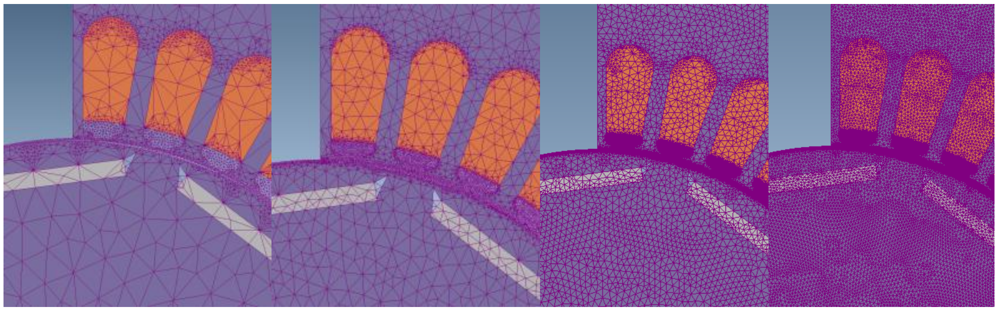

Figure 3.12: Mesh Refinement

In both parts of the verification assessment, power balance and mesh refinement, the selection of time step and mesh size was weighted against computational time. This was done in an effort to get the most accurate results with the most acceptable computational time. Therefore, time steps and mesh sizes were selected knowing that more refinement on these two variables may yield more accurate results. However, the cost of computational time did not constitute added value to the study being conducted. For the time steps and mesh sizes chosen for the simulations in this study, please refer to tables 3.12 and 3.13 in section 3.5.3.

3.5.2 Validation

The validation of the model developed was a challenge to the author due to the lack of experimental data on the machines used in this study. One alternative was to build machines to the exact specification that are simulated in the FEA software and perform validation test on the prototype motors. This would have been an ideal way to validate the model in this study. Unfortunately due to lack of funding and time that would be required to build and test the machines properly, this was not an option for validating the model. To validate the model, the author has chosen to compare the model results to a motor design software that is well established in industry. This motor design software program is specific for motor design engineers in industry.

The author recognizes that this not the ideal way to validate a computer model. However, since this model is used simply for a study on performance in specific machine designs, this validation is more than adequate since the software used to validate the model is well established in industry. To validate the model, all three motor designs were analyzed in the motor design software for specific operating points to calculate the average torque. The model developed was also solved for the same operating points to calculate the average torque. To validate the model developed in this study, the relative error between the average torque calculated by the motor design software and the average torque calculated by the model developed was evaluated.

There will be a certain amount of error between the two software simulations but as long as it is assessed within acceptable limits, the model is validated for its use in this study and can be used with confidence in its results. The formula used for relative percent error is given by equation (3.20):

$$\frac{\left|f_{\exp} - f_{\mathrm{mod}el}\right|}{\left|f_{\exp}\right|} \times 100\% \tag{3.20}$$

where f_{exp} is the value obtained from the motor design software and f_{model} is the value obtained from the model developed for this study.

3.5.3 Results and Conclusion of V&V Study

The results of the Verification and Validation of the model developed in this study are listed in Tables 3.6-3.14. As stated earlier, the results of the power balance study for all three rotor designs are used to determine the time step for the simulations and are given in Tables 3.6, 3.7 and 3.8. The time step that is chosen is based on what speed the motor is being simulated. The time base relation to speed is chosen so that the motor will move one degree every time step in the FEA simulation. The results for this time base are shown in the middle column in Tables 3.6-3.11. Looking at the power balance error quantity in Tables 3.6, 3.7 and 3.8, it can be observed that the error increases as the speed increases. However, looking at the error associated with the base time step, the error is within acceptable limits. Therefore, this base time step of one degree per time step will be used in this study for all three rotor configurations at every speed. The time steps for the FEA simulations for all speeds simulated are listed in table 3.12.

Table 3.6: Power Balance Study Results Flat Rotor Configuration

Flat			
750 rpm			
Time Step [sec.]	0.000444	0.000222	0.000111
Power Balance [W]	-4.2082	-0.9939	-0.2396
1,500 rpm			
Time Step [sec.]	0.000222	0.000111	0.0000556
Power Balance [W]	-8.4271	-1.988	-0.4793
6,000 rpm			
Time Step [sec.]	0.0000556	0.0000278	0.0000139
Power Balance [W]	-33.7277	-7.9625	-5.8922

Table 3.7: Power Balance Study Results Radial Rotor Configuration

Radial			
750 rpm			
Time Step [sec.]	0.000444	0.000222	0.000111
Power Balance [W]	-3.0616	-1.3667	-0.232
1,500 rpm			
Time Step [sec.]	0.000222	0.000111	0.0000556
Power Balance [W]	-6.1203	-1.5161	-0.4626
6,000 rpm			
Time Step [sec.]	0.0000556	0.0000278	0.0000139
Power Balance [W]	-24.6339	-6.0853	-1.8388

Table 3.8: Power Balance Study Results V-shaped Rotor Configuration

V-shaped			
750 rpm			
Time Step [sec.]	0.000444	0.000222	0.000111
Power Balance [W]	-3.0616	-1.3667	-0.531
1,500 rpm			
Time Step [sec.]	0.000222	0.000111	0.0000556
Power Balance [W]	-8.5436	-1.5161	-0.4626
6,000 rpm			
Time Step [sec.]	0.0000556	0.0000278	0.0000139
Power Balance [W]	-24.6339	-6.0853	-2.062

The mesh refinement study results are listed in Tables 3.9, 3.10 and 3.11. Looking at the results one can see the very low relative error values in the torque production of each mesh refinement step. The author has chosen to use the double base mesh size due to its lower computational time compared to the quarter base mesh size. The mesh sizes for the FEA simulations are listed in table 3.13.

Table 3.9: Mesh Refinement Study Results Flat Rotor Configuration

Flat						
Mesh Size	Tave@750 rpm	Absolute Relative Error	Tave@1,500 rpm	Absolute Relative Error	Tave@6,000 rpm	Absolute Relative Error
Base	56.7273		56.7276		56.7175	
Double Base	56.6687	0.0012	56.6656	0.0013	56.6585	0.0013
Quarter Base	56.6818	0.0006	56.6855	0.0008	56.6788	0.0008

Table 3.10: Mesh Refinement Study Results Radial Rotor Configuration

Radial						
Mesh Size	T_{ave}@750 rpm	Absolute Relative Error	T_{ave}@1,500 rpm	Absolute Relative Error	T_{ave}@6,000 rpm	Absolute Relative Error
Base	59.1631		59.1625		59.1629	
Double Base	59.1426	0.0005	59.142	0.0005	59.1424	0.0005
Quarter Base	59.1631	0.0006	59.1623	0.0006	59.1626	0.0006

Table 3.11 Mesh Refinement Study Results V-shaped Rotor Configuration

V-shaped						
Mesh Size	T_{ave}@750 rpm	Absolute Relative Error	T_{ave}@1,500 rpm	Absolute Relative Error	T_{ave}@6,000 rpm	Absolute Relative Error
Base	53.8183		53.8141		53.8104	
Double Base	53.6519	0.0031	53.6515	0.003	53.6475	0.003
Quarter Base	53.6718	0.0005	53.6708	0.0005	53.6671	0.0005

The model validations results for the torque production value of the model compared to the motor design software results are shown in Tables 3.14, 3.15 and 3.16. The FEA simulation time step and mesh refinement were chosen by the verification results stated earlier. Looking at the percentage error in the average torque developed by each rotor configuration, one can see that it depends on the rotor configuration. The Flat rotor configuration had the lowest percentage error between the two models at 4.6% and the V-shaped rotor configuration had the highest at 10.8%. For the purpose of this study, the author believes that these error values are within limits of acceptability to give confidence in the results given by the model developed in this study.

Table 3.12: FEA Simulation Time Steps

Time Step Chosen for FEA Simulations					
Speed [RPM]					
	750	1500	3000	4500	6000
Time Step [ms]	0.222222	0.111111	0.055556	0.037037	0.027778

Table 3.13: FEA Simulation Mesh Sizes

Mesh Size Chosen for FEA Simulations				
Model Element				
	Stator	Rotor	Air Gap	Air Box
Max Element Size [m]	0.0025	0.0025	0.00025	0.05

Table 3.14: FEA Simulation VS Motor Design SW Results for Flat Rotor Configuration

Rotor Type: Flat	FEA Model Torque [Nm]	Motor Design SW Torque [Nm]	Error	Absolute Error	Percentage Error %
750 rpm	56.6687	54.18	2.4929	2.4929	4.6014
1,500 rpm	56.6655	54.06	2.6079	2.6079	4.8244
6,000 rpm	56.6585	53.35	3.31	3.31	6.2046

Table 3.15: FEA Simulation VS Motor Design SW Results for Radial Rotor Configuration

Rotor Type: Radial	FEA Model Torque [Nm]	Motor Design SW Torque [Nm]	Error	Absolute Error	Percentage Error %
750rpm	59.1426	63.63	-4.4824	4.4824	7.045
1,500 rpm	59.142	64.08	-4.9417	4.9417	7.7113
6,000 rpm	59.1424	63.37	-4.2322	4.2322	6.678

Table 3.16: FEA Simulation VS Motor Design SW Results for V-shaped Rotor Configuration

Rotor Type: V-Shaped	FEA Model Torque [Nm]	Motor Design SW Torque [Nm]	Error	Absolute Error	Percentage Error %
750 rpm	53.6519	49.24	4.4096	4.4096	8.9549
1,500 rpm	53.6512	49.12	4.5271	4.5271	9.2156
6,000 rpm	53.6475	48.42	5.2324	5.2324	10.8074

Chapter 4

4.0 Performance Analysis

In this chapter the results were analyzed to characterize the performance of each rotor configuration. As stated in the previous chapter, simulations for various current and speeds were carried out to analyze the performance of each rotor configuration in this study. These operating points were filtered based on the maximum bus voltage to get all possible operating conditions for the rated current of the motor. In this study, it is assumed that the motor control strategy has been calibrated to operate the motor in its most efficient operating points. Therefore, the comparison of each rotor configuration was based on high efficiency operation. There was no dynamic analysis done in this study. All analysis was based on steady state conditions.

The analysis focused on the following performance characteristics:

- Maximum torque over the speed range
- Efficiency
- Synchronous Torque and Reluctance Torque Production
- Torque Ripple
- Parameter Variation

4.1 Maximum Torque over the Speed Range

Figure 4.1 shows the maximum torque production for all three rotor configurations at rated current for the speed range of 0 – 6000 rpm. When comparing maximum torque production in the constant torque region, the V-shaped rotor configuration achieves the highest torque at 70 Nm. The Flat rotor configuration achieves the second highest torque production at 67 Nm and the Radial rotor configuration produces the lowest torque at 60 Nm. Looking at speed greater than the rated speed of 1,500 rpm, the rotor configuration with the greater torque production in the flux-weakening region is the Flat rotor configuration with the exception of the V-shaped rotor configuration producing higher torque at 6000 rpm. In Figure 4.1, the Radial and Flat rotor configurations have a linear decline in torque production at higher speeds, whereas the V-shaped has more of an exponential decline.

Based on the above observations, there is no apparent front runner for maximum torque over all speed ranges of the motor. The torque production capabilities over the entire speed ranged for each rotor configuration gave very different results. The V-shaped rotor configuration has a high torque production in the constant torque region but falls below the Flat rotor configuration in the flux weakening region. The Flat rotor configuration has the best torque production in the flux weakening region with its high toque values and a linear decline as speed increases. The Radial rotor configuration has the least favorable torque capabilities of all three rotor configurations. However, it does have a linear decline in torque as speed increases in the flux weakening region.

4.2 Efficiency

The efficiency values for the toque versus speed for all three rotor configurations are shown in the Figures 4.2-4.4. The efficiency values represented in these figures are just the electromechanical conversion efficiency with no mechanical loss. However, since this study is only concerned with the effect of rotor configuration on performance, the mechanical losses have been neglected because the magnet placement has no effect on the wind and friction losses in the motor.

Figures 4.2-4.4 shows that all three rotor configurations have a high efficiency region above 90% for the majority of their torque and speed ranges. The rotor configuration with the highest efficiency region is the Radial rotor configuration with 97%. The next highest efficiency region is the 96% region that is achieved by all three rotor configurations. The Flat rotor configuration has the largest area with the 96% efficiency region, followed by the Radial and then the V-shaped.

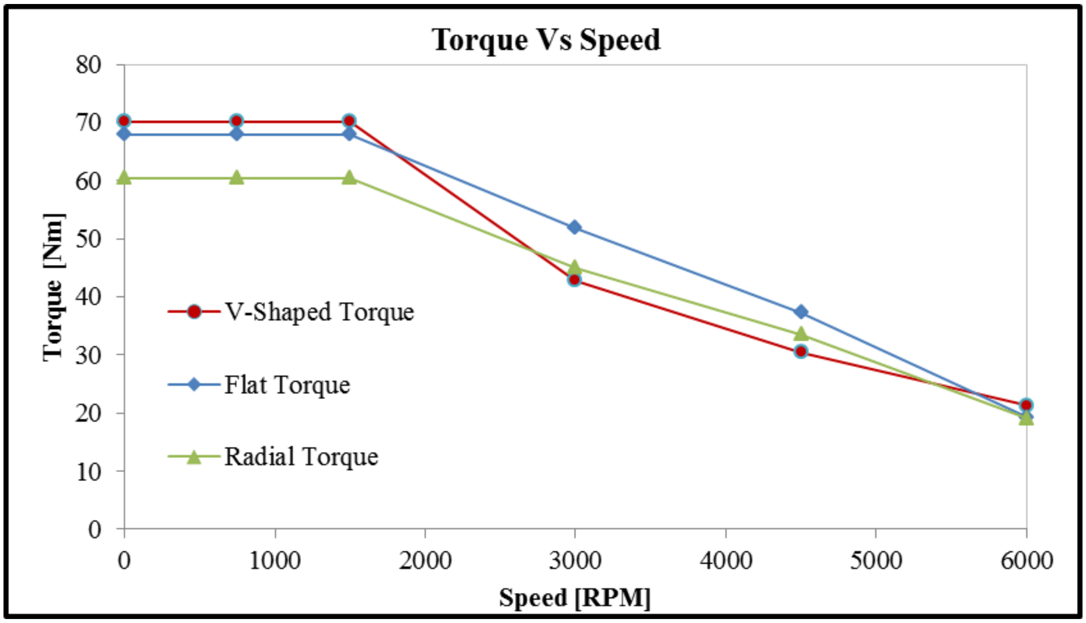

Figure 4.1: Torque vs Speed Curve

Overall, the Flat rotor configuration has the best balance between its torque production and efficiencies. The Radial rotor configuration has the highest efficiency region but has the lowest torque production capabilities compared to the other two rotor configurations. The V-shaped produces the highest torque value but also has lower efficiency values when compared to the other two rotor configurations.

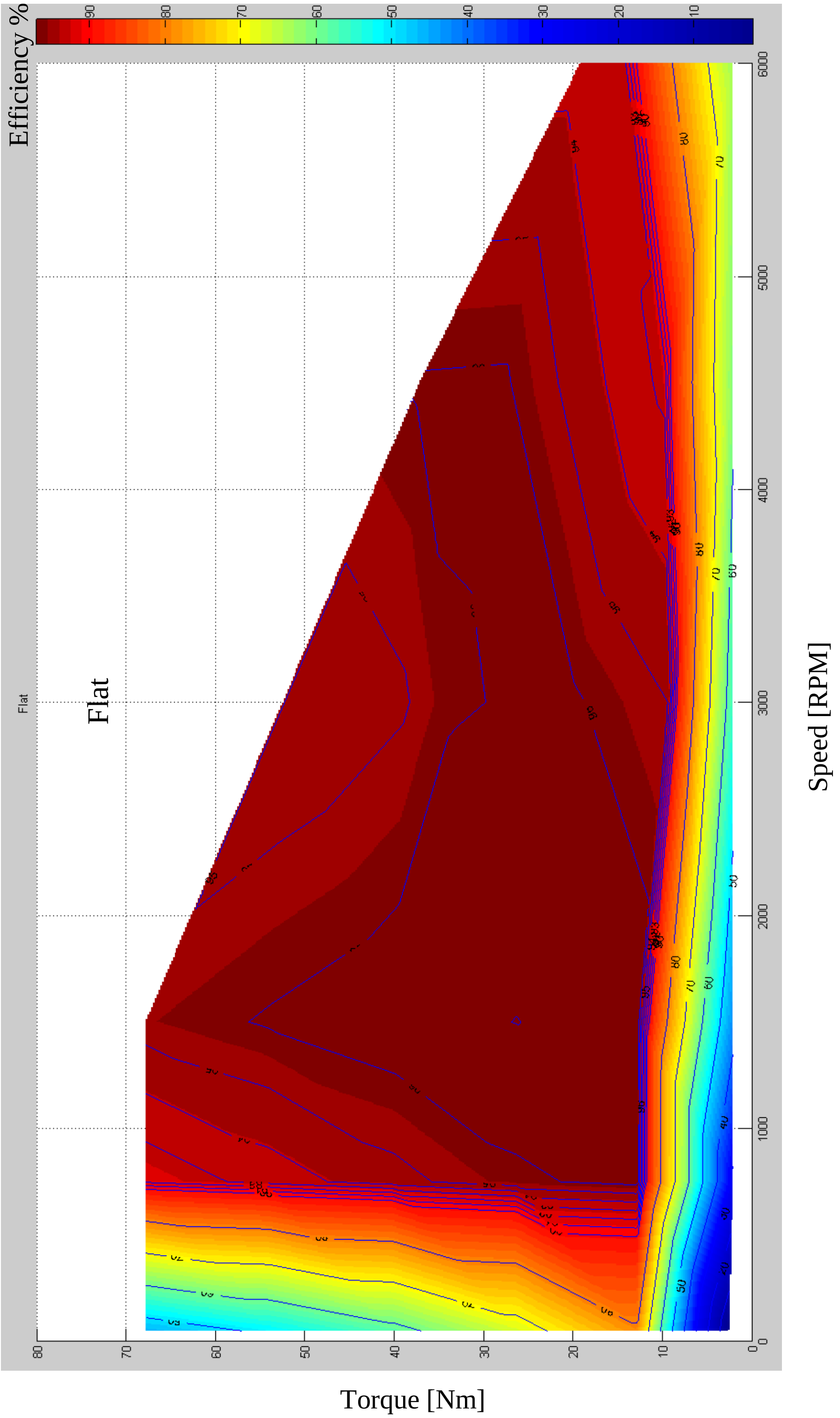

Figure 4.2: Torque vs Speed Efficiency Plot for Flat Rotor Configuration

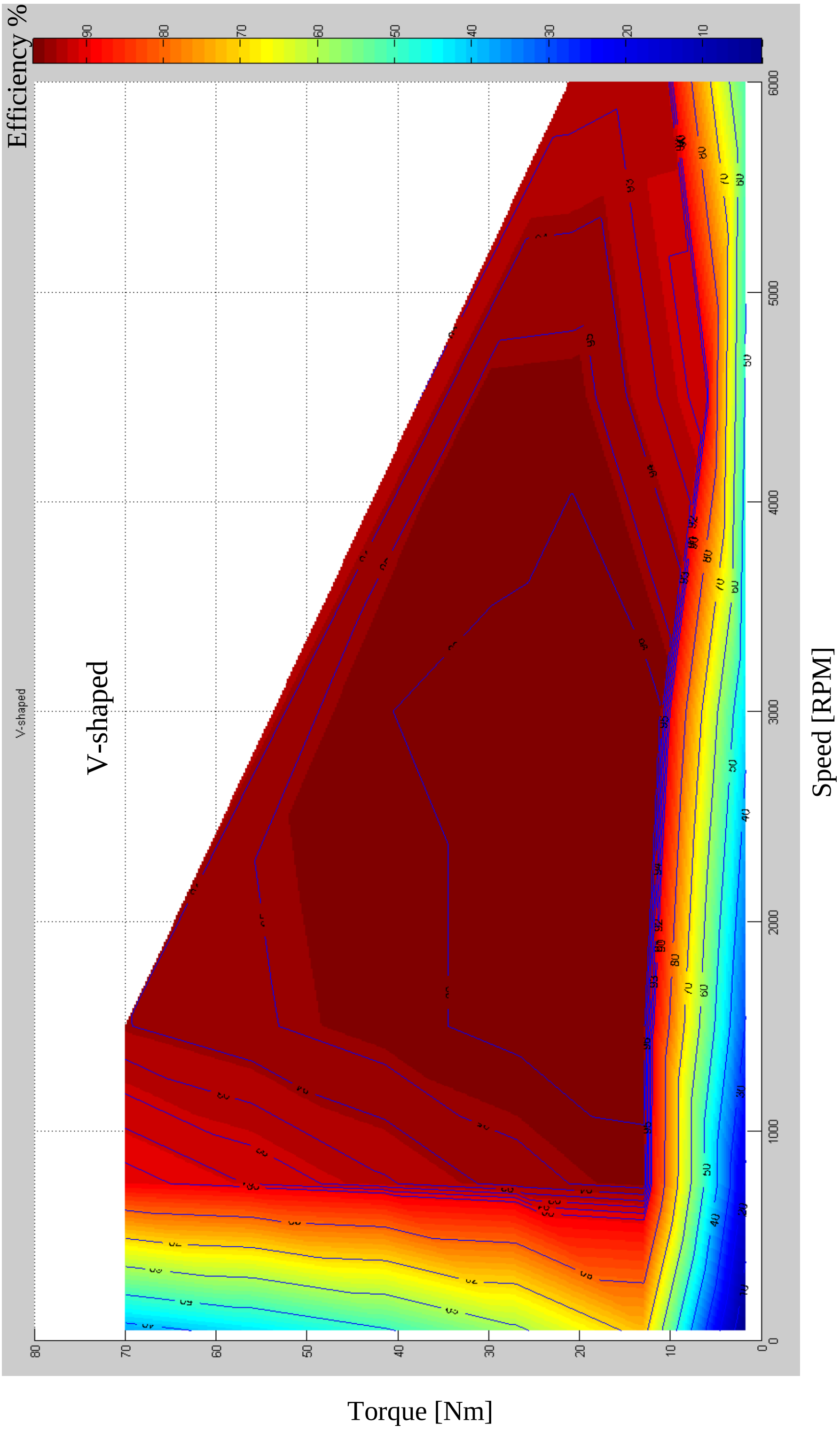

Figure 4.3: Torque vs Speed Efficiency Plot for V-shaped Rotor Configuration

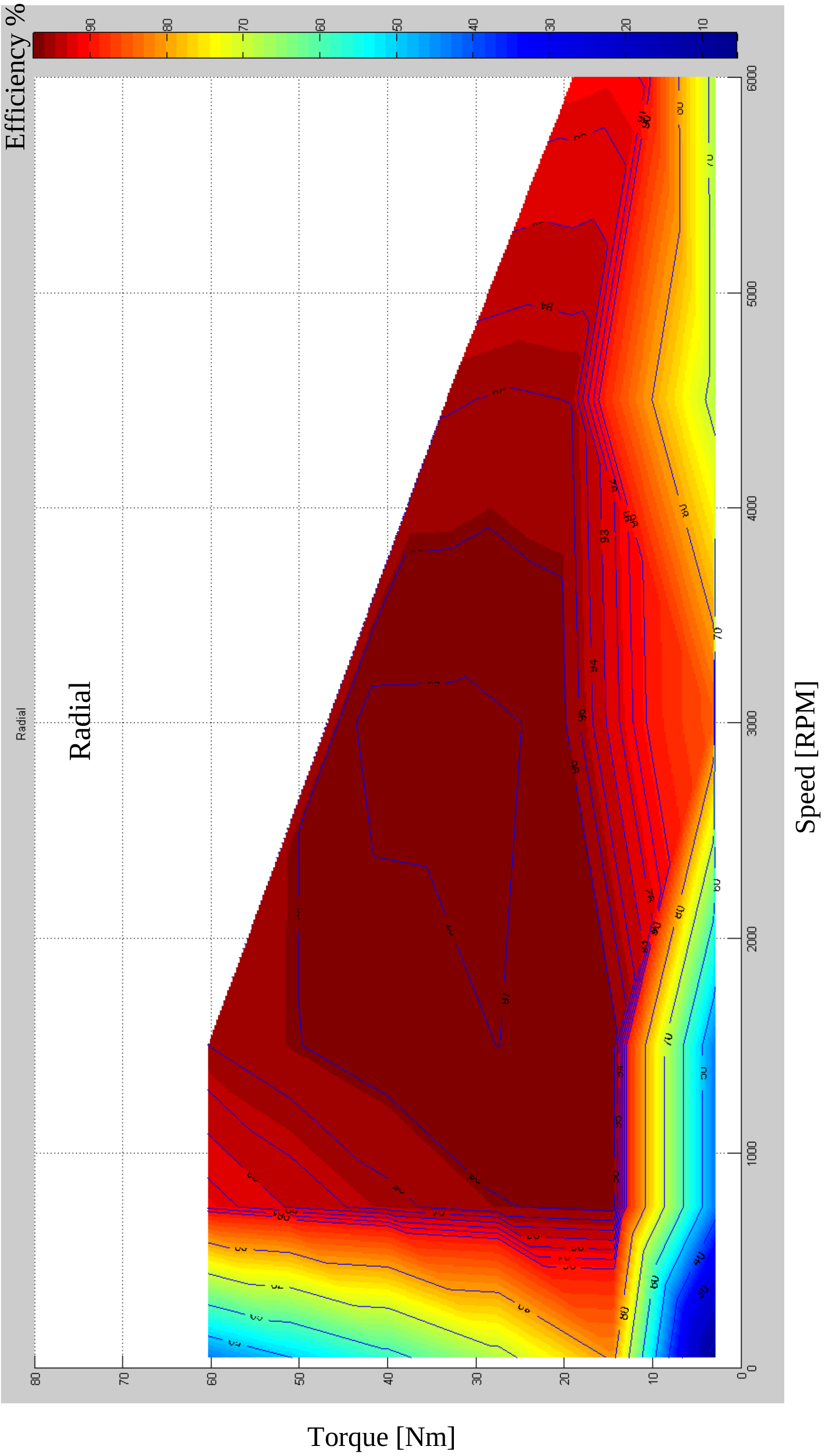

Figure 4.4: Torque vs Speed Efficiency Plot for Radial Rotor Configuration

4.3 Synchronous Torque and Reluctance Torque Production

As stated earlier, the reluctance torque production is possible when there is a negative difference between the *d* and *q*-axis inductance. The major advantage of an interior permanent magnet synchronous motor is its ability to produce reluctance torque as well as synchronous torque. Therefore, the reluctance torque and synchronous torque capabilities have been evaluated for all three rotor configurations. In the paragraphs below the torque production has been analyzed from the results of the FEA simulations at 1500 rpm. Also, an additional breakdown of synchronous and reluctance torque has been done by calculating the torque by parameters determined from the FEA results. In this section, it has been assumed that the parameters calculated are constant and do not vary with the operating condition of the motor.

The graphs in Figures 4.5, 4.6 and 4.7 for the rated speed of 1500 rpm, show that the Flat and V-shaped rotor configurations produce higher torque values at higher current angles. This is due to the fact that at higher current angles the machine is utilizing its reluctance torque capabilities by applying a negative *d*-axis current. However, the Radial rotor configuration torque capabilities do not produce much more torque when *d*-axis current is applied to the machine as compared to the Flat and V-shaped rotor configurations. These torque characteristics of the Flat and V-shaped rotor configurations are caused by high rotor saliency, whereas the Radial rotor configuration has a low rotor saliency. A further analysis into the reluctant torque capabilities is done by breaking down the torque into the synchronous and reluctance torque component of each rotor configuration at its maximum torque value. This was done by using parameters determined from the FEA results and applying them to equations (2.63) and (2.64) in chapter 2. Using these equations, the max torque breakdown for each rotor configuration at the rated current and speed of the motors is listed in Table 4.1. The total torque calculated using the parameters determined from FEA and equations (2.63) and (2.64) are within 1 % of the average torque determined by the FEA simulations. Therefore, this gives validity to the torque breakdown calculated using equations (2.63) and (2.64).

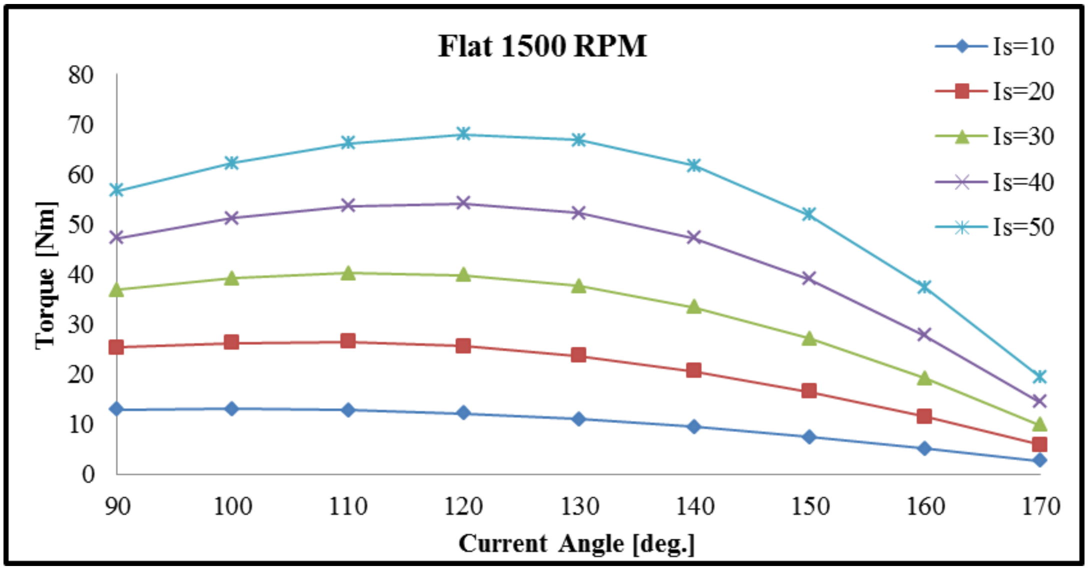

Figure 4.5: Flat Torque Production Graph for Varying Current Magnitude and Angle

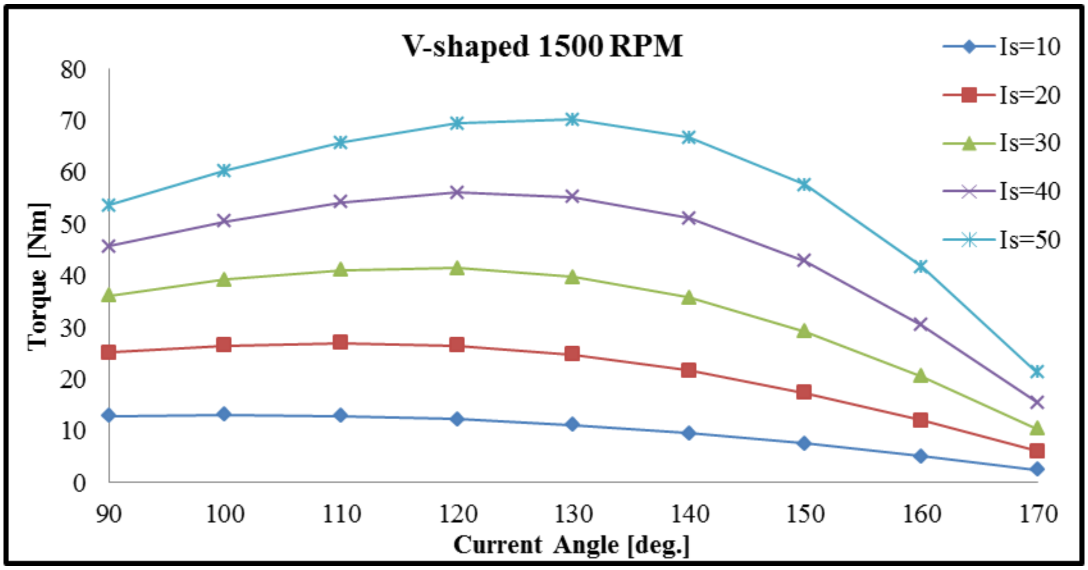

Figure 4.6: V-Shaped Torque Production Graph for Varying Current Magnitude and Angle

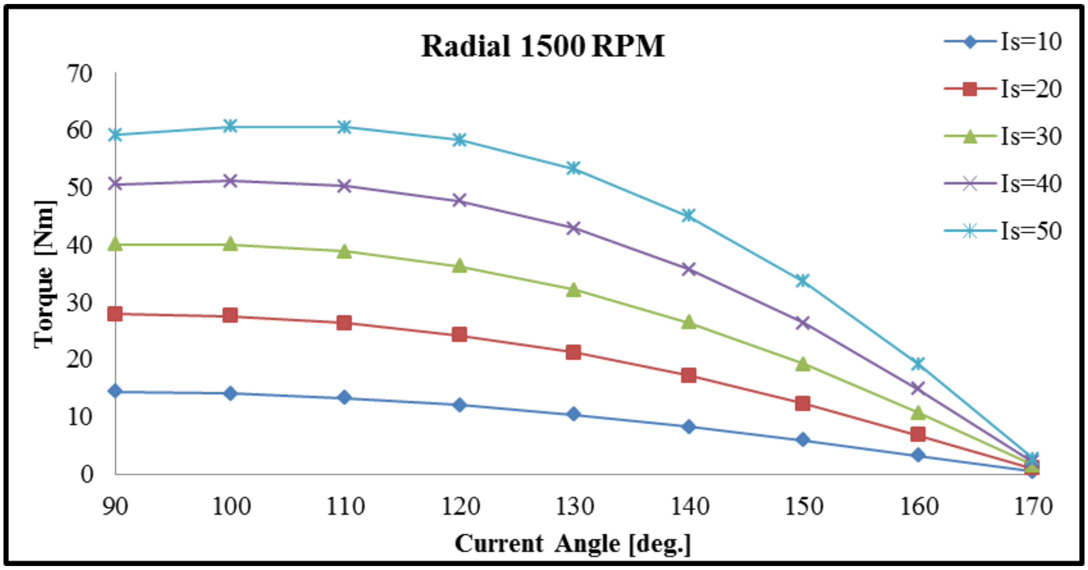

Figure 4.7: Radial Torque Production Graph for Varying Current Magnitude and Angle

Table 4.1: Reluctance and Synchronous Torque for Rated Condition

Flat (I_s=50, α=120)	
L_d-L_q [H]	-0.00227
Reluctance Torque [Nm]	14.75
Synchronous Torque [Nm]	53.34
Total Torque [Nm]	68.09
PM Flux Linkage Wb-turns	0.2053
Radial (I_s=50, α=110)	
L_d-L_q [H]	0.000477
Reluctance Torque [Nm]	-2.29874
Synchronous Torque [Nm]	63.10
Total Torque [Nm]	60.8
PM Flux Linkage Wb-turns	0.2239
V-shaped (I_s=50, α=130)	
L_d-L_q [H]	-0.00314
Reluctance Torque [Nm]	23.2
Synchronous Torque [Nm]	47.2
Total Torque [Nm]	70.42
PM Flux Linkage Wb-turns	0.2055

The value that is used to determine the synchronous torque capabilities of each rotor configuration is the permanent magnet flux linkage, which is listed in Table 4.1. The highest permanent magnet flux linkage listed in Table 4.1 belongs to the Radial rotor configuration. Therefore, the Radial rotor configuration has the highest synchronous torque capabilities of all three rotor configurations. The permanent magnet flux linkages of the Flat and V-shaped rotor configurations are relatively close in value, thus giving them the same amount of synchronous torque capabilities.

The next quantity to analyze in Table 4.1 is the negative difference between L_d and L_q which gives the reluctance toque capabilities of each rotor configuration. The V-shaped rotor has the highest negative difference between L_d and L_q which means it has the highest reluctance torque capabilities of all three rotor configurations. The Flat rotor configuration has the next highest negative difference between L_d and L_q which allows it to produce the next highest reluctance torque. The Radial rotor configuration has a positive difference between L_d and L_q which produces a negative reluctance torque.

In summary, the highest synchronous torque production is achieved by the Radial rotor configuration due to its high permanent magnet flux linkage. The highest reluctance torque capabilities are achieved by the V-shaped rotor configuration having the highest negative difference between L_d and L_q. However, an interesting observation to note is that the Radial rotor configuration had achieved the highest torque value when a q and a negative d-axis current was applied. This resulted in the Radial rotor configuration producing negative reluctance torque. Based on the assumption taken in this section that the parameters were constant, the highest torque achieved by the Radial rotor configuration should have occurred when there was only q-axis current being applied. However, the maximum torque achieved by the Radial rotor configuration occurred with both q and negative d-axis currents being applied. This is due to the fact the parameters are not constant and change depending on operating conditions caused by the effect of saturation of the machine [56]. A more detailed analysis into the parameter variations for different operating conditions will be done in a later section.

4.4 Torque Ripple Analysis

Torque ripple in this study has been conducted on the peak torque values for each rotor configurations at various speeds. The back EMF waveform will be analyzed for harmonic content due to its contribution to the torque ripple. Also, the cogging torque of each rotor configuration will be analyzed.

The torque ripple for the peak torque values at 750, 1500, 3000, 4500 and 6000 rpm are plotted in Figure 4.8. In comparing the torque ripple of each rotor configuration, the Radial rotor configuration has the highest torque ripple value for every speed. The Flat and V-shaped rotor configurations have relatively the same values of torque ripple except at the speed of 4500 rpm where the V-shaped has a slightly higher torque ripple.

The back EMF waveform of each rotor configuration is plotted in Figure 4.9 for the speed of 3000 rpm. As stated earlier in chapter 2, the torque ripple can be attributed to non-fundamental harmonic components in the back EMF waveforms. These non-fundamental harmonics make the back EMF waveform vary from the ideal sinusoidal waveform.

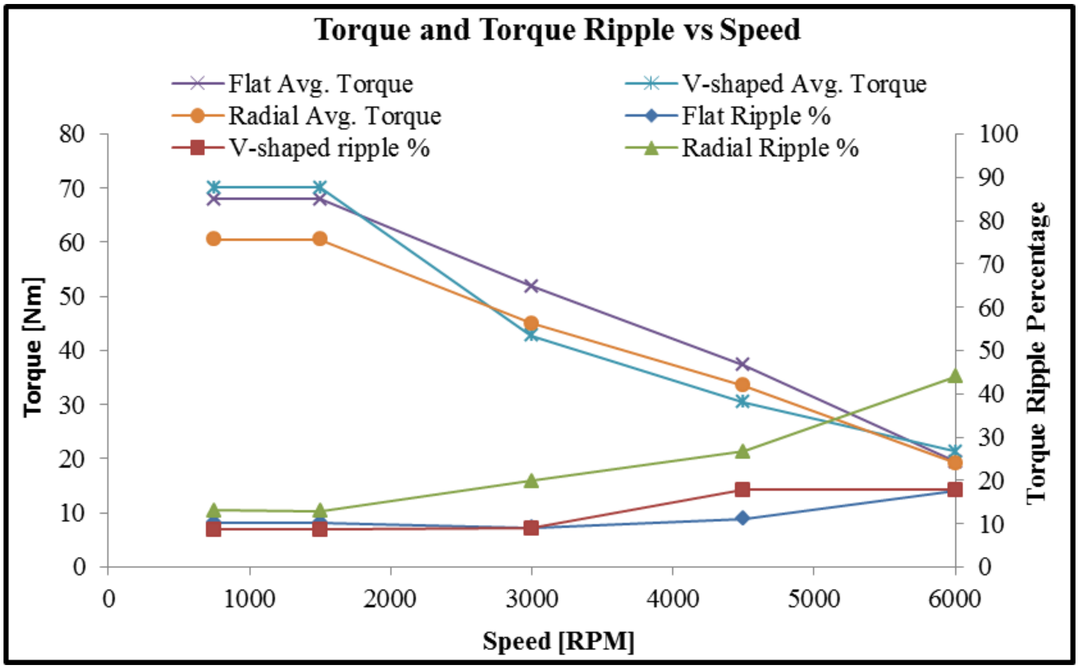

Figure 4.8: Torque Ripple vs Speed

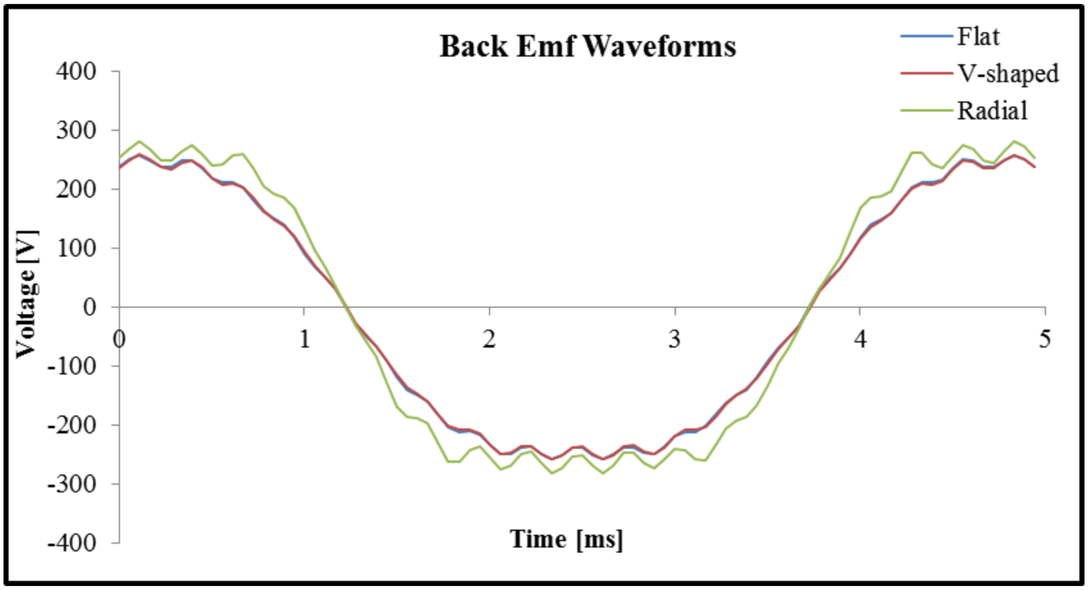

Figure 4. 9: Back EMF Waveforms of All Rotor Configurations

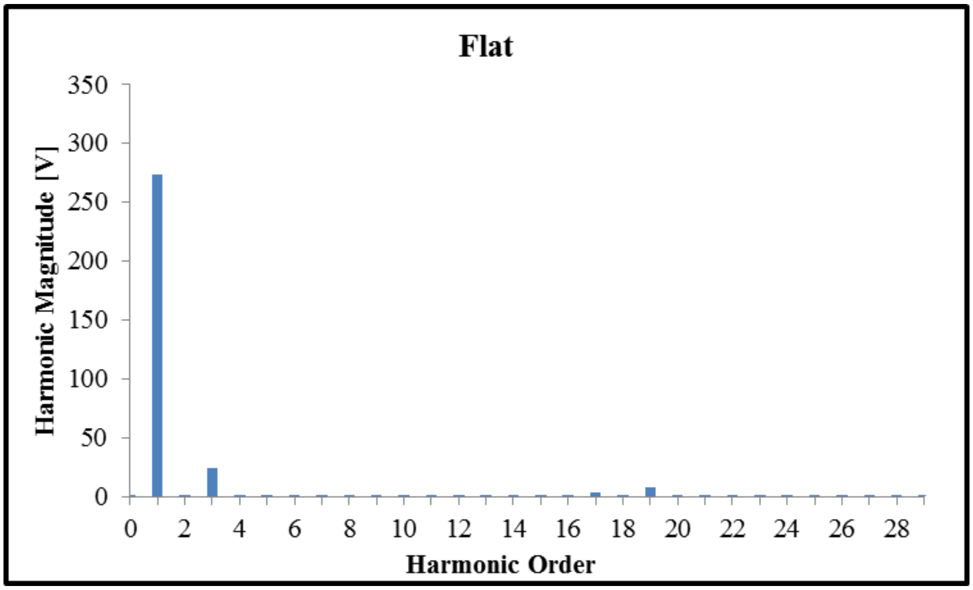

Figure 4.10: Harmonic Spectrum of Flat Rotor Back EMF Waveform

Figure 4.9 shows that the Flat and V-shaped back EMF's are very similar and overlap each other. The Radial rotor configuration's back EMF waveform has the highest value.

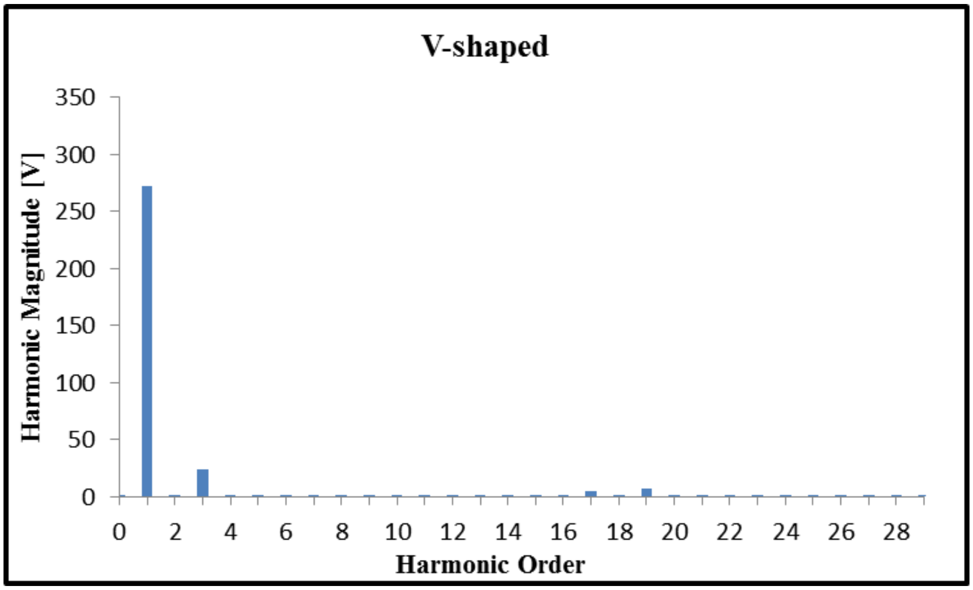

Figure 4.11: Harmonic Spectrum of V-Shaped Rotor Back EMF Waveform

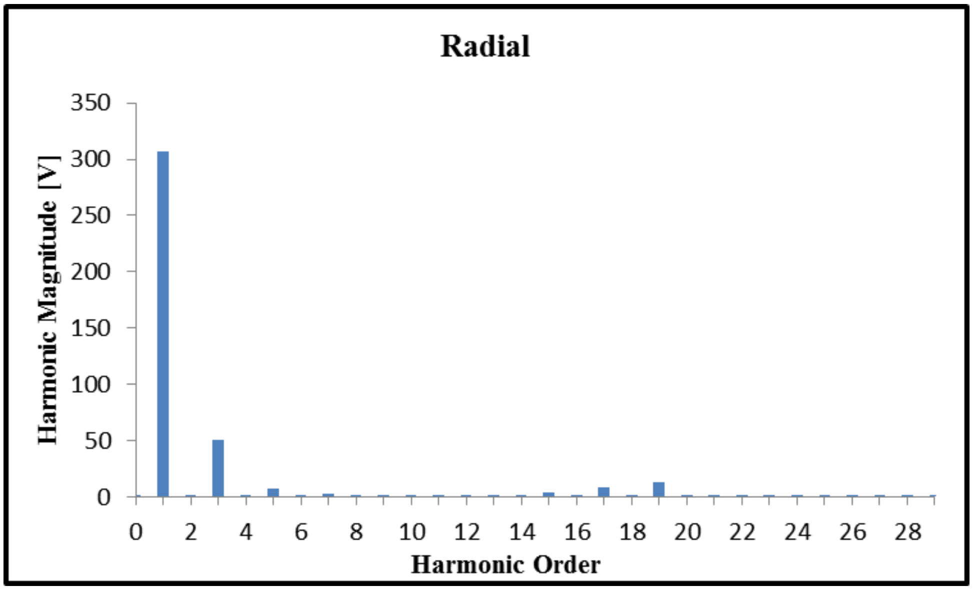

Figure 4.12: Harmonic Spectrum of Radial Rotor Back EMF Waveform

The harmonic content of the back EMF waveforms are shown in Figures 4.10-4.12 for all three rotor configurations. Also the total harmonic distortion (THD) is given in Table 4.2. In analyzing the harmonic components of the Flat and V-shaped rotor configurations, there are slight differences in their harmonic content. This would be expected since their back EMF waveforms are nearly identical. The Radial rotor configuration has the highest amount of harmonic content with the largest 3rd, 5th, 17th and 19th harmonic components. The higher harmonic content of the Radial rotor configuration can also be seen by its THD shown in Table 4.2. The high harmonic content in the back EMF waveform would explain why the Radial rotor configuration in this study has the highest torque ripple of all three rotor configurations.

Another contributor of the torque ripple is the cogging torque produced by the interaction of the permanent magnets and the stator teeth. This cogging torque was evaluated by simulating the rotor spinning without any current applied to the machine and then measuring the resulting torque pulsations. The simulation results of the peak cogging torque for each rotor configuration are listed in Table 4.3. In comparing the torque ripple values of all three rotor configurations, the Radial rotor configuration has the highest cogging torque value, with the V-shaped rotor configuration having the next highest, followed by the Flat rotor configuration having the lowest cogging torque value.

In summary, the Radial rotor configuration is observed to have the highest torque ripple when compared to the other two rotor configurations. This high torque ripple can be attributed to the high harmonic content in the back EMF waveform and also the high cogging torque. However, due to the fact that there was no design optimization done on any of the rotor configurations in this study, it should not be assumed that every Radial rotor configuration design has a high torque ripple. If any conclusion could be drawn from this analysis of the torque ripple, it is that torque ripple can be affected by the rotor configuration.

Table 4.2: THD of Flat, V-shaped and Radial Rotor Configurations Back EMF

Rotor Configuration	Flat	V-shaped	Radial
THD %	9.44	9.43	17.54

Table 4.3: Peak Cogging Torque of the Flat, V-shaped and Radial Rotor Configurations

Rotor Configuration	Flat	V-shaped	Radial
Peak Cogging Torque [Nm]	0.0107	0.0697	0.6081

4.5 Parameter Variation Due to Loading Condition

In order to understand the effect of the rotor configuration on the parameter variations due to the loading condition, the author had to not only analyze the parameter variation due to the magnitude and angle of the stator current, but also had to conduct further simulations to characterize the parameter variations due to the applied *d* and *q*-axis currents.

4.5.1 Parameter Variation Due to Applied Current Magnitude and Angle

The dependency of the parameters on the loading condition has been documented by many authors [56]-[64]. Parameter variation due to the loading condition can be attributed to the saturation of the machine at different loading conditions [61], [64]. Looking at the Figures 4.13-4.18 for the base speed of each rotor configuration, one can see that there is a dependence of current and current angle on the inductance parameters. Taking the assumption that the flux linkage of the permanent magnets λ_{pm} is constant and not affected by the loading condition [62], one can make the following observations based on the Figures 4.13-4.18. The *d*-axis profile seems to have the same trend for all three rotor configurations since it varies very little after 120 degrees. This little variance of the *d*-axis inductance is caused by the negative *d*-axis current reducing the saturation of the machine [63]. The *q*-axis inductance for each rotor configuration does vary with the magnitude and angle of the current being applied to the motor [32], [63]. The *q*-axis has highly saturated magnetic steel with a very small air gap, thus allowing the *q*-axis to saturate and affect the *q*-axis inductance.

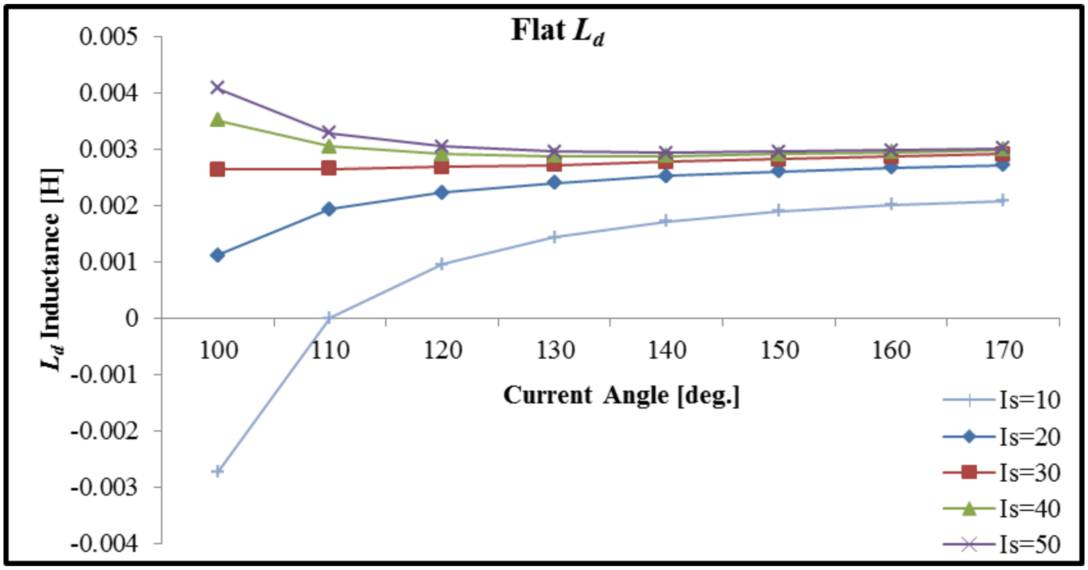

Figure 4.13: Flat *d*-axis Inductance Variation with Current Magnitude and Angle

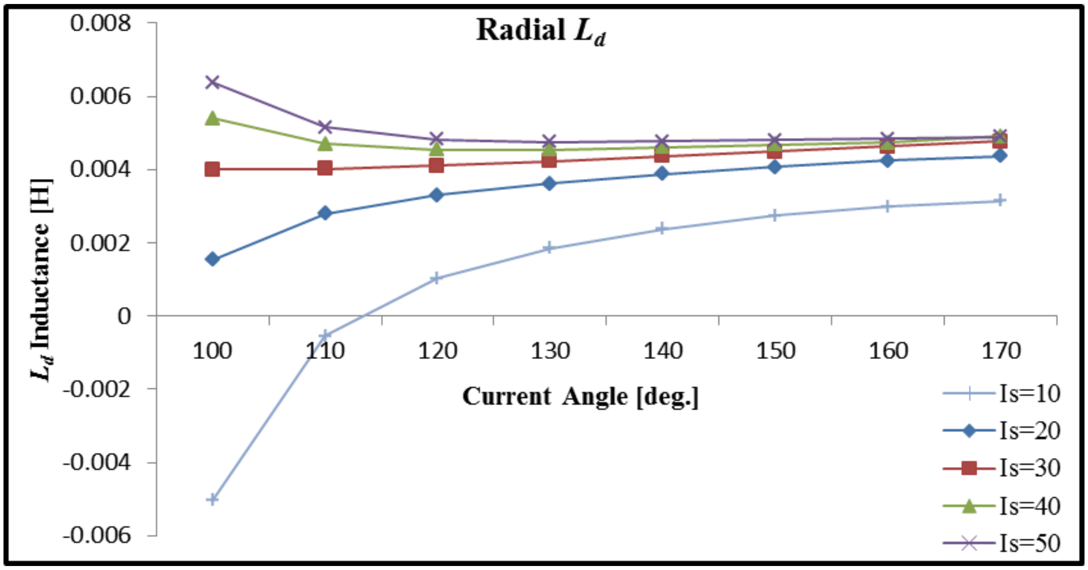

Figure 4.14: Radial *d*-axis Inductance Variation with Current Magnitude and Angle

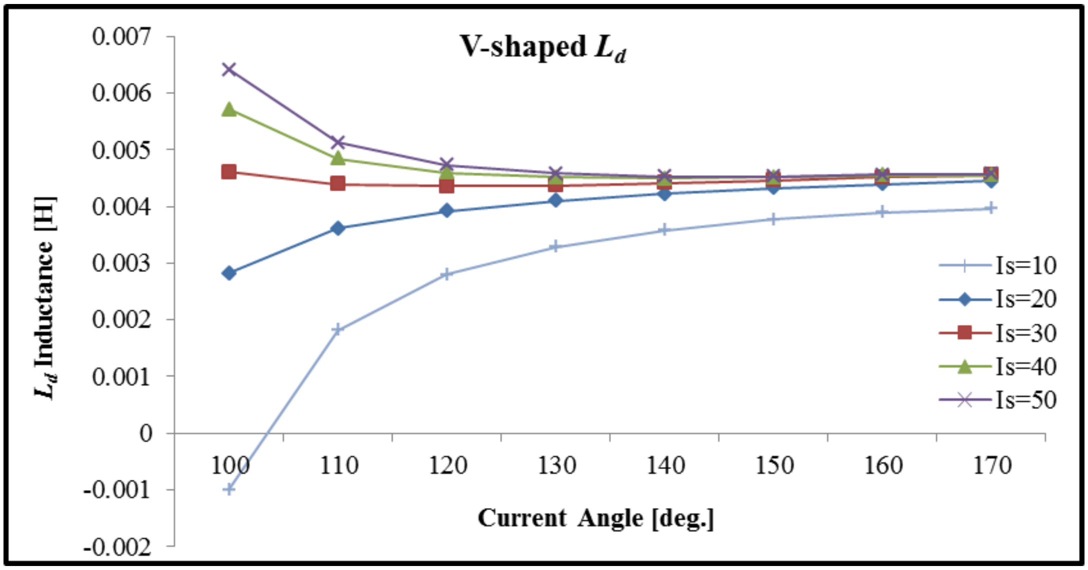

Figure 4.15: V-shaped *d*-axis Inductance Variation with Current Magnitude and Angle

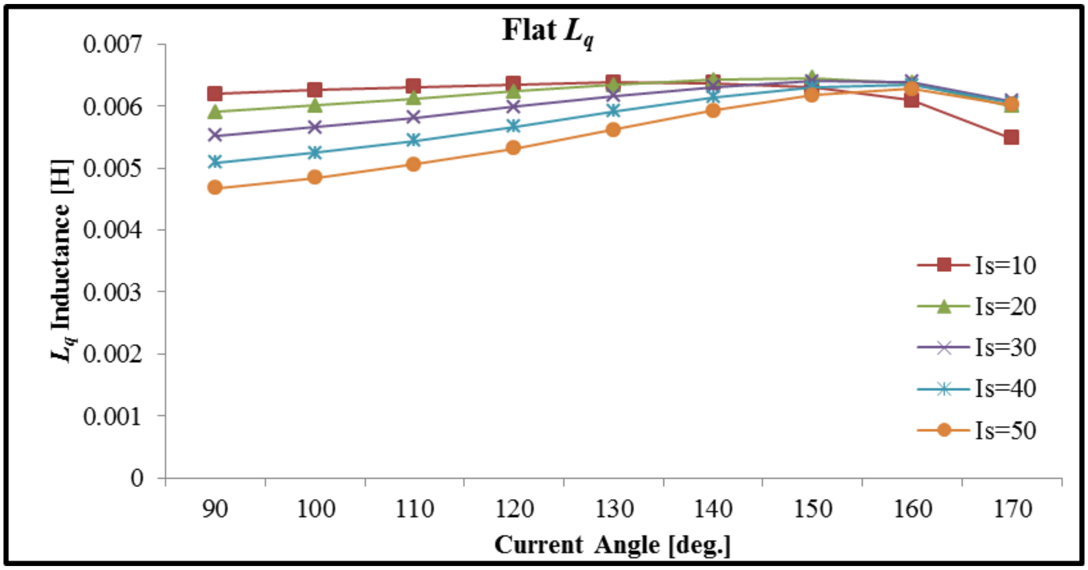

Figure 4.16: Flat *q*-axis Inductance Variation with Current Magnitude and Angle

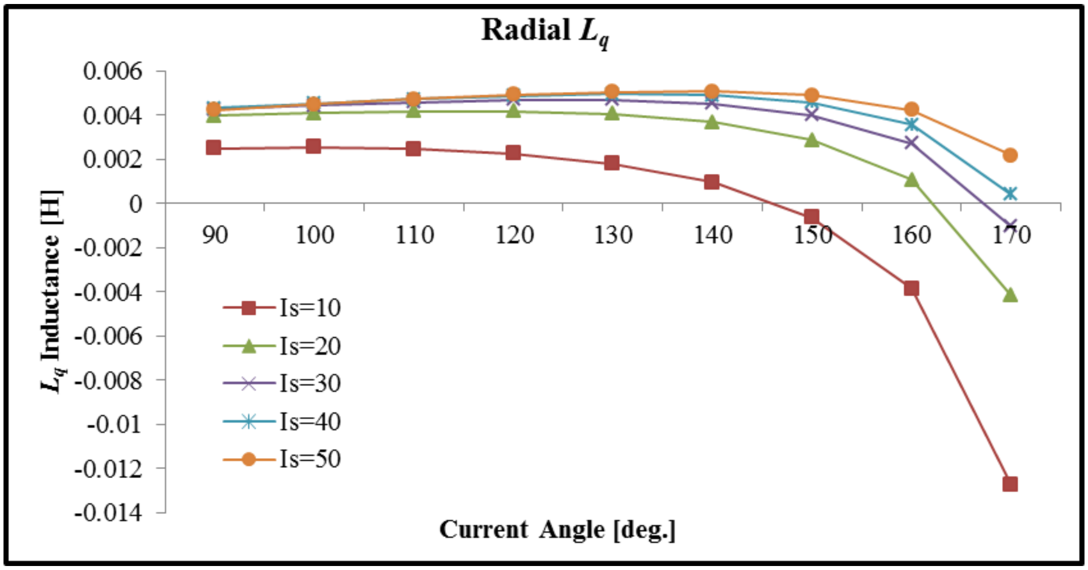

Figure 4.17: Radial *q*-axis Inductance Variation with Current Magnitude and Angle

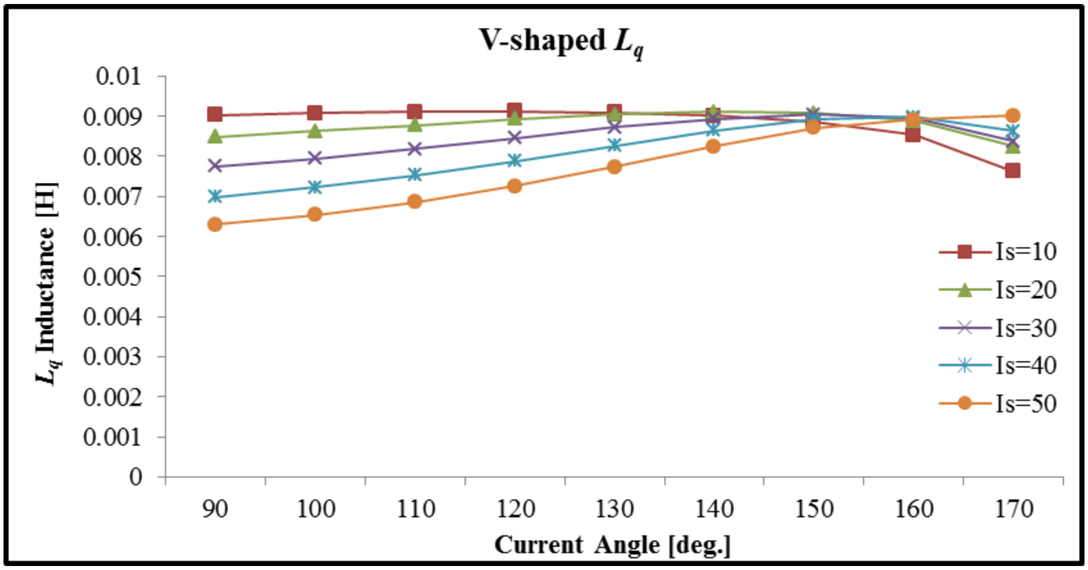

Figure 4.18: V-shaped *q*-axis Inductance Variation with Current Magnitude and Angle

In Figures 4.13-4.15, the *d*-axis inductance for the values at the current angle equal to 100 degrees where the *d*-axis current is low, one can see that for various *q*-axis current the value of the d-axis inductance varies. The *d*-axis flux linkage equation (4.1) which is used to calculate the *d*-axis inductance shows no dependence of other variables other than the *d*-axis current i_d. Assuming a constant value of permanent magnet flux linkage λpm, one can conclude that there is a dependency of *q*-axis current on the *d*-axis inductance that is not taken into account by formula (4.1).

$$\begin{aligned} \lambda_d &= L_d I_d + \lambda_{pm} \\ \lambda_q &= L_q I_q \end{aligned} \tag{4.1}$$

It has been shown by numerous authors that the ideal decoupled *d* and *q*-axis parameters, such as the flux linkage and inductance, do depend on both the *d* and *q*-axis currents [56], [65]-[69]. This coupled behavior of the *d* and *q*-axis quantities is sometimes referred to as cross magnetization. To characterize the cross magnetization effect of the currents on the motor parameters, a separate set of simulations were conducted on each rotor configurations at the base speed of 1500 rpm. At this base speed, the *d* and *q*-axis currents were varied to characterize their effect on the parameter variation. The results are discussed below.

4.5.2 *d* and *q*-axis Flux Path

To better understand the results of the parameter variation due to the *d* and *q*-axis currents, view Figures 4.19-4.21 which show the flux paths of the permanent magnets, *q*-axis current and *d*-axis current for each rotor configuration. The d-axis for all three rotor configurations can be determined from the main flux path setup by the permanent magnets which are shown in Figure 4.19a, 4.20a and 4.21a. The *q*-axis of all three rotor configuration is located 90 electric degrees or 22.5 mechanical degrees, ahead of the *d*-axis. The flux path due to the *q*-axis current is shown in Figures 4.19b, 4.20b and 4.21b. This flux path travels in the same vicinities in all three rotor configuration with some minor alterations due to the placement of the magnets. In the Flat and V-shaped configurations, the main *q*-axis flux path enters the *q*-axis of the rotor. Then, it travels through the rotor across the tops of the magnets, with some flux lines running beneath the magnets. In the Radial rotor configuration, the *q*-axis flux enters just off the *q*-axis of the rotor due to the presence of the permanent magnets and the flux barriers. Then, the flux travels across the top of the poles just like the V-shaped and Flat configuration, with some flux traveling beneath the magnets. The path of the negative *d*-axis flux due to the negative *d*-axis current is shown in Figures 4.19c, 4.20c and 4. 21c. The negative *d*-axis flux path for all three rotor configurations are very similar and vary slightly due to the placement of the permanent magnets. The negative *d*-axis flux path travels opposite the permanent magnet flux. It then travels through the flux barrier bridges near the magnet edges to reach the other pole for the return path through the stator. This visual understanding of the flux path in the *d* and *q*-axis will be used to analyze the parameter variation due to the applied *d* and *q*-axis currents.

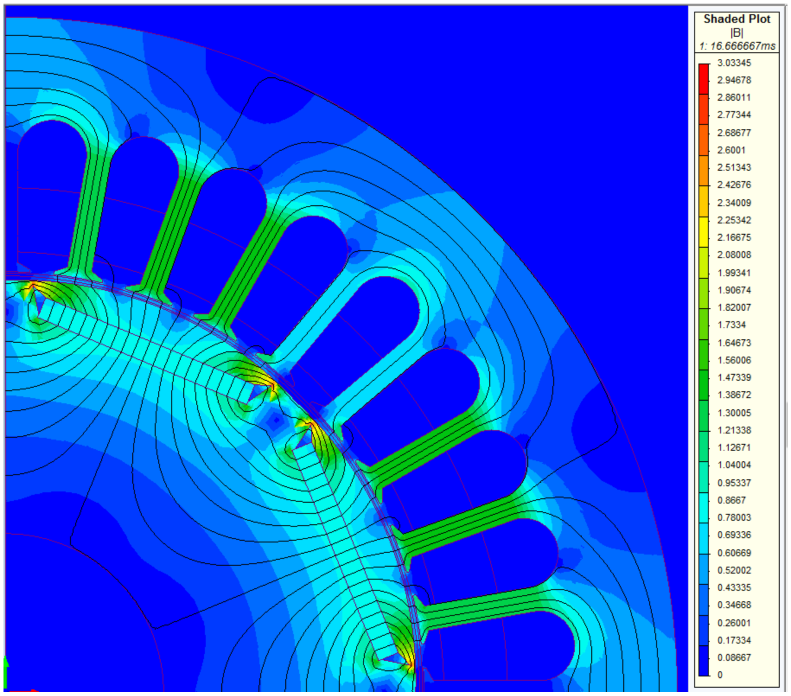

a) Permanent Magnets Only

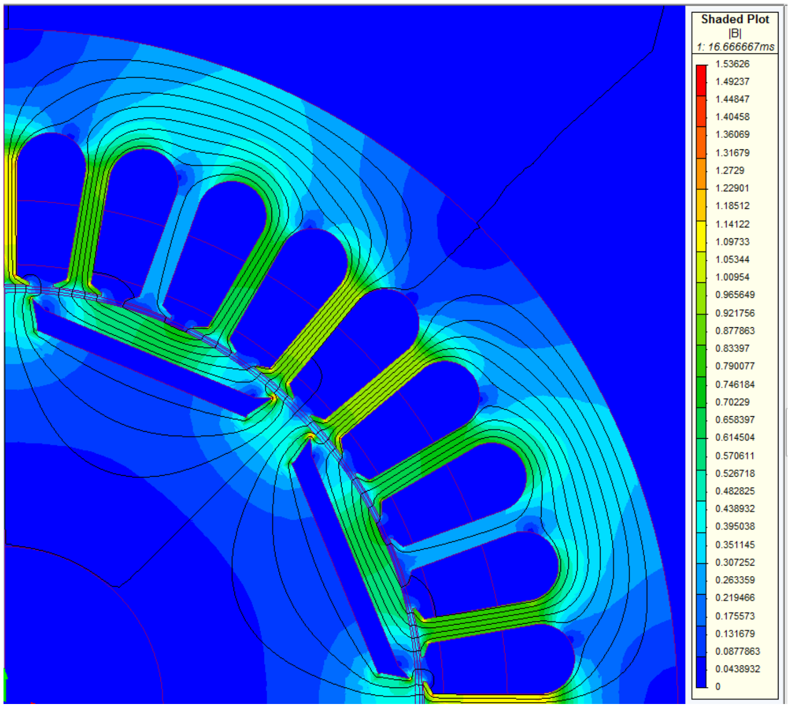

b) *q*-axis Current only

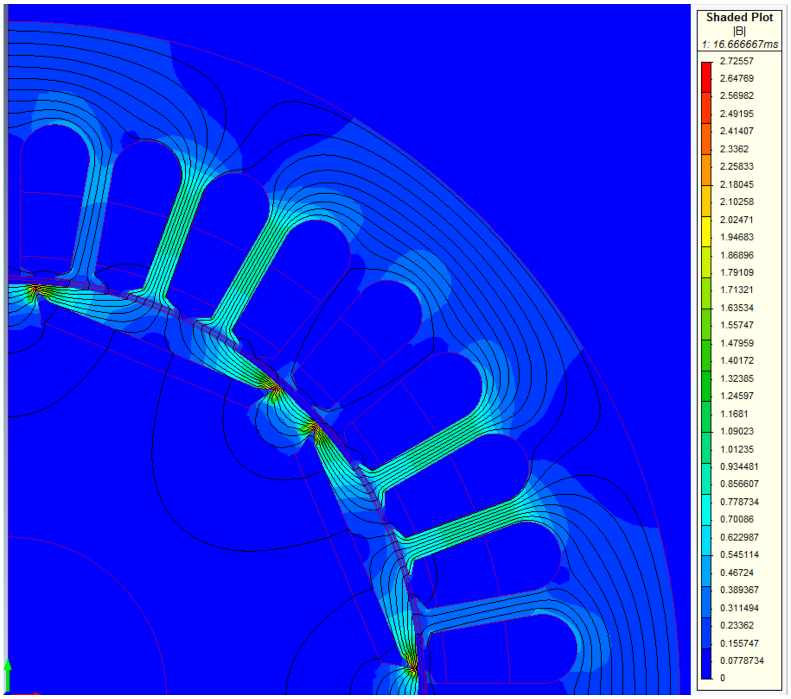

c) *d*-axis Current Only

Figure 4.19: Flat Rotor Configuration's Flux Paths

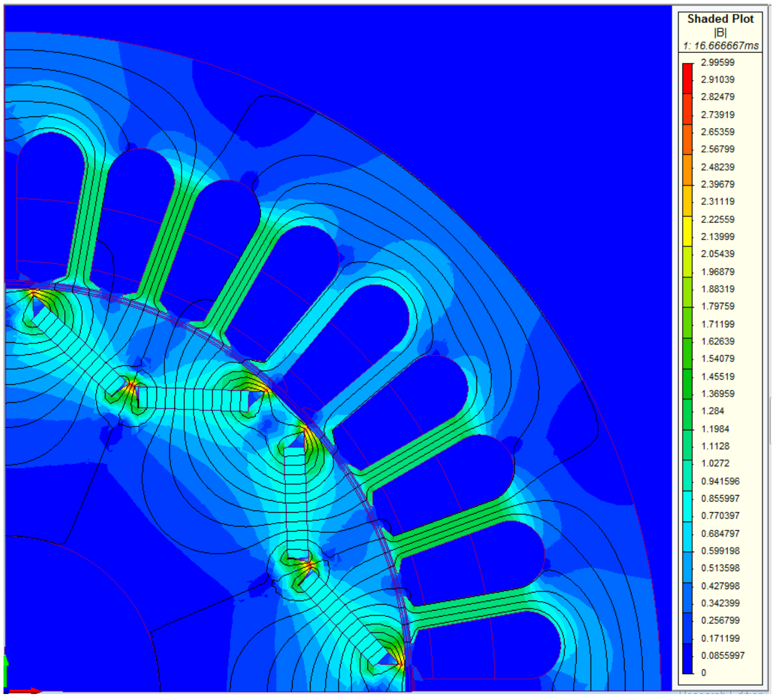

a) Permanent Magnets Only

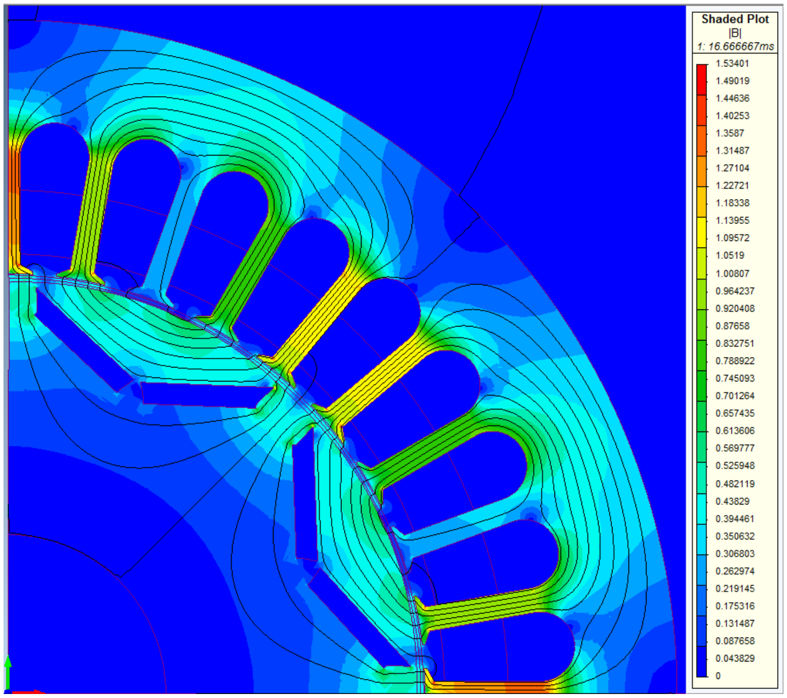

b) *q*-axis Current Only

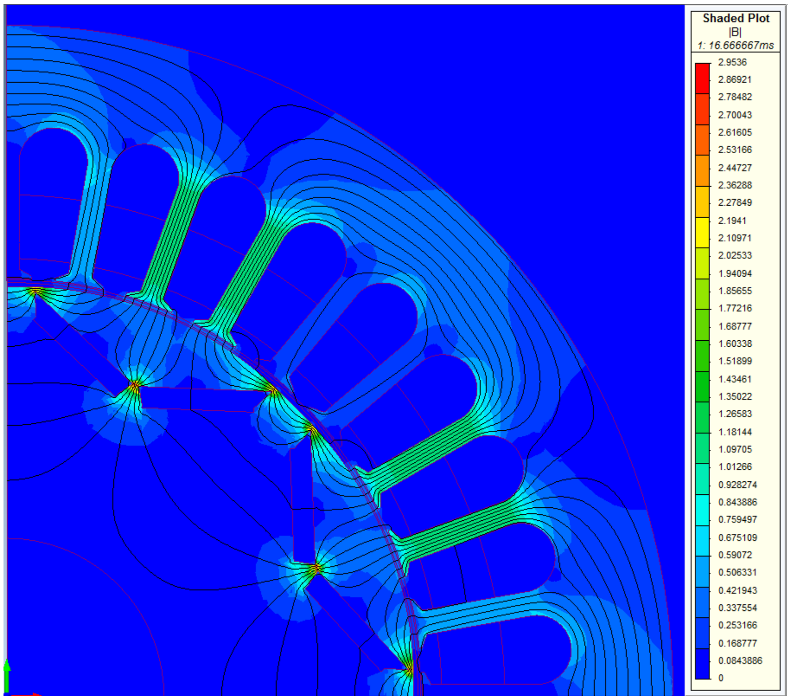

c) Negative *d*-axis Current Only

Figure 4.20: V-shaped Rotor Configuration’s Flux Paths

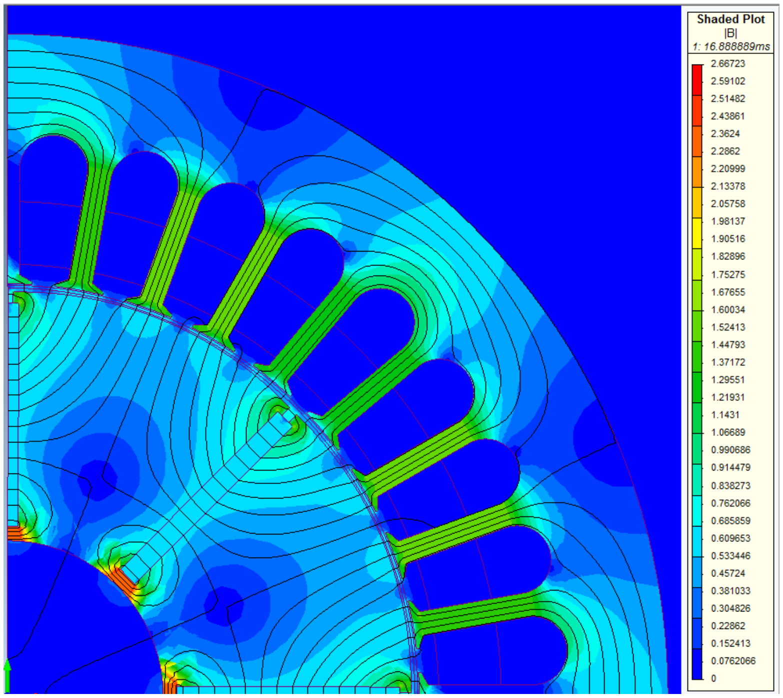

a) Permanent Magnets Only

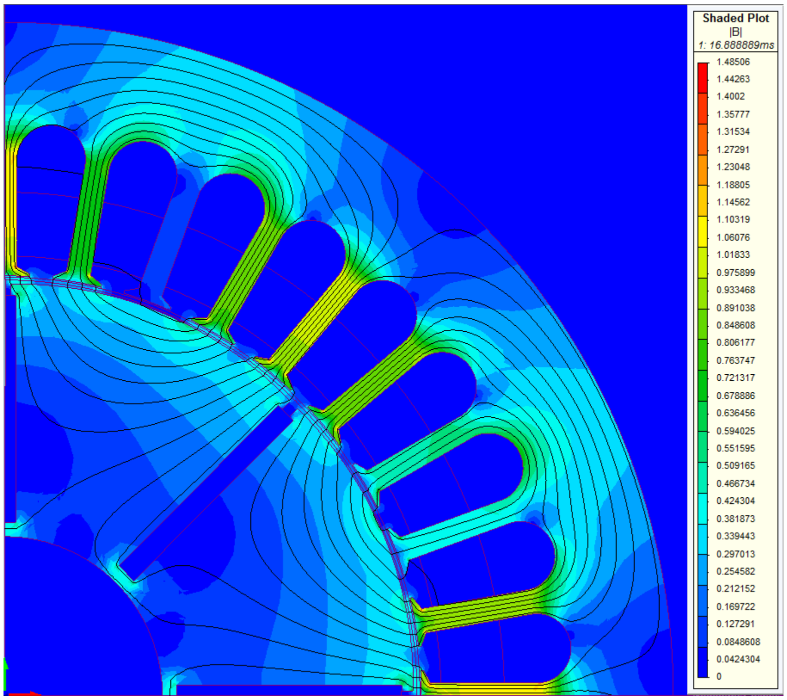

b) *q*-axis Current Only

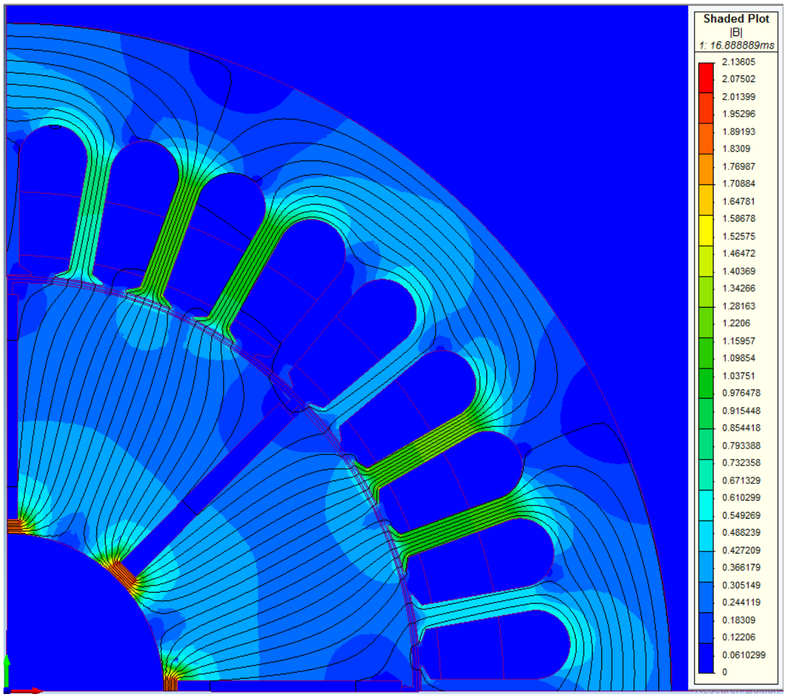

c) Negative *d*-axis Current Only

Figure 4.21: Radial Rotor Configuration's Flux Paths

4.5.3 *q*-axis Parameter Variation

The *q*-axis flux linkage determined by the parameter variation simulations for all three rotor configurations are shown in Figures 4.22, 4.23 and 4.24. In all three rotor configurations, the flux linkage has a non-liner saturation characteristic to its curve as I_q is increased. However at higher values of I_q, it can been seen that by applying higher values of negative *d*-axis current, decreases the saturation effect on the *q*-axis flux linkage. This results in an increase in the *q*-axis flux linkage. This negative *d*-axis effect on the *q*-axis flux linkage can be observed in the flux plots shown in Figures 4.25, 4.26, and 4.27.

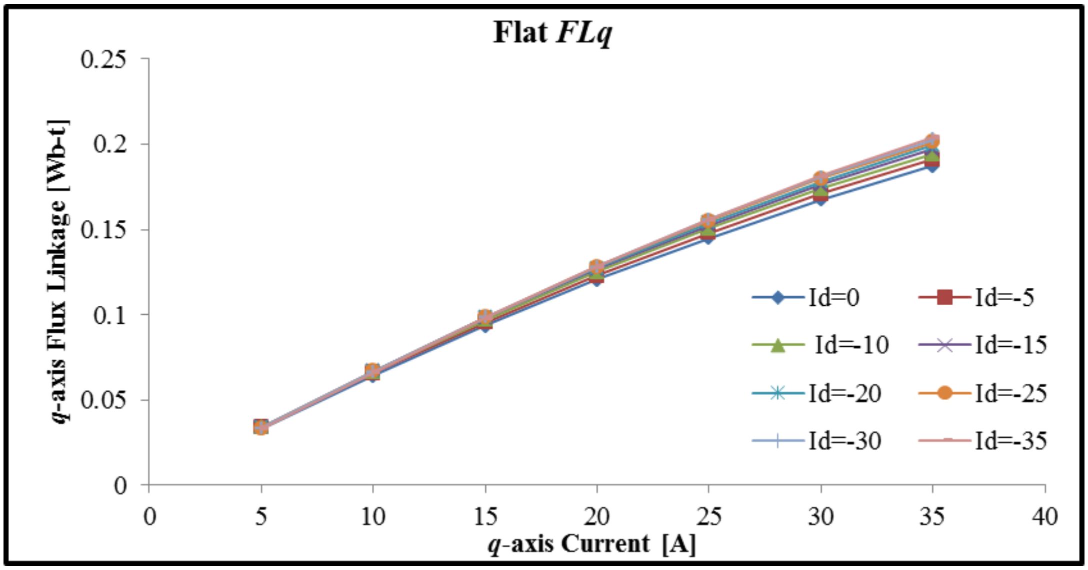

Figure 4.22: Flat Variation of *q*-axis Flux Linkage with Applied *d* and *q*-axis Currents

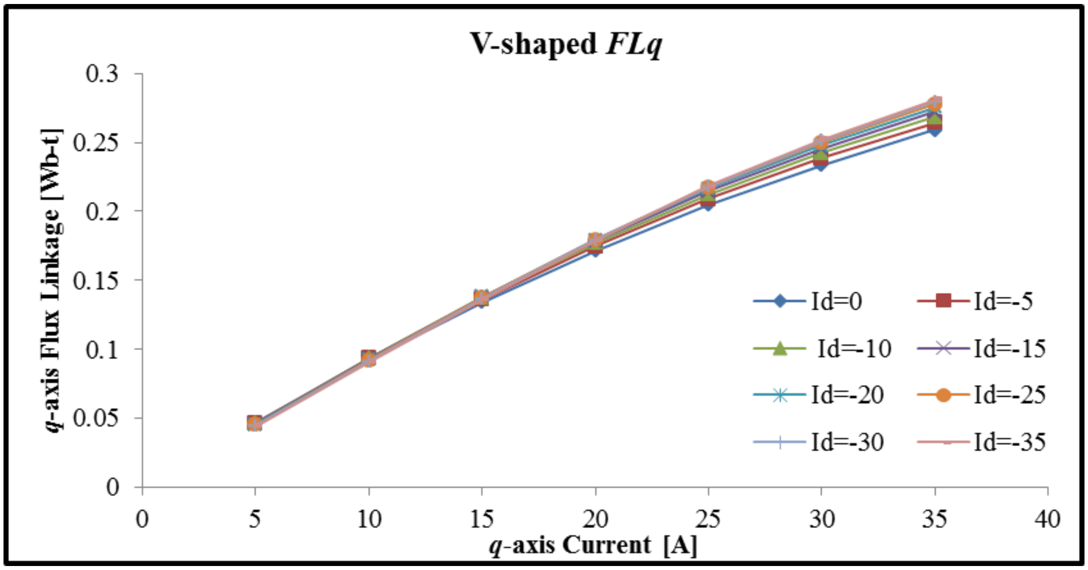

Figure 4.23: V-Shaped Variation of *q*-axis Flux Linkage with Applied *d* and *q*-axis Currents

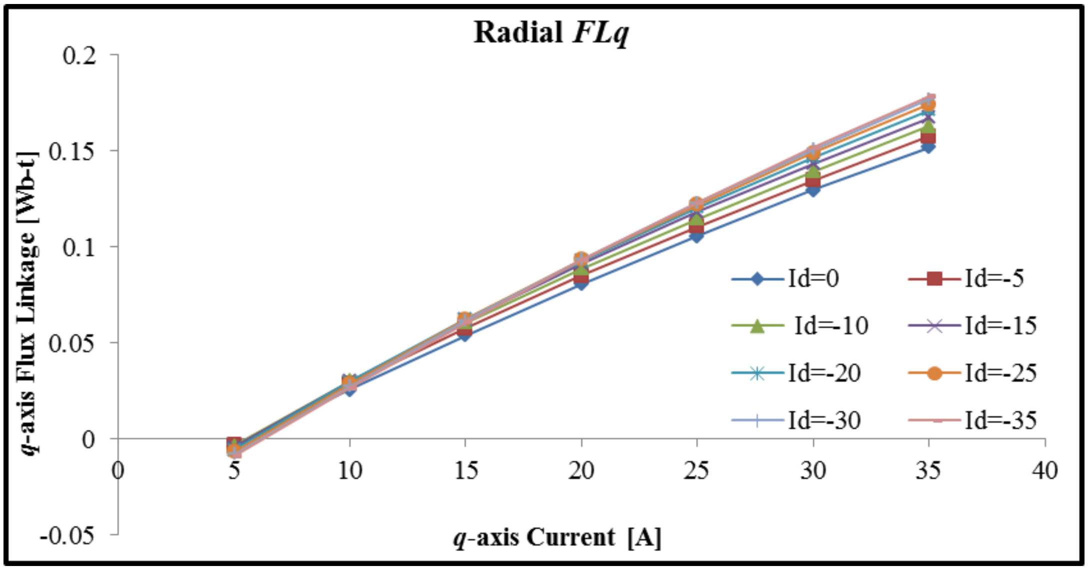

Figure 4.24: Radial Variation of *q*-axis Flux Linkage with Applied *d* and *q*-axis Currents

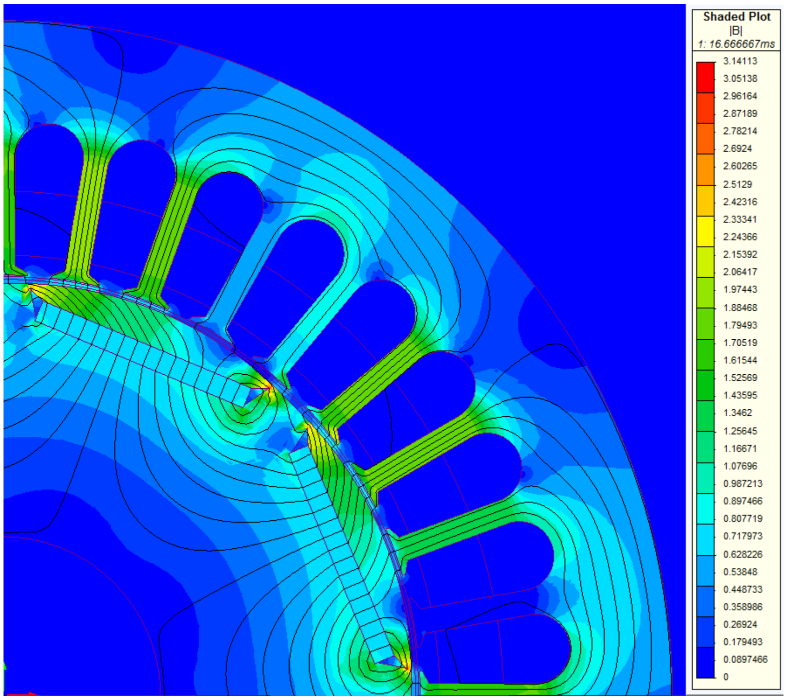

a) $I_d = 0$ and $I_q = 35$

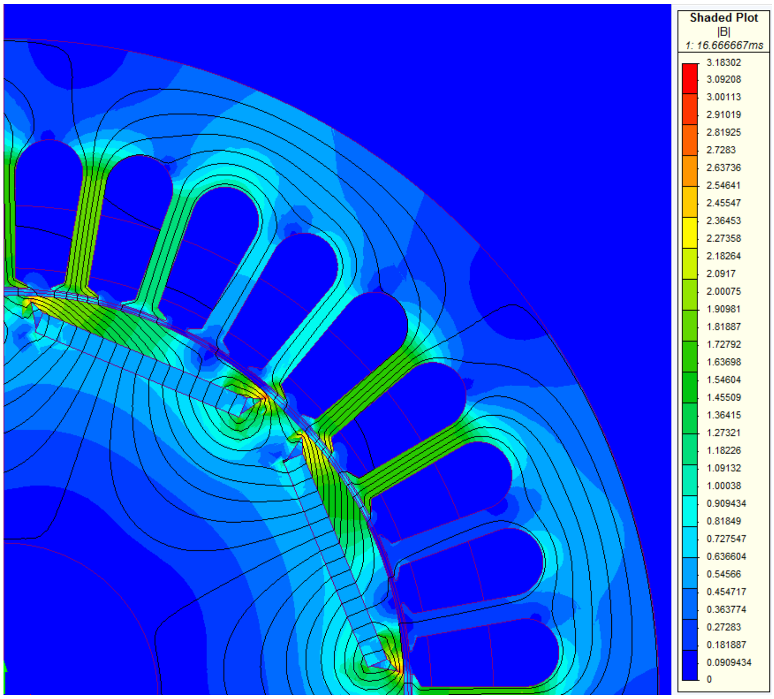

b) $I_d = -35$ and $I_q = 35$

Figure 4.25: Flat Rotor with Applied Current

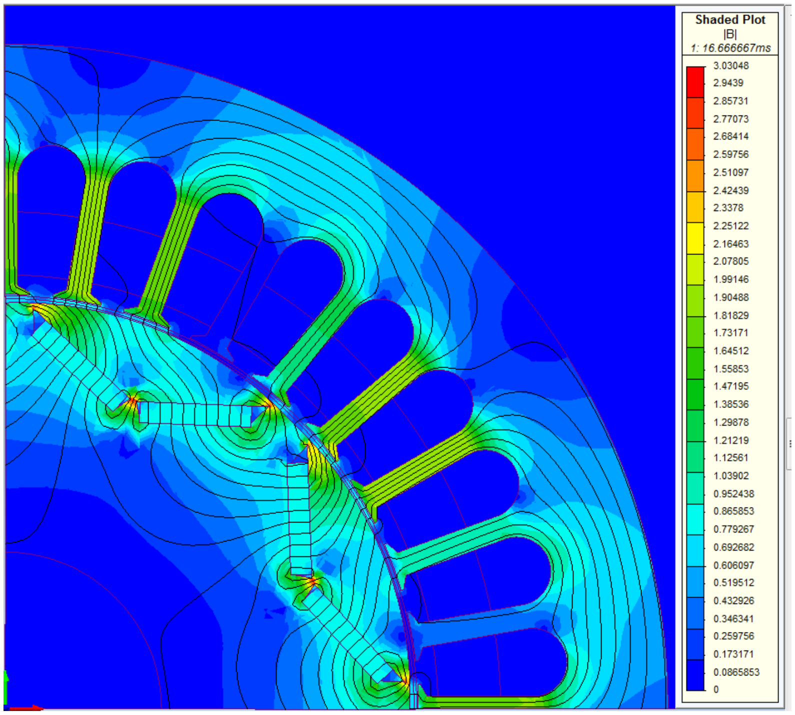

a) $I_d = 0$ and $I_q = 35$

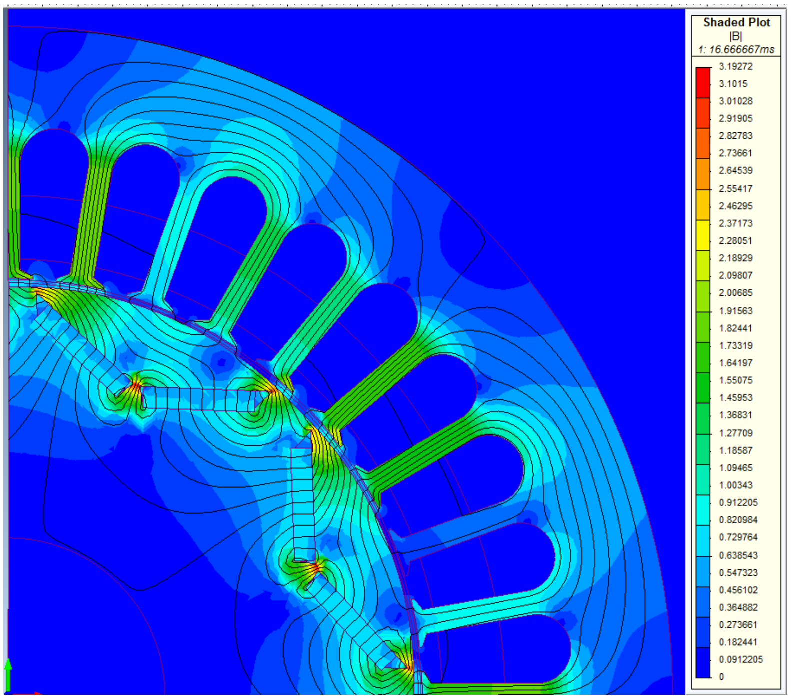

b) $I_d = -35$ and $I_q = 35$

Figure 4.26: V-shaped Rotor with Applied Current

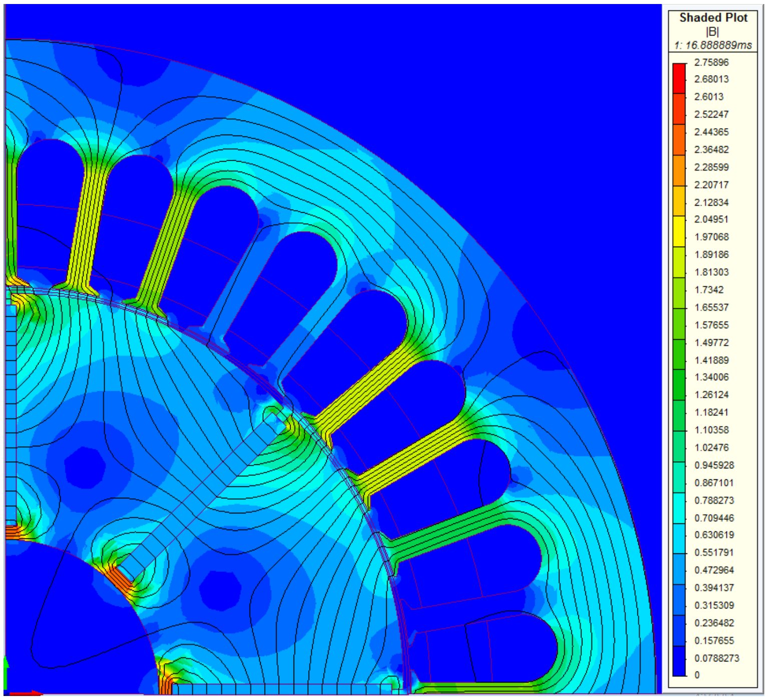

a) $I_d = 0$ and $I_q = 35$

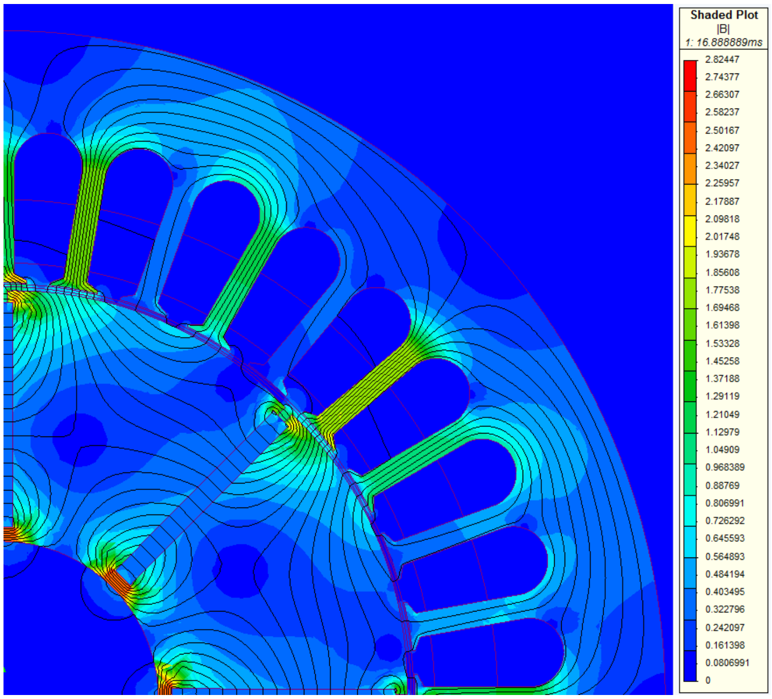

b) $I_d = -35$ and $I_q = 35$

Figure 4.27: Radial Rotor with Applied Current

These flux plots show all three rotor configurations at two different operating conditions, one for I_d=0 I_q=35 and the other for I_d=-35 I_q=35. In the operating condition I_d=0 I_q=35 shown in Figures 4.25a, 4.26a and 4.27a, it is observed that the resultant flux from the contributions of the permanent magnets and the *q*-axis current is saturating the motor. The direction of the resultant flux for the Flat and V-shaped rotor configurations lies in a direction that is between the *d* and *q*-axis of the rotor. However, in the radial rotor configuration there is a higher flux density due to the permanent magnet placement, thus making the resultant flux align more toward the *d*-axis. In the operating condition I_d=-35 I_q=35 shown in Figures 4.25b, 4.26b and 4.27b, it can be seen that the negative d-axis current lowers the permanent magnet flux causing the resultant flux to shift toward the *q*-axis of the rotor. This causes the saturation of the machine to reduce and increase the *q*-axis flux linkage. This increase of *q*-axis flux linkage will then increase the *q*-axis inductance which can be observed in Figures 4.28, 4.29 and 4.30 for the *q*-axis inductance for all three rotor configurations. Based on the above observations, it can be seen that the q-axis flux linkage and *q*-axis inductance are affected by saturation. Also, applying a negative *d*-axis current can decrease the effect of saturation on these parameters causing them to increase.

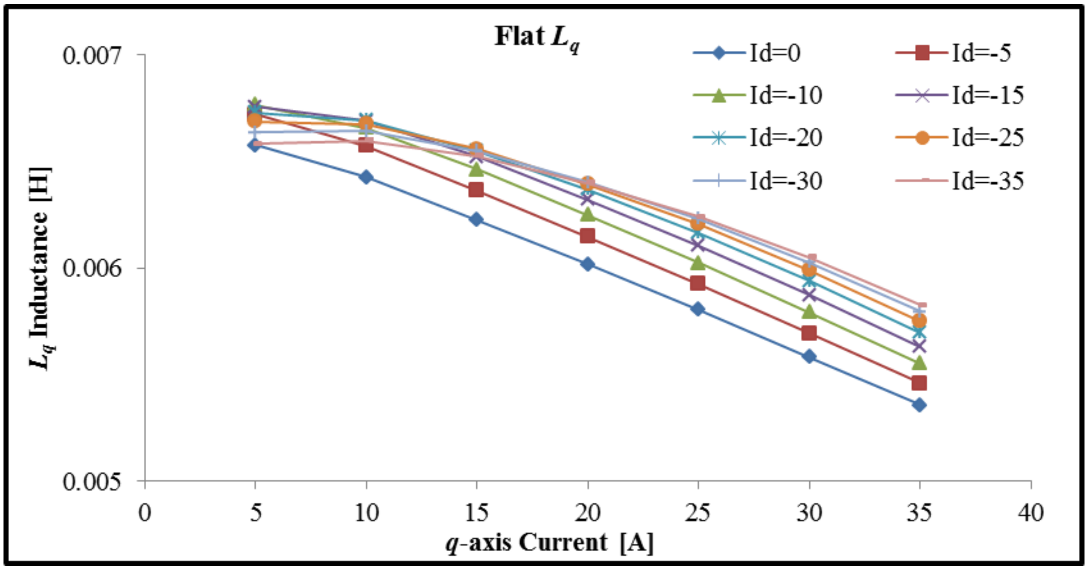

Figure 4.28: Flat *q*-axis Inductance Variation with Applied *d* and *q*-axis Currents

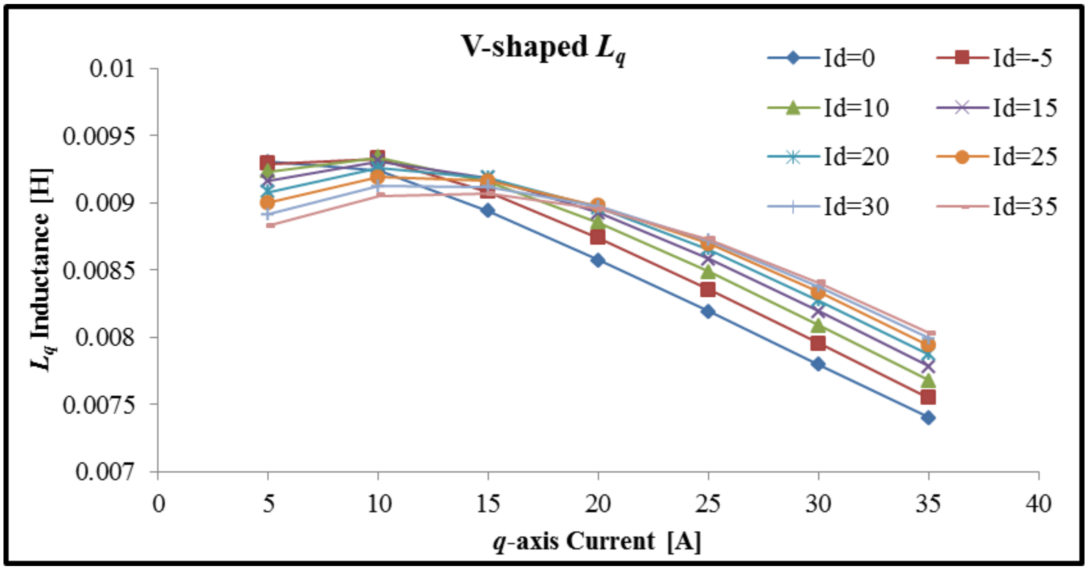

Figure 4.29: V-shaped q-axis Inductance Variation with Applied d and q-axis Currents

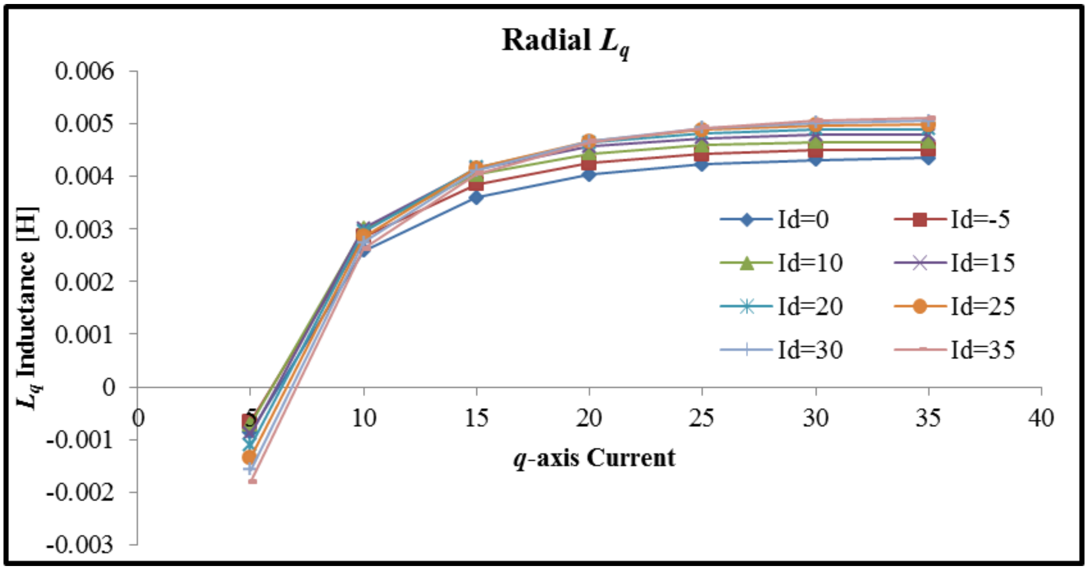

Figure 4.30: Radial q-axis Inductance Variation with Applied d and q-axis Currents

At lower values of q-axis current, there is an opposite effect on the q-axis inductance when the negative d-axis current is applied. At low values of I_q, the flux along the q-axis is mainly being supplied from the permanent magnets. Also, the machine is observed to be not highly saturated due to the low levels of q-axis current. This is evident in the flux function plots in Figures 4.31a, 4.32a and 4.33a for the operating condition of I_d=0 I_q=5. As the negative *d*-axis current is increased, the flux from the permanent magnets is reduced. Since the flux along the *q*-axis was supplied by the permanent magnets, the flux linkage of the *q*-axis is therefore reduced, due to the very low values of *q*-axis current. This reduction in *q*-axis flux linkage can be observed in the flux plots in Figures 4.31b, 4.32b and 4.33b for the operating condition of I_d=-35 I_q= 5. As the *q*-axis flux linkage is decreased when negative *d*-axis current is applied, the *q*-axis inductance will also be reduced. This can be observed in the *q*-axis inductance graphs as shown Figures 4.28, 4.29 and 4.30.

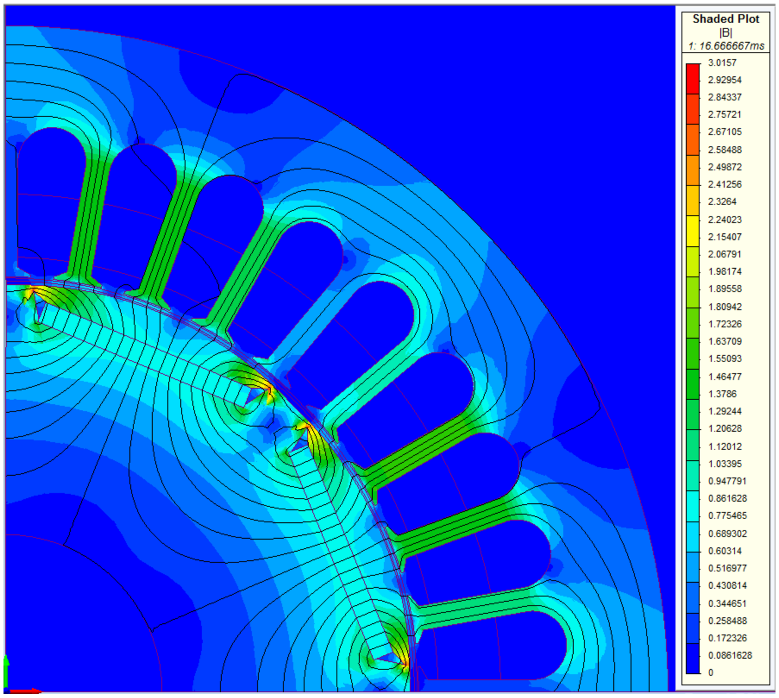

a) I_d = 0 and I_q = 5

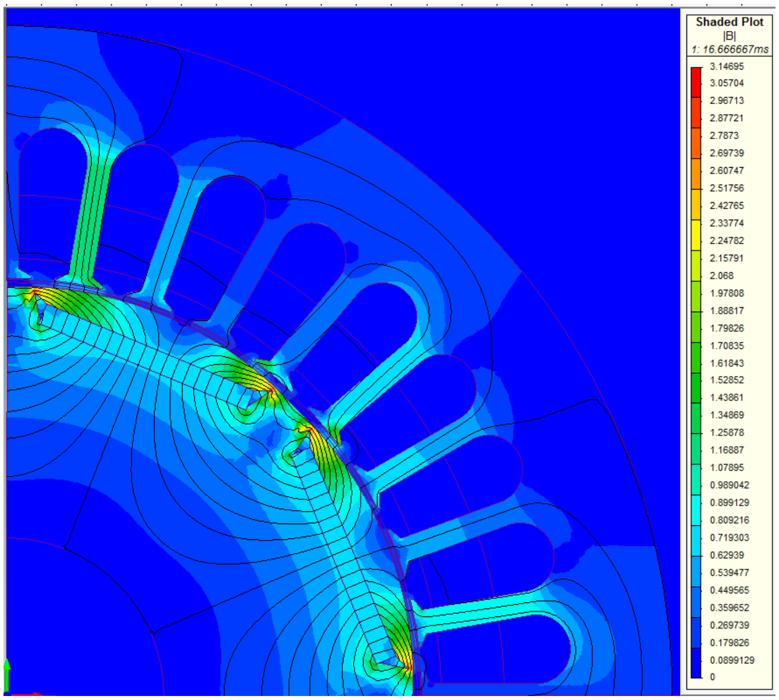

b) I_d = -35 and I_q = 5

Figure 4.31: Flat Rotor with Applied Current

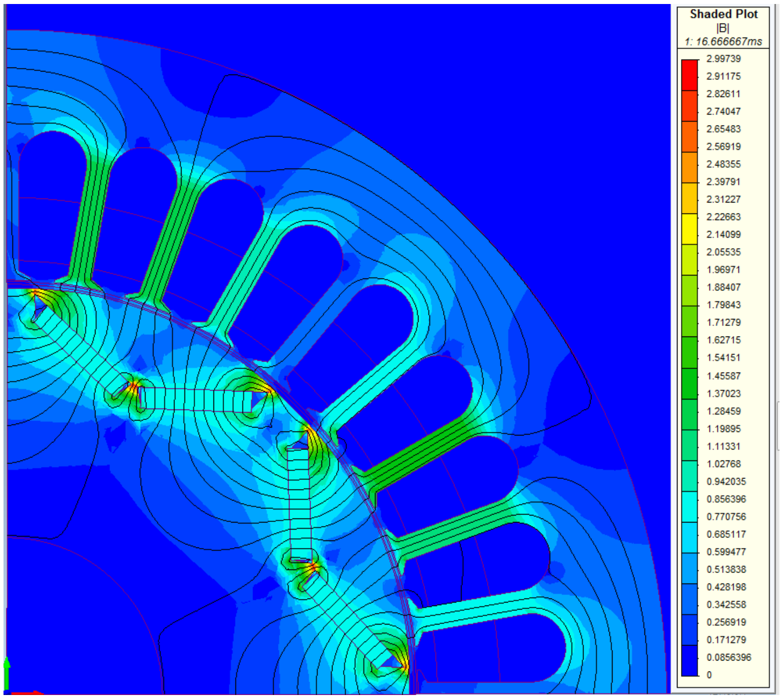

a) I_d = 0 and I_q = 5

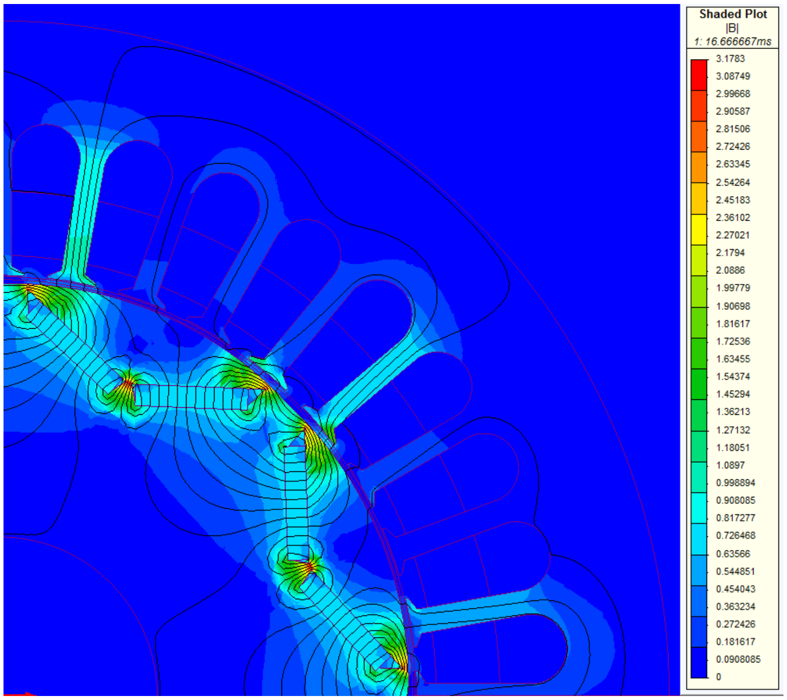

b) I_d = -35 and I_q = 5

Figure 4.32: V-shaped Rotor with Applied Current

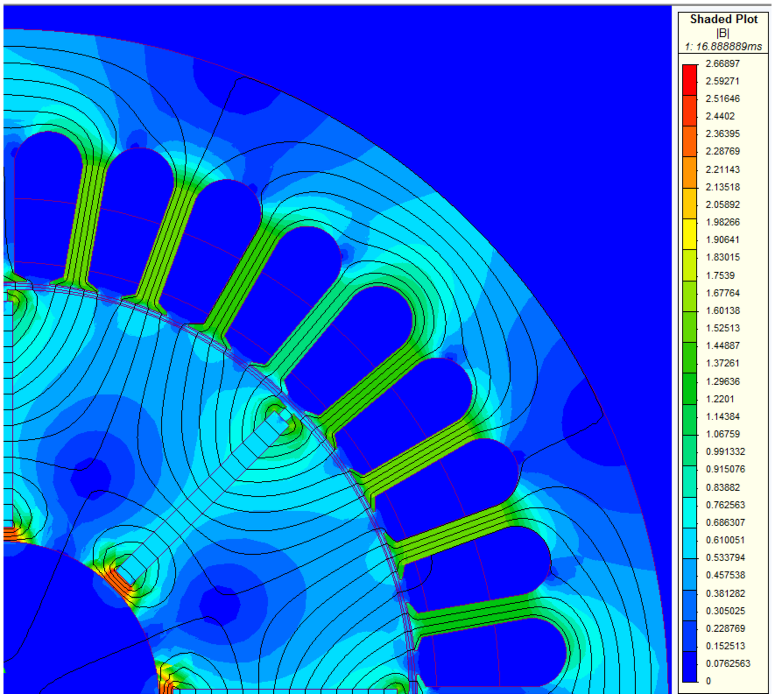

a) I_d = 0 and I_q = 5

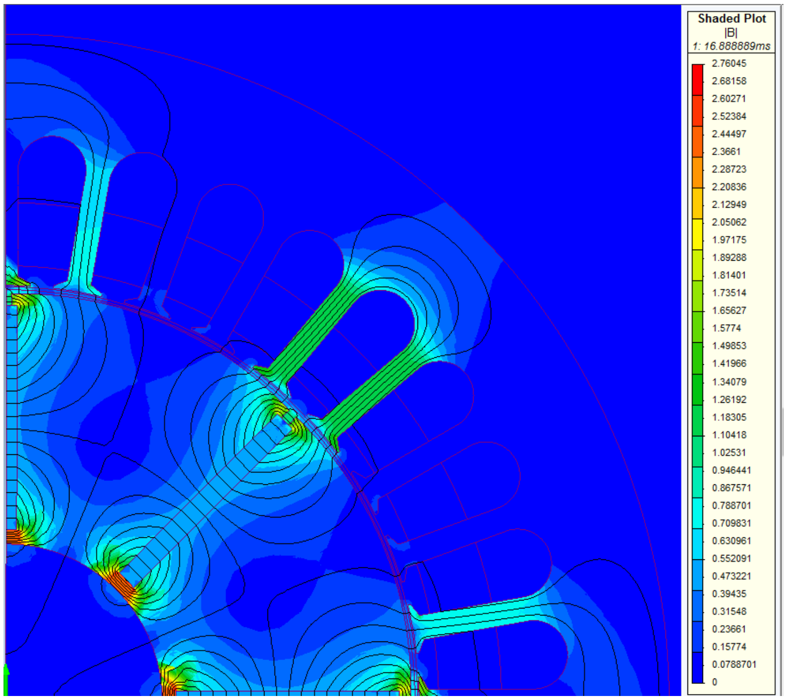

b) $I_d = -35$ and $I_q = 5$

Figure 4.33: Radial Rotor with Applied Current

4.5.4 *d*-axis Parameter Variation

Figures 4.34, 4.35 and 4.36 show the *d*-axis flux linkage determined by the parameter variation simulations for all three rotor configurations. Looking at the *d*-axis flux linkage, one can see that all three rotor configurations follow the same trend. That is, the *d*-axis flux linkage varies with *q*-axis current at low values of *d*-axis current, but is observed to not be affected by the *q*-axis current at higher levels of negative *d*-axis current.

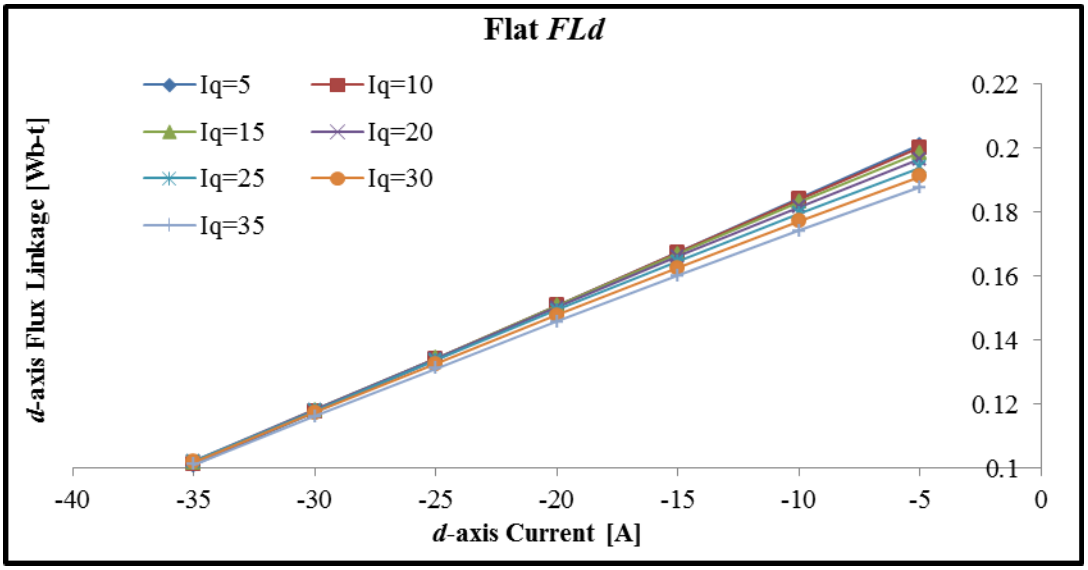

Figure 4.34: Flat *d*-axis Flux Linkage Variation with Applied *d* and *q*-axis Currents

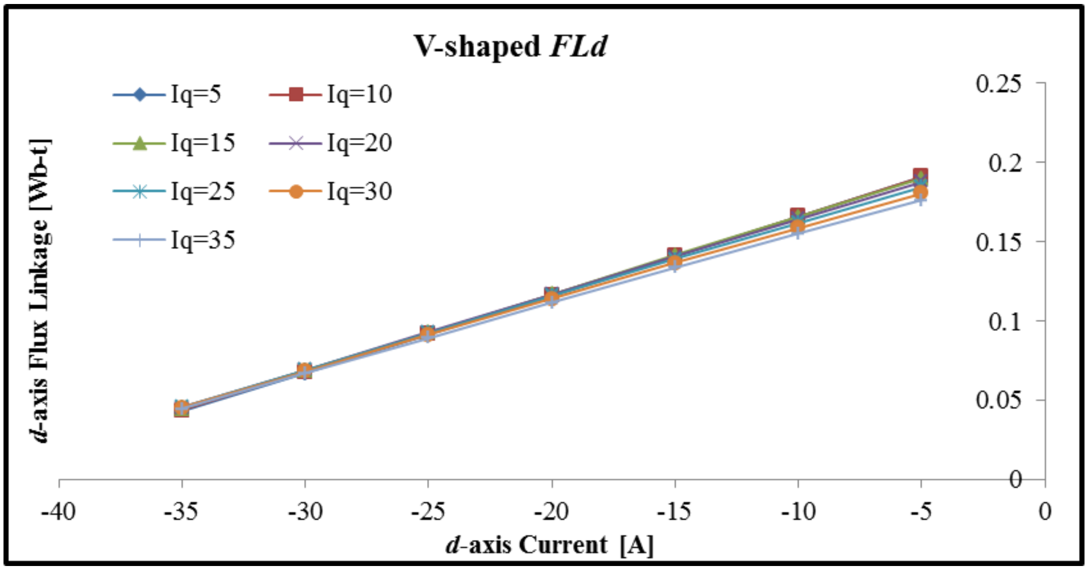

Figure 4.35: V-shaped *d*-axis Flux Linkage Variation with Applied *d* and *q*-axis Currents

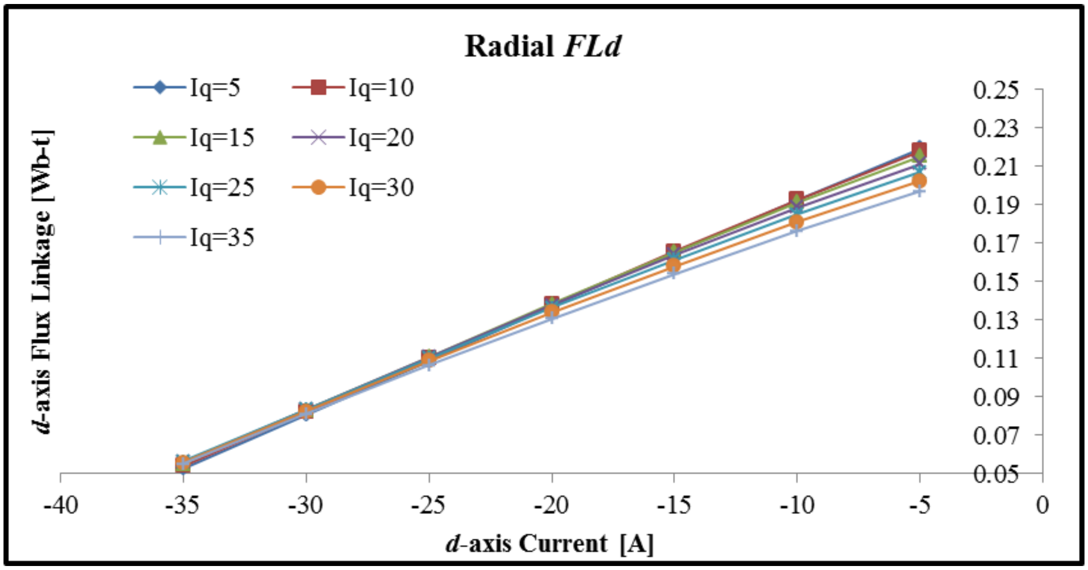

Figure 4.36: Radial *d*-axis Flux Linkage Variation with Applied *d* and *q*-axis Currents

Looking at Figures 4.40, 4.41 and 4.42 will clarify the reason behind this trend. Figures 4.40a, 4.41a and 4.42a, where the motors are operating at I_d=-5 I_q=5, show that the resultant flux is mainly in the *d*-axis, even though the *d*-axis is acting against the permanent magnet flux. Figures 4.40b, 4.41b and 4.42b, where the motors are operating at I_d=-5 I_q=35, show increased saturation in the machine due to the increase of *q*-axis current. This increase in saturation due to the *q*-axis current and the permanent magnets will result in a lowering of the *d*-axis flux linkage. This lowering of the *d*-axis flux linkage is observed in Figures 4.34, 4.35 and 4.36. This effect in *d*-axis flux linkage due to the *q*-axis current for low values of negative *d*-axis current is also observed in the *d*-axis inductances as shown in Figures 4.37, 4.38 and 4.39.

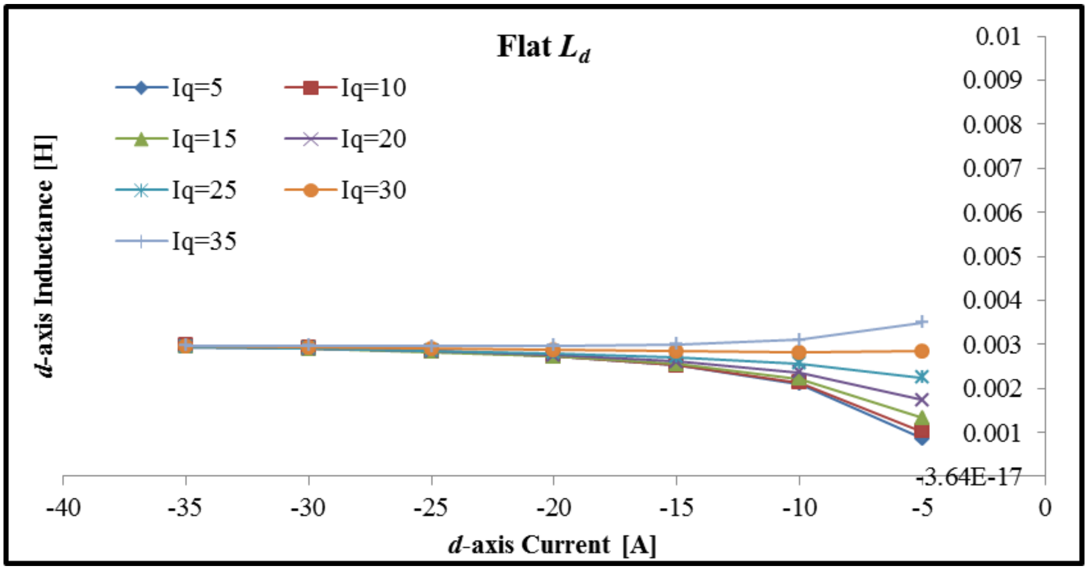

Figure 4.37: Flat *d*-axis Inductance Variation with Applied *d* and *q*-axis Currents

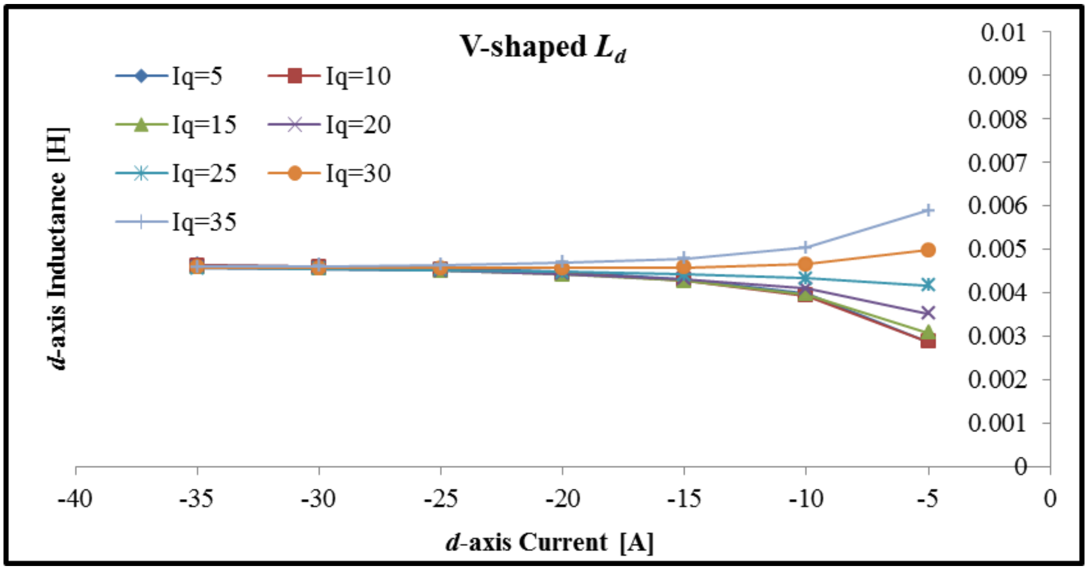

Figure 4.38: V-shaped *d*-axis Inductance Variation with Applied *d* and *q*-axis Currents

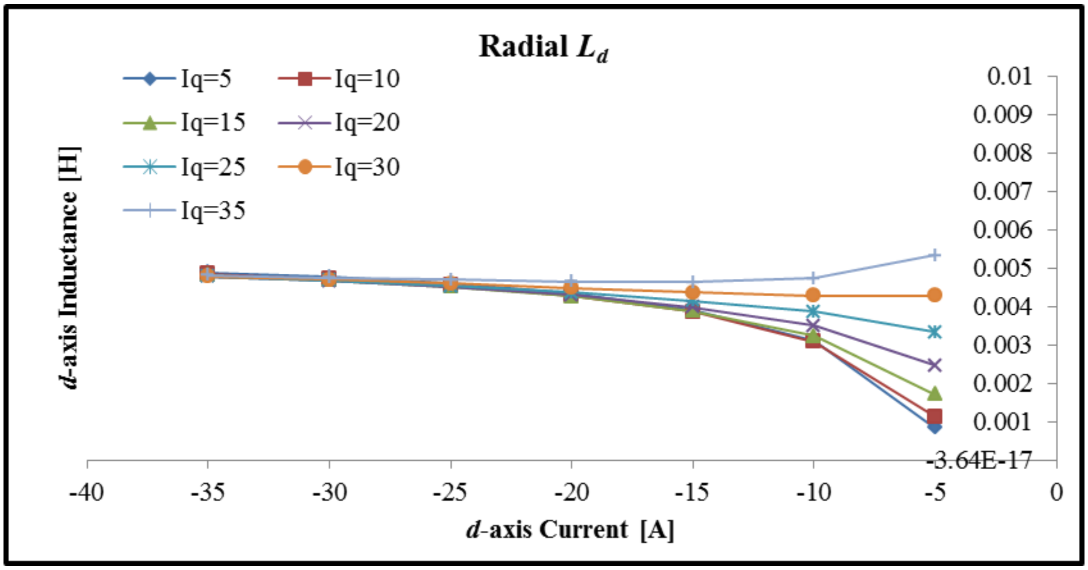

Figure 4.39: Radial *d*-axis Inductance Variation with Applied *d* and *q*-axis Currents

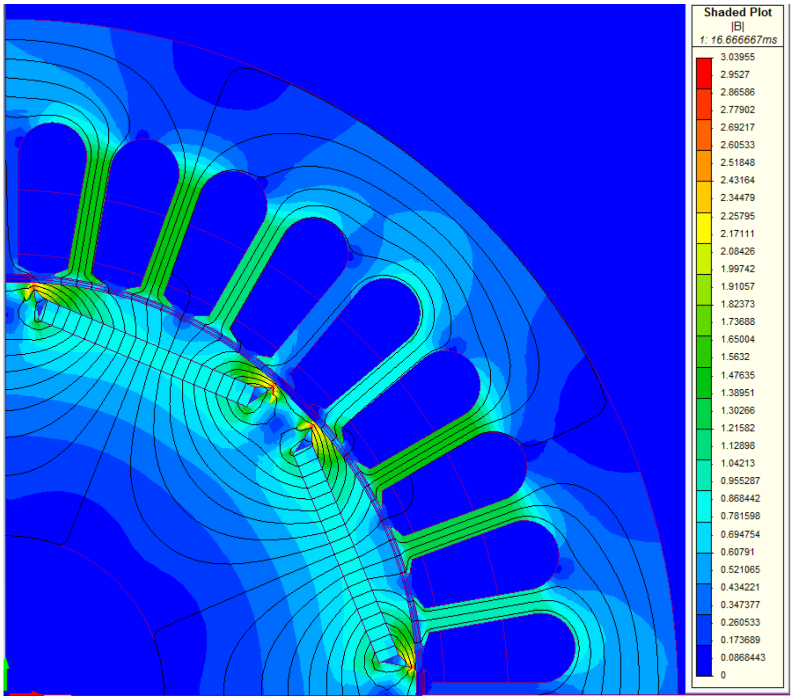

a) I_d = -5 and I_q = 5

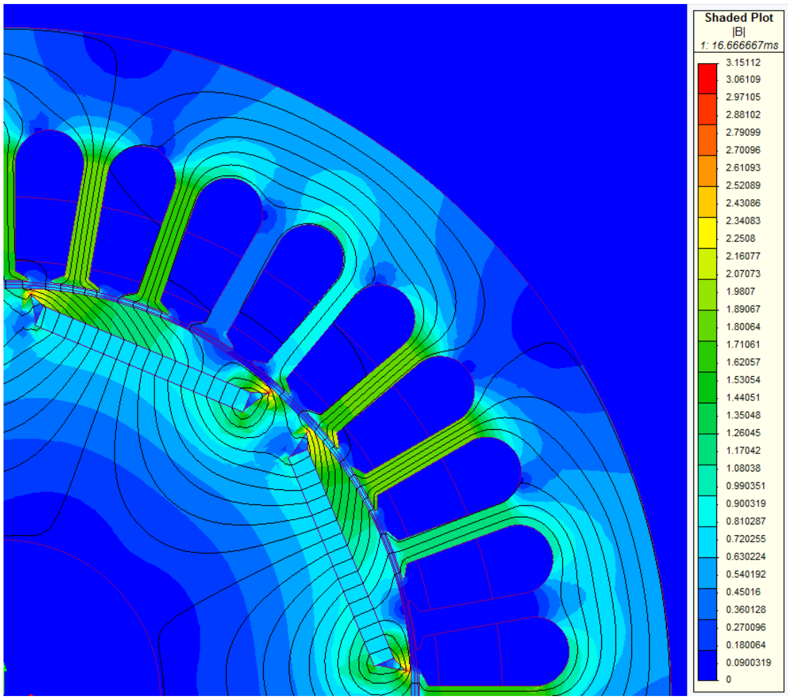

b) I_d = -5 and I_q = 35

Figure 4.40: Flat Rotor with Applied Current

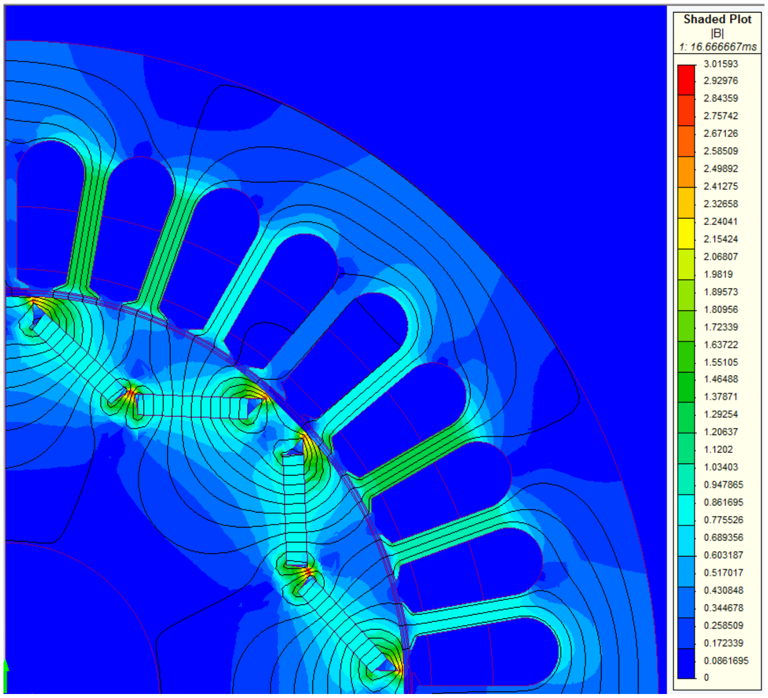

a) I_d = -5 and I_q = 5

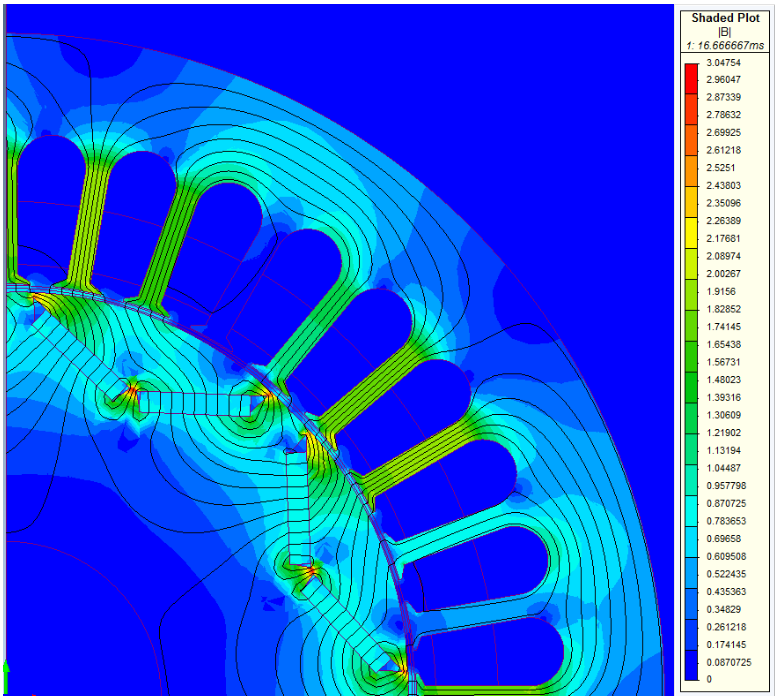

b) I_d = -5 and I_q = 35

Figure 4.41: V-shaped Rotor with Applied Current

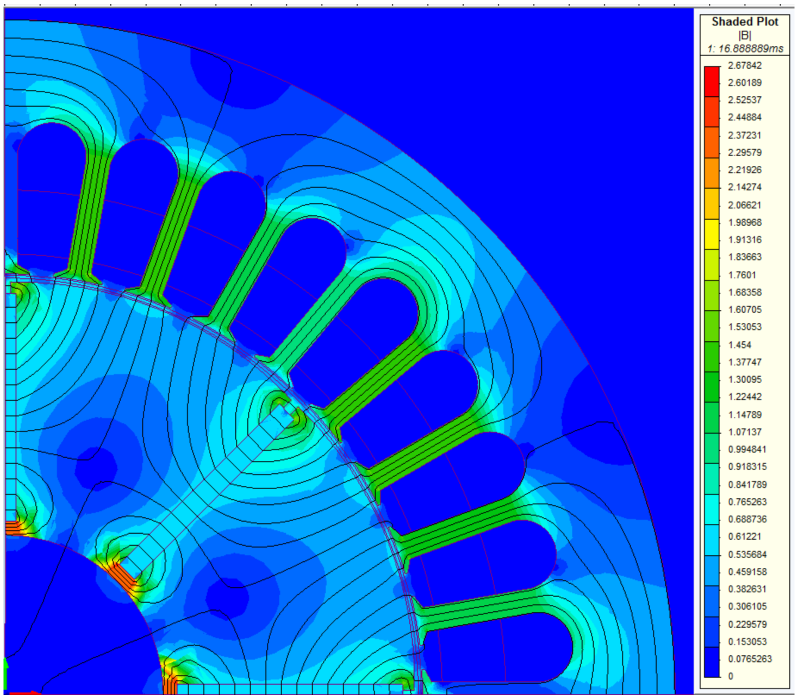

a) I_d = -5 and I_q = 5

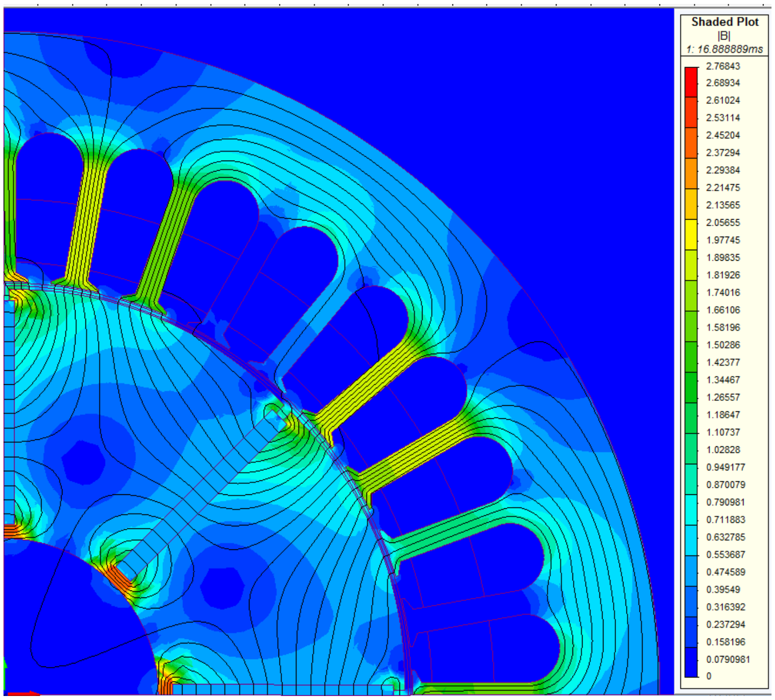

b) I_d = -5 and I_q = 35

Figure 4.42: Radial Rotor with Applied Current

However, as the negative *d*-axis current is increased the *d*-axis flux linkage decreases and is observed not to be affected by the *q*-axis current. This can be seen in the flux plots in Figures 4.25b 4.26b and 4.27b for I_d=-35 I_q=35 and Figures 4.43, 4.44 and 4.45 for I_d=-35 I_q=5. In these figures, it is observed that the flux along the *d*-axis is at a low value for both the I_d =-35 I_q =5 or I_d =-35 I_q =35 flux plots. Therefore, the high demagnetizing flux produced by the high negative *d*-axis current will reduce saturation of the *d*-axis. With the *d*-axis unsaturated, the *d*-axis flux linkage will have a more linear characteristic causing the *d*-axis inductance to have a more consistent value.

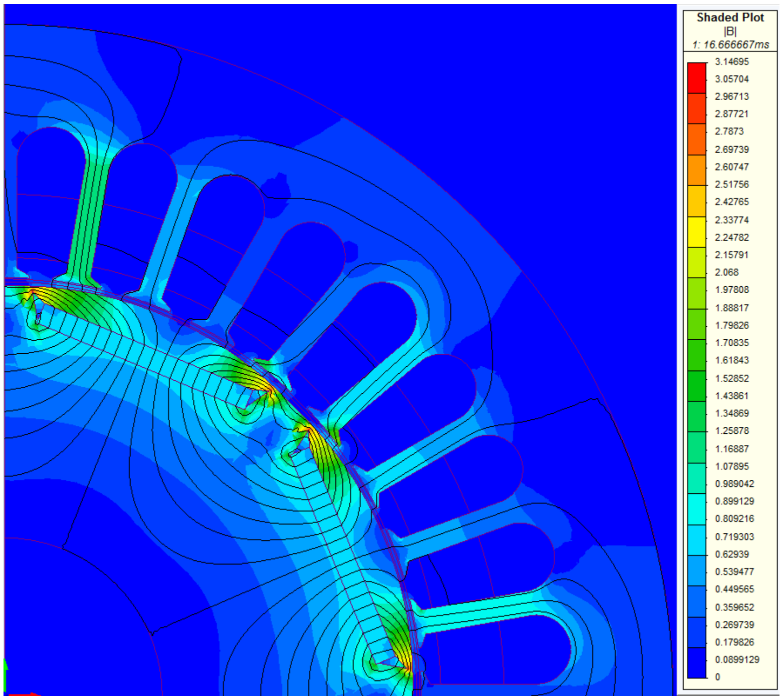

Figure 4.43: Flat with I_d = -35 and I_q = 5

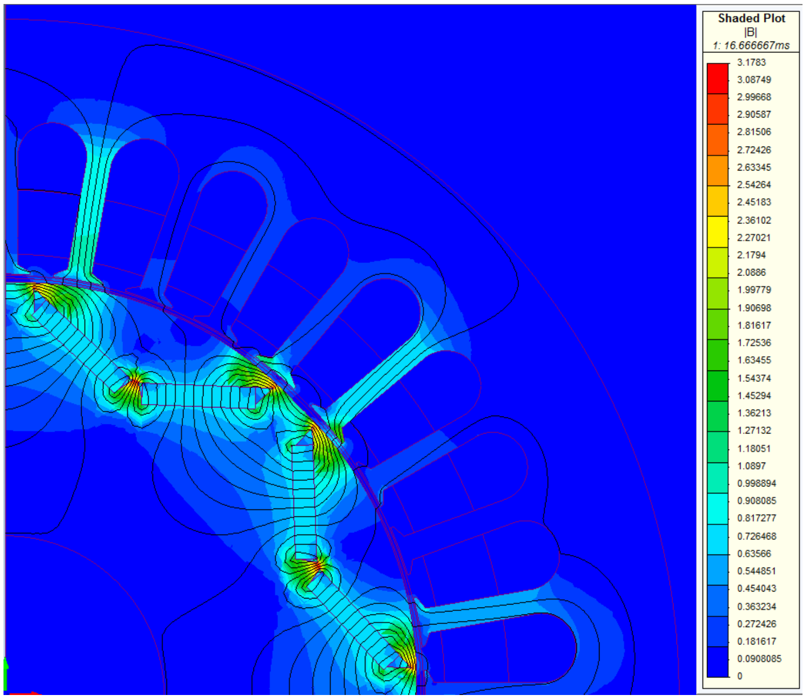

Figure 4.44: V-shaped with I_d = -35 and I_q =5

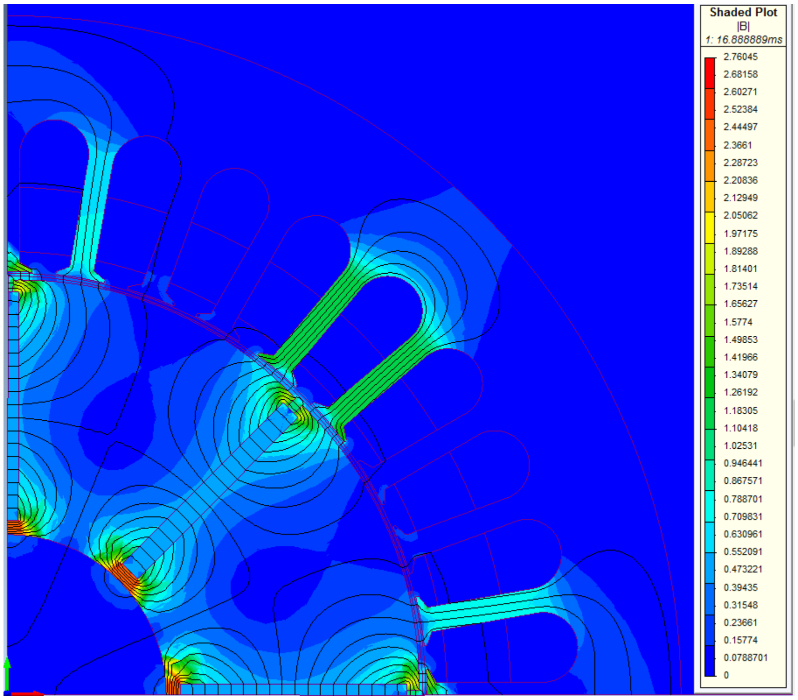

Figure 4.45: Radial with I_d = -35 and I_q = 5

4.5.5 Parameter Variation Effects on Performance

The effect on the performance of the rotor configurations due to the parameter variation will be discussed next. This will be done by analyzing the variation of L_d-L_q due to the applied *d* and *q*-axis currents and its effect on the reluctance torque production capabilities. Figures 4.46, 4.47 and 4.48 show the variation of L_d-L_q for various *d* and *q*-axis currents that are applied to the motor.

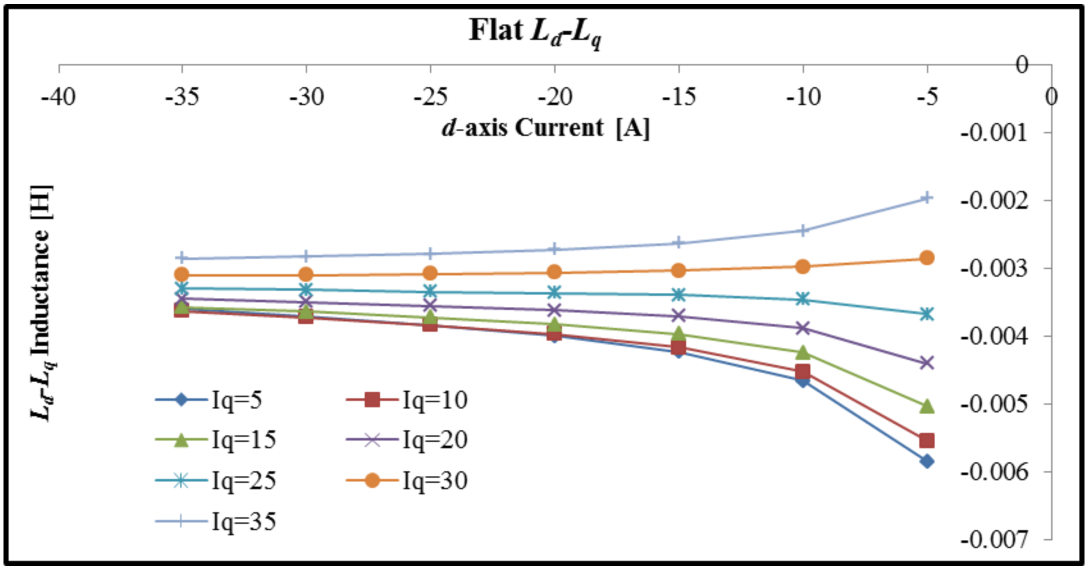

Figure 4.46: Flat Rotor L_d-L_q Variation with Applied *d* and *q*-axis Currents

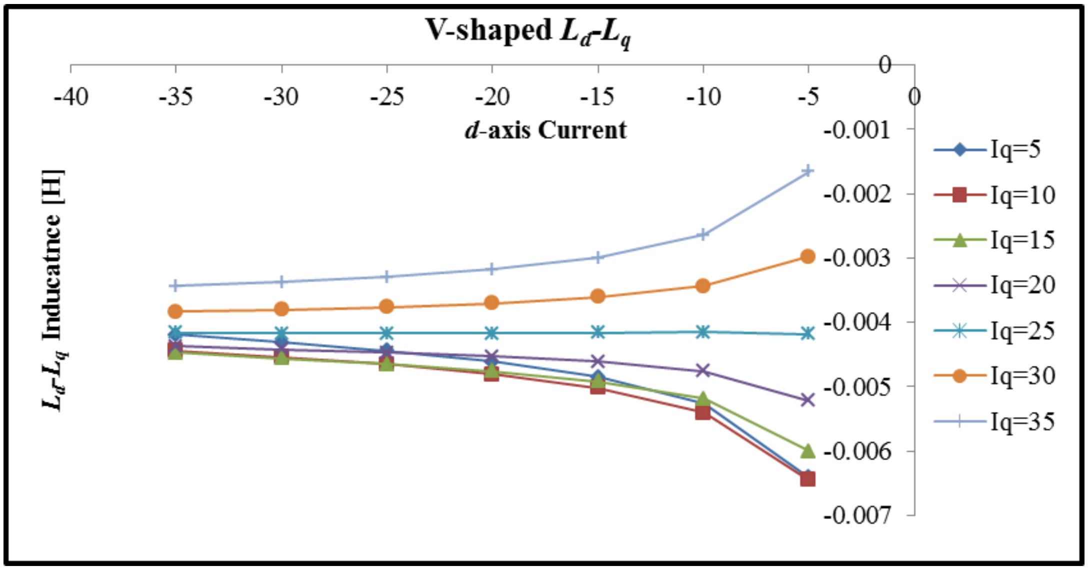

Figure 4.47: V-shaped Rotor L_d-L_q Variation with Applied *d* and *q*-axis Currents

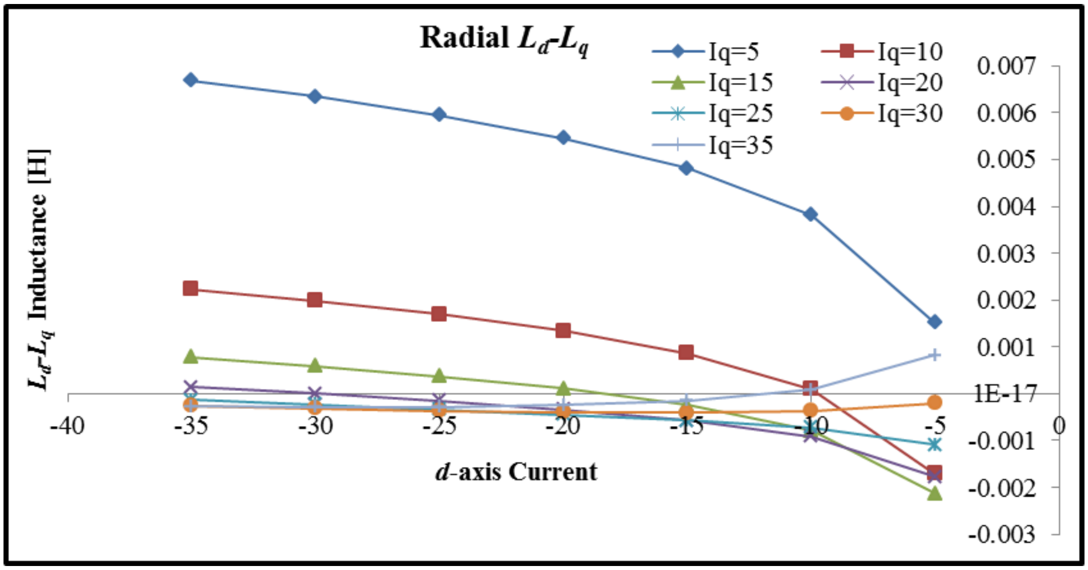

Figure 4.48: Radial Rotor L_d-L_q Variation with Applied *d* and *q*-axis Currents

Looking at the figures for the Flat and V-shaped rotor configurations, one can see that the higher the applied current to the machine, the smaller the negative L_d-L_q value. Therefore, as the *q*-axis current is increased, the reluctance torque capabilities of the machine reduce due to the parameter variations of the machine. Looking at the Radial rotor configuration, one can see that L_d-L_q quantity is positive at low *q*-axis current. This indicates that the reluctance torque acts against the synchronous torque of the machine. However, as the *d*-axis current is increased, the L_d-L_q quantity does reduce to a negative value which will then produce reluctance torque to add to the synchronous torque of the machine.

The effect of magnet placement on parameter variation is evident when comparing the Radial rotor configuration to the Flat and V-shaped rotor configurations. The Radial rotor configuration affected the flux paths due to the magnet placement on the *q*-axis. In addition, the Radial rotor configuration affected the resultant flux of the machine due to the higher flux produced by the placement of the permanent magnets. In the case of the Flat and V-shaped rotor configurations, the parameter variations caused the reduction of reluctance torque capabilities when a high *q*-axis current was applied. However, in the Radial rotor configuration, the parameter variation caused the rotor configuration to produce negative reluctance torque, unless there was a high *q*-axis current. At high *q*-axis current, the Radial rotor configuration’s parameter variation caused it to produce low positive reluctance torque.

Chapter 5

5.0 Conclusion and Future Work

This research study was conducted in an effort to understand what effects the rotor configuration has on the performance of a permanent magnet synchronous machine, independent of the stator configuration. Three motors were designed with different interior permanent magnet rotor configurations. The stator laminations were kept the same for all three motors so that the difference between the motors was only their rotor configurations. This design approach was taken in order to observe the effects on performance caused by the rotor configuration. A finite element analysis model coupled with a *dq*-axis circuit model was used to analyze the steady state performance of each rotor configuration. To prove confidence in the results from the model used in this study, a verification and validation process was done on the model. The validation of this model was done by comparing it to a motor design software program used in industry. The error between the model developed for this study and the motor design software was in the range of 4.6 to 10.8 %. For the purpose of this study, these error values are within acceptable limits to provide confidence in the model's results.

The purpose of this study was to understand what performance characteristics were affected by the rotor design. By understanding what performance aspects are affected by the rotor design, it may be possible to improve motor performance by making design changes to the rotor configuration. For the use in HEV and EV applications, the motor design not only has to perform to the desired performance requirements but it also has to be designed so that it can be manufactured in the automotive industry. Since the current manufacturing capabilities of the electric machine's stator are limited due to the complexity of the windings, it would be desirable to improve motor performance by making design changes on the rotor and not further complicate the stator design.

5.1 Summary of Study

The results of this compressive study are summarized in the following paragraphs for each rotor configuration's performances.

The Flat rotor configuration had the best torque production in the flux weakening region with its high torque values and a linear decline as speed increased. It produced a low torque ripple between the ranges of 9%-18%. It also had the best balance between its torque production and efficiencies. The effect of parameter variation on the Flat rotor configuration caused the reduction of reluctance torque capabilities when a high q-axis current was applied.

The V-shaped rotor configuration had a high torque production in the constant torque region of 70 Nm but fell below the Flat rotor configuration in the flux weakening region. It had the highest reluctance torque production capabilities by having the highest negative difference between L_d and L_q of -0.00314 H. It had the poorest efficiency of all three rotor configuration but it produced a low torque ripple between the ranges of 9%-18%. The effect of parameter variation on the V-shaped rotor configuration caused the reduction of reluctance torque capabilities when a high q-axis current was applied.

The Radial rotor configuration had the least favorable torque capabilities of all three rotor configurations. However, it did have a linear decline in torque as speed increased in the flux weakening region. It had the highest synchronous torque production capabilities of all three rotor configurations having the highest permanent magnet flux linkage of 0.2239 Wb-turns. The Radial rotor configuration had the highest efficiency region but had the lowest torque production capabilities compared to the other two rotor configurations. However, it had the highest torque ripple with a range of 12%-42%. The parameter variation of the Radial rotor configuration had the effect of producing negative reluctance torque, unless there was a high q-axis current applied. At high q-axis current, the Radial rotor configuration's parameter variation caused it to produce a low positive reluctance torque.

It was not the objective of this work to select the most suitable rotor configuration for the application of HEV and EV since the focus of this study was only on performance effects due to the rotor configuration. Also, it would be ill-advised to select a rotor configuration from this study since there was no attempt to optimize any of these motors.

5.2 Conclusion

The aim of this study was to understand what performance characteristics were affected by the rotor design. Based on the analysis of Chapter 4, which is summarized in the paragraphs above, it can be concluded that by keeping the stator configuration constant, the rotor design can affect the synchronous and reluctance torque production, efficiency, torque ripple and parameter variation of an interior PMSM.

5.3 Future Work

Future work could focus on the optimal stator design based on the manufacturing limitations and the motor performance requirements for the HEV and EV applications. Once an optimal stator design is determined, the observations of this study could be applied to develop a motor that has high performance due the rotor design and also meets the manufacturing requirements of the automotive industry.

REFERENCES/BIBLIOGRAPHY

[1] http://www.huffingtonpost.com/2012/08/28/new-mileage-standards-obama_n_1836546.html, “Fuel Efficiency Standards: Obama Administration Finalizes New Regulations For Cars And Trucks” Huffington post, August 2012.

[2] http://www.caranddriver.com/features/how-automakers-will-meet-2016-cafe-standards, “How Automakers Will Meet 2016 CAFE Standards”, Car and Driver, May 2010.

[3] M. A. Saidel, M. C. E. S. Ramos and S. S. Alves, “Assessment and Optimization of Induction Electric Motors Aiming Energy Efficiency in Industrial Applications,” in *Proc. International conference of Electric Machine ICEM*, 2010, Rome.

[4] OEK Onwunta and MTE Kahn, “Energy Efficiency and Reliability Improvement Strategies In Industrial Electric Motor-Driven Systems (Emds),” in *Proc. the 8th Conference on the Industrial and Commercial Use of Energy*, Aug 2011, Cape Town.

[5] Jacek F. Gieras, *Motor Technology Design and Applications*, Second Edition, Copyright 2002 by Marcel Dekker, Inc.

[6] T. Finken, M. Hombitzer and K. Hameyer, "Study and Comparison of Several Permanent-Magnet Excited Rotor Types Regarding Their Application in Electric Vehicles," in *Proc. Emobility-Electrical Power Train*, 2010.

[7] T. Finken and K. Hameyer, "Design of Optimization of an IPMSM with Fixed Outer Dimensions for Application in HEVs," in *Proc. IEEE International Electric and Drives Conference*, May 3-6, 2009.

[8] K. Yamazaki, Y. Fukushima and M. Sato, "Loss Analysis of Permanent-Magnet Motors with Concentrated Winding-Variation of Magnet Eddy-Current Loss Due to Stator and Rotor Shapes," *IEEE Transactions on Industry Applications*, Vol.45, No. 4, July/August 2009.

[9] K. Yamazaki, and A. Abe, "Loss Investigation of Interior Permanent-Magnet Motors Considering Carrier Harmonics and Magnet Eddy Currents," *IEEE Transactions on Industry Applications*, Vol. 45, No. 2, March/April 2009.

[10] K. Yamazaki and Y. Seto, " Iron Loss Analysis of Interior Permanent-Magnet Synchronous Motors-Variation of Main Loss Factors Due to Driving Condition," *IEEE Transaction on Industry Application*, Vol. 42, No. 4, July/August 2006.

[11] K. Yamazaki, Y. Kanou, Y. Fukushima, S. Ohki, A. Nezu, T. Ikemi and R. Mizokami, "Reduction of Magnet Eddy-Current Loss in Interior Permanent-Magnet Motors with Concentrated Windings," *IEEE Transactions on Industrial Applications*, Vol.46, No.6, November/December 2010.

[12] K. Yamazaki and H. Ishigami, "Rotor-Shape Optimization of Interior-Permanent-Magnet Motors to Reduce Harmonic Iron Losses," *IEEE Transactions on Industrial Electronics*, Vol.7, No. 1, January 2010.

[13] K. Yamazaki, M. Shina, Y. Kanou, M. Miwa and J. Hagiwara, "Effect of Eddy Current Loss Reduction by Segmentation of Magnets in Synchrous Motors: Difference Between Interior and Surface Types," *IEEE Transactions on Magnetics*, Vol. 45, No.10, October 2009.

[14] S. Han, T. M. Jahns and Z. Q. Zhu, "Analysis of Rotor Core Eddy-Current Losses in Interior Permanent-Magnet Synchronous Machines," *IEEE Transactions on Industry Application*, Vol. 46, No. 1, January/February 2010.

[15] Su-Jim Lee, Sung-ll Kim and Jung-Pyo Hong, "Investigation on Core Loss According to Stator Shape in Interior Permanent Magnet Synchronous Motor", in *Proc. The 11th International Conference on Electrical Machines and Systems*, October 17-20, 2008 Wuhan, China.

[16] G. R. Slemon, A Straughen, *Electric Machines*, Addison-Wesley Publishing Company Copyright 1980.

[17] Stephen J. Chapman, *Electric Machinery Fundamentals*, 4th Edition, McGraw –Hill Copyright 2005.

[18] chi ,"Position-Sensorless Control Of Permanent Magnet Synchronous Machines Over Wide Speed Range", Ph D Dissertation, The Ohio State University, United Stated, 2007.

[19] Jacek F. Gieras, Permanent Magnet Motor Technology: Design and Applications, 3rd Ed., CRC Press, 2009.

[20] Paul C. Kruse, *Analysis of Electric Machinery and drive Systems*, IEEE Press Copyright 2002.

[21] Thomas M. Jahns, Gerald B. Kliman and Thomas W. Neumann, "Interior Permanent-Magnet Synchronous Motors for Adjustable-Speed Drives," *IEEE Transactions on Industry Applications*, Volume: IA-22, Issue:4, 1986.

[22] Jurgen Reinert, Ansgar Brockmeyer and Rik W. A. A. De Donker, "Calculation of Losses in Ferro- and Ferromagnetic Materials Based on the Modified Steinmetz Equation" *IEEE Transaction on Industrial Applications*, Vol. 37, No. 4, July/August 2001.

[23] Bertotti, "Hysteresis in Magnetism: For Physicists, Materials Scientist, and Engineers", Academic Press, 1998.

[24] C. Mi, G. R. Slemon, R. Bonert, " Modeling of Iron Losses of Surface-Mounted Permanent Magnet Synchronous Motors," in *Proc. IEEE Industry Applications Conference*, 2001.

[25] M. Ibrahim and P. Pillay, "Core loss prediction in electrical machine laminations considering skin effect and minor hysteresis loops," in *Proc.Energy Conversion Congress and Exposition (ECCE)*, 2012.

[26] J.D. Lavers, P.P. Biringer and H. Hollitscher, "A simple method of estimating the minor loop hysteresis loss in thin laminations," *IEEE Transactions on Magnetics*, Volume: 14 , Pages 386 – 388, 1978.

[27] K. Atallah, Z. Q. Zhu and D. Howe, “An Improved Methd for Predicting Iron Losses in Brushless Permanent Magnet DC Drives” *IEEE Transaction on Magnetics,* Volume: 28, Issue: 5, 1992.

[28] Roshen, "Iron Loss Model for Permanent-Magnet Synchronous Motors," *IEEE Transactions on Magnetics*, Volume: 43 , Issue: 8, Pages: 3428 – 3434, 2007.

[29] A.A. Jimoh, S, R.D. Findlay, SM, and M. Poloujadoff, "Stray Losses in Induction Machines: Part I, Definition, Origin and Measurement", *IEEE Transactions on Power Apparatus and Systems*, Vol. PAS-104, No. 6, June 1985.

[30] Rich Schifierl, “Design considerations for salient pole, permanent magnet synchronous motors in variable speed drive applications,” Ph D Dissertation, University of Wisconsin-Madison, United States, 1987.

[31] http://www.infolytica.com/secured/customer/elite/livedocs/, "Sloving", Infolytica.

[32] Gyu-Hong Kang, Jung-Pyo Hong,, Gyu-Tak Kim, and Jung-Woo Park, “Improved Parameter Modeling of Interior Permanent Magnet Synchronous Motor Based on Finite Element Analysis,” *IEEE Transactions on Magnetics,* Volume: 36 , Issue: 4 , Part: 1, Pages: 1867 – 1870, 2000.

[33] M.S. Islam, S. Mir, T. Sebastian and S. Underwood, “Design Considerations of Sinusoidally Excited Permanent Magnet Machines for Low Torque Ripple Applications,” *IEEE Transactions on Industry Applications,* Volume: 41 , Issue: 4 Page(s): 955 – 962, 2005.

[34] A. Kioumarsi, M. Moallem and B. Fahimi, “Mitigation of Torque Ripple in Interior Permanent Magnet Motors by Optimal Shape Design,” *IEEE Transactions on Magnetics,* Volume: 42, NO. 11, 2006.

[35] J. A. G¨uemes, A. M. Iraolagoitia, J. I. Del Hoyo, and P. Fern´andez, “Torque Analysis in Permanent-Magnet Synchronous Motors: A Comparative Study, *IEEE Transactions on Energy Conversion*, Volume. 26, Issue: 1, 2011.

[36] M. Chaieb, S. Tounsi, R. Neji and F. Sellami, “Optimum Geometry for Torque Ripple Minimization of Permanent Magnet Motor by the Finite Element Method,” in *Proc. of the 14th IEEE Mediterranean Electrotechnical Conference*, Pages: 459 – 464, 2008.

[37] Chang-Sung Jin, Dae-Sung Jung, Ki-Chan Kim, Yon-Do Chun, Hyung-Woo Lee, and Ju Lee, “A Study on Improvement Magnetic Torque Characteristics of IPMSM for Direct Drive Washing Machine,” *IEEE Transactions on Magnetics*, Volume: 45, Issue: 6, 2009.

[38] Hang-Sheng Chen, David G. Dorrell, and Mi-Ching Tsai, “Design and Operation of Interior Permanent-Magnet Motors with Two Axial Segments and High Rotor Saliency,” *IEEE Transactions on Magnetics*, Volume: 46, Issue: 9, Pages: 3664 – 3675, 2010.

[39] Mohammad S. Islam, Rakib Islam and Tomy Sebastian, “Experimental Verification of design techniques or permanent Magnet Synchronous Motors for Low-Torque-Ripple Applications,” in *Proc. of the IEEE Energy Conversion Congress and Exposition*, ECCE 2009, Pages: 214 – 219, 2009.

[40] R. Krishnan, Permanent Magnet Synchronous and Brushless DC Motor Drives, pg. 250-254, CRC Press , Taylor Financial Group, 2010.

[41] Pragasan Pillay, and R. Krishnan, " Modeling of Permanent Magnet Motor Drives", *IEEE Transactions on Industrial Electronics*, Vol. 35, No. 4, November 1988.

[42] Naomitsu Urasaki, Tomonobu Senjyu, and Katsumi Uezato, "A Novel Calculation Method for Iron Loss Resistance Suitable in Modeling Permanent-Magnet Synchronous Motors," *IEEE Transactions on Energy conversion*, Vol. 18, No. 1, March 2003.

[43] Naomitsu Urasaki, Tomonobu Senjyu, and Katsumi Uezato, "Relationship of Parallel Model and Series Model for Permanent Magnet Synchronous Motors Taking Iron Loss Into Account" *IEEE Transactions on Energy Conversion*, Vol. 19, No. 2, June 2004.

[44] Valentin Navrapescu, Mircea Popescu, Dragos Ovidiu Kisck and Mariana Kisck, "Modelling of Iron Losses in Salient Pole Permanent Magnet Synchronous Motors", in *Proc. of the The 7th International Conference on Power Electronics*, October 22-26, 2007, EXCO, Daegu Korea.

[45] Y. S. Chen, Z. Q. Zhu and D. Howe, "Calculation of d- and q-Axis Inductances of PM Brushless ac Machines Accounting for Skew," *IEEE Transactions on Magnetics*, Volume. 41, Isseu: 10, Pages: 3940 – 3942, 2005.

[46] Hui Guo1 and Meiyang Zuo "2D and 3D Magnetic Field Finite Element Analysis and Contrast of Permanent Magnet Synchronous Generator", 2011 International Conference on Electric Machines and Systems, August 2011.

[47] http://oee.nrcan.gc.ca/industrial/equipment/motors/10718, Energy Efficiency Reference Guide Electric Motors, Natural Resource Canada.

[48] J. R. Hendershot and T.J.E. Miller, *Design of Brushless Permanent-Magnet Machines*, Oxford: Clarendon Press, copyright 1994.

[49] Duane C. Hanselman, *Brushless permanent-magnet motor design*, McGraw-Hill Copyright 1994.

[50] http://www.infolytica.com/secured/customer/elite/livedocs/, "Materials", Infolytica .

[51] Michael Liwschitz-Garik and Clyde Colburn Whipple. *"Alternating-current machines",* Princeton, N.J., Nostrand., 1961.

[52] A.K. Sawhney, *A cource in Electrical Machine Design*, Dhanpat Ri & Co. (P) Ltd.

[53] Moskowitz, Lester R., *Permanent magnet design and application handbook,* Boston : Cahners Books International, copyright 1976.

[54] William L. Oberkampfa and Timothy G. Trucanob "Verification and validation in computational fluid dynamics," *Progress in Aerospace Sciences 38*, Pages: 209–272, 2002.

[55] "An Overview of the PTC 60 / V&V 10 Guide for Verification and Validation in Computational Solid Mechanics" The American Society of Mechanical Engineers. All rights reserved.

[56] G. Almandoz, J. Poza, M.A Rodriguez and A. Gonzalez, "Modeling of Cross-Magnetization Effect in Interior Permanent Magnet Machines," in *Proc. of the 18th International Conference on Electrical Machines,* Pages 1-6, 2008.

[57] U. Schaible and B. Szabado,"Dynamic Motor Parameter Identification for High Speed Flux Weakening Operation of Brushless Permanent Magnet Synchronous Machines," *IEEE Transactions on Energy Conversion,* Volume: 14, Issue: 3, 1999.

[58] A. Gebregergis M. Islam , T. Sebastian and R. Ramakrishnan, "Evaluation of Inductance in a Permanent Magnet Synchronous Motor," in *Proc. of the IEEE International Electric Machines & Drives Conference,* Page(s): 1171 – 1176, 2011.

[59] Gyu-Hong Kang, Byoung-Kuk Lee and Hyuk Nam, "Analysis of Single-Phase Line-Start Permanent-Magnet Motor Considering Iron Loss and Parameter Variation With Load Angle," *IEEE Transactions on Industry Applications,* Volume: 40, Issue: 3, 2004.

[60] Ming-De Chen, Enrico Levi and Mark Dov Pelka, "Iron Saturation Effects in PM AC Motors," *IEEE Transactions on Magnetics,* Volume: 21, Issue: 3, 1985.

[61] Jiliang Li, Lin Gao, Huifang Sun, Huabo Huang and Guodong Liu, "Experimental Analysis and Simulation of Saturation Effects in Interior Permanent-Magnet Synchronous Motor," *in Proc. of the International Conference on Electrical Machines and Systems*, Pages: 1–6, 2011.

[62] LIN Weijie, "Study on Direct Torque Control of Permanent Magnet Synchronous Motor Based on Observing Stator Flux Linkage," in *Proc. of the International Technology and Innovation Conference,* Pages: 1957-1962, 2006.

[63] A. Soualmi, F. Dubas, D. Dépernet, A. Randria and C. Espanet, " Inductances Estimation in the d-q Axis for an Interior Permanent-Magnet Synchronous Machines with Distributed Windings," in *Proc. of the XXth International Conference on Electrical Machines*, Pages: 30 –314, 2012.

[64] Christos Mademlis and Vassilios G. Agelidis, On Considering Magnetic Saturation with Maximum Torque to Current Control in Interior Permanent Magnet Synchronous Motor Drives," *IEEE Transactions on Energy Conversion,* Volume: 16, Issue. 3, 2001.

[65] Sang-Yong Jung, "Numerical Identification of D and Q Axis Parameters for Multi-Layer Buried PM Synchronous Motor considering Cross-Magnetization," in *Proc. of the International Conference on Electrical Machines and Systems*, Pages: 729 – 734, 2007.

[66] Aimeng Wang, Heming Li and Cheng-Tsung Liu, "Assessments of Magnetic Cross-Coupling Impacts on Interior Permanent Magnet Machine Controls for Electric Vehicles," in *Proc. of the International Conference on Power Electronics and Drive Systems*, Pages: 1435 – 1438, 2009.

[67] Bojan ˇStumberger, Gorazd ˇStumberger and Drago Dolinar, “Evaluation of Saturation and Cross-Magnetization Effects in Interior Permanent-Magnet Synchronous Motor,” *IEEE Transactions on Industry Applications*, Volume: 39, Issue: 5, 2003.

[68] Hu Jianhui, Zou Jibin and Liang Weiyan, “Finite Element Calculation of the Saturation DQ-Axes Inductance for a Direct-Drive PM Synchronous Motor Considering Cross-Magnetization,” in *Proc. of the Fifth International Conference on Power Electronics and Drive Systems*, Volume: 1, 2003.

[69] G. Qi, J. T. Chen , Z. Q. Zhu, D. Howe, L. B. Zhou and C. L. Gu, “Influence of Skew and Cross-coupling on d- and q-Axis Inductances and Flux-Weakening Performance of PM Brushless AC Machines,” *IEEE Transactions on Magnetics*, Volume: 45, Issue: 5, Pages: 2110 - 2117, 2009.

VITA AUCTORIS

NAME:	James Edward Kettlewell
PLACE OF BIRTH:	Windsor, ON
YEAR OF BIRTH:	1984
EDUCATION:	Holy Names High School, Windsor, ON, 2002 St. Clair College of Applied Arts & Technology, Electronics Engineering Technician, Windsor, ON, 2004 University of Windsor, B.A.Sc., Windsor, ON, 2009